Quantum gases in optical lattices

Fabrice Gerbier

March 16, 2018

Contents

1. Introduction

The purpose of these notes is to discuss the physics of quantum gases of ultracold atoms trapped in optical lattices. Optical lattices are periodic structures of light created by the interference between laser beams, that can trap atoms (or other electrically polarizable particles) near the nodes or the antinodes of the interference pattern. They were first explored in the 1990s [1], following the dramatic progress in cooling neutral atomic gases in the years 1980s. These early experiments were performed with gases that are very dilute by today's standards (one atom per hundred or thousand lattice sites), yet cold enough to observe characteristic phenomena of quantum particles in periodic potentials, such as Bragg diffraction or Bloch oscillations. With the advent of Bose-Einstein condensates (BECs) and degenerate Fermi gases (DFGs), an entirely new regime opened where filling factors of one atom or more per lattice site can be achieved. Combining quantum degenerate atomic gases and optical lattices allows experimentalists to study many quantum-mechanical phenomena usually associated with electrons in a crystal, but with unprecedented control over both the lattice and the particle properties and a time resolution not easily accessible in solid-state systems.

Moreover, the strong confinement at the trapping sites of the optical lattice gives access to strongly correlated phases of matter completely different from weakly-interacting gases, such as Mott insulators. To illustrate the latter point, let us focus on the case of bosonic atoms. From a many-body point of view, a weakly-interacting gas of bosons is expected to form a BEC, which corresponds to a N-particle state

$$|\Psi\rangle_N \approx \frac{1}{\sqrt{N!}} \left(\hat{a}_\phi^\dagger\right)^N |\varnothing\rangle \tag{1.1}$$

in second-quantized notation. In the last expression, $|\varnothing\rangle$ is the vacuum state and $\hat{a}_\phi^\dagger$ creates a particle in the state ϕ. Such a state describes well a weakly-interacting gas, a statement usually justified by an argument of *adiabatic continuity*. One can imagine the actual interacting system as emerging from an ideal gas after a slow ramp of the strength of the interactions. A system prepared in the ground state should follow that ramp adiabatically, and therefore remain to a good approximation in a product state but with a modified ϕ affected by interactions. This reasoning is at the basis of the Gross-Pitaevskii theory of BECs[1]. For fermions, a similar argument is used to justify that a Fermi liquid should arise from a non-interacting Fermi gas.

For sufficiently strong interactions between the particles, this adiabatic picture breaks down, and other phases of matter may emerge. Such phases are described by a many-body wave function that differs substantially from the product state in Eq. (1.1), possessing in particular short-range correlations on the scale of the average inter-particle distance $\rho^{-1/3}$, with ρ the mean particle density. For a gas of atoms with mass m_a, such short-range correlations entail a kinetic energy cost $\sim \hbar^2\rho^{2/3}/2m_a$ from dimensional arguments. Comparing this kinetic energy to the typical interaction energy $4\pi\hbar^2 a\rho/m_a$, with a the $s-$wave scattering length, one finds

$$\frac{E_{\rm kin}}{E_{\rm int}} \sim \frac{1}{(\rho a^3)^{1/3}}. \tag{1.2}$$

This allows one to identify the so-called *diluteness parameter* ρa^3. For quantum gases in standard traps, and away from Feshbach resonances one has $\rho a^3 \ll 1$, which corresponds to a dilute gas that can be described by weakly-interacting theories. Conversely, strongly correlated system arises when the short-range behavior of the wave function becomes strongly distorted by interactions, or equivalently when $E_{\rm kin}/E_{\rm int} \sim 1$ (this is for instance the case in liquid ^{4}He).

This strongly interacting limit is unfortunately very hard to reach for bosons, even for very high densities, or close to a Feshbach resonance where a diverges. The reason lies in the occurrence of three-body recombination events. When three atoms collide, it is possible to form a molecule. The molecule and the remaining free atom carry away the binding energy as kinetic energy. Since the kinetic energy of the collisional partners (comparable to the binding energy, typically a few K) is very large compared to the trap depth ($\sim \mu$K for degenerate gases), they escape from the trap and are lost. The loss rate $\gamma_{\rm loss}$ for such three-body recombination events scale as $L_3\rho^2$, where the rate constant $L_3 \propto a^4$ for recombination into weakly bound states [3][2]. This leads to the estimate

$$\frac{\hbar\gamma_{\rm loss}}{E_{\rm int}} \sim \rho a^3. \tag{1.3}$$

[1] The Bogoliubov theory already predicts a wavefunction that deviates from the product state, see [2].

[2] For Rubidium atoms, for instance, $L_3 \sim 10^{-29}$ at/cm^6. At a typical density for a BEC, $\rho \sim 10^{14}$ at/cm^3 [$a \approx 5.5\,$nm, $\rho^{1/3}a \sim 3\times10^{-4}$], the lifetime is $\gamma_{\rm loss}^{-1} \sim 10\,$s.

We thus conclude that in the regime $\rho a^3 \sim 1$, the lifetime of a gas at very low temperatures will be very short due to three-body recombination. Ongoing research is trying to determine whether studying such a strongly interacting Bose liquid is possible at all [4, 5], but it is clear that this is a difficult path at the very least. For fermions, the Pauli principle saves the day and makes the gas stable under three-body recombination [6].

Instead of enhancing the interaction energy, another route to achieve $E_{\rm kin}/E_{\rm int} \sim 1$ is to reduce the kinetic energy. This is precisely what is done in optical lattices thanks to the band structure of the periodic potential. For deep lattices, atoms are tightly bound at the bottom of each well of the periodic potential, and the energy levels cluster into very narrow energy bands. The energy width of the lowest energy band J is proportional to the probability to tunnel from one well to a neighboring one, and plays the role of the kinetic energy. For deep lattices, J decays exponentially with the lattice depth, and thus can be strongly suppressed. At the same time, the interaction energy U is (mildly) enhanced by the increased confinement near each lattice site. It follows, 1) that the ratio

$$\frac{E_{\rm kin}}{E_{\rm int}} \sim \frac{J}{U} \tag{1.4}$$

can become $\ll 1$, and 2) that this ratio is tunable by a change of the depth of the lattice potential. The regime of strong correlations is thus within reach, even if the gas is very dilute.

We will explore some aspects of this physics in these notes. We discuss in the first Chapter the properties of quantum gases in lattices that do not depend on interactions, *i.e.* are mainly due to the underlying band structure. We discuss in details in a second Chapter the properties of interacting bosonic gases, with emphasis on the superfluid-Mott insulator transition that has been studied in details experimentally. Finally, we briefly review the case of interacting fermions in the last Chapter.

2. Optical lattices

2.1. Optical lattice potentials

2.1.1. Quick review of atom-light interactions

We consider an atom placed in a monochromatic light field $\boldsymbol{E}$ (such as the one created by a laser), written as

$$\boldsymbol{E} = \frac{\boldsymbol{\mathcal{E}}(\boldsymbol{r})}{2} e^{-i\omega_L t + i\varphi(\boldsymbol{r})} + \text{c.c.}, \tag{2.1}$$

with $\boldsymbol{\mathcal{E}}$ real. The electric field oscillates with frequency ω_L (wavelength λ_L, wave vector $k_L = 2\pi/\lambda_L$), and induces a non-zero electric dipole,

$$\boldsymbol{D} = \tilde{\alpha}(\omega_L)\boldsymbol{E} = \frac{\tilde{\alpha}(\omega_L)\boldsymbol{\mathcal{E}}(\boldsymbol{r})}{2} e^{-i\omega_L t + i\varphi(\boldsymbol{r})} + \text{c.c.} \tag{2.2}$$

Here $\tilde{\alpha}(\omega_L) = \alpha(\omega_L) + i\alpha'(\omega_L)$ is the complex electic polarisability of the atom.

The potential energy of the dipole, usually called *dipole potential*, is given by

$$V_{\text{dip}} = -\frac{1}{2}\overline{\boldsymbol{D}\cdot\boldsymbol{E}} = -\frac{1}{4}\alpha(\omega_L)|\boldsymbol{\mathcal{E}}|^2, \tag{2.3}$$

where the bar indicates time-averaging over an optical period and where the "extra" factor $\frac{1}{2}$ is needed for an induced dipole [7]. The dipole potential is determined by the real part of the polarisability (the component oscillating in phase with the electric field). The energy radiated by the dipole is given by $\overline{\dot{\boldsymbol{D}}\cdot\boldsymbol{E}} = -(\omega_L/2)\alpha'(\omega_L)|\boldsymbol{\mathcal{E}}|^2 = -\hbar\omega_L\Gamma_{\text{sp}}$ and is related to the imaginary part of the polarisability (the component oscillating in quadrature with the electric field). The second expression reintroduces "by hand" the concept of photons, by relating the radiated energy to the number of (spontaneously) emitted photons per unit time, Γ_{sp}.

We need to evaluate the average dipole (or equivalently, the polarisability) to be able to calculate the final form of the dipole potential. The simplest model ("two-level atom") considers a single optical transition between two particular atomic levels, the ground state g and an excited state e, with a Bohr frequency ω_{eg} relatively close to the laser frequency (to be able to single out one particular transition in the full optical spectrum of the atom). Using the stationary solution of the optical Bloch equations [8], one finds $\tilde{\alpha}(\omega_L) = (d^2/\hbar)/(-\delta_L + i\Gamma/2) \approx -(d^2/\hbar)(1/\delta_L + i\Gamma/2\delta_L^2)$. Here $\delta_L = \omega_L - \omega_{eg}$ is the detuning of the laser from the atomic resonance, Γ is the natural linewidth (inverse spontaneous emission time) of the transition, and $\Omega_L = d|\boldsymbol{\mathcal{E}}|/\hbar$ is the Rabi frequency with d the electric dipole matrix element characterizing the atom-light coupling strength for the transition under consideration.

A far-off resonance trap corresponds to the situation where $|\delta_L| \gg \Gamma, \Omega_L$. In this limit, the dipole potential reduces to

$$V_{\text{dip}} = \frac{d^2}{4\hbar\delta_L}|\boldsymbol{\mathcal{E}}|^2 = \frac{\hbar\Omega_L^2}{4\delta_L}, \tag{2.4}$$

and the spontaneous emission rate is given by

$$\Gamma_{\text{sp}} = \frac{\hbar\Gamma\Omega_L^2}{8\delta_L^2} = \frac{\Gamma}{2|\delta_L|}|V_{\text{dip}}|. \tag{2.5}$$

The two expressions show the different scaling with detuning of the dipole potential $V_{\text{dip}} \propto 1/\delta_L$ and of the spontaneous scattering rate $\Gamma_{\text{sp}} \propto 1/\delta_L^2$. In principle, the latter can be made as small as desired for a given V_{dip} by choosing sufficiently large detunings and by increasing $|\boldsymbol{\mathcal{E}}|$ (by increasing the light intensity).

Historically, optical lattices were first used to trap laser-cooled atoms, using light fairly close to resonance (see [1] for a review of early experiments with non-degenerate gases). The detuning of the light was optimized to cool and trap the atoms at the same time, but ultimately one faces the same temperature limits as in the continuum. In experiments with quantum gases, the dipole potential is viewed as *conservative*, as spontaneous emission is suppressed by using large detunings. One must however be aware that spontaneous emission still lurks around the corner: Each spontaneous

emission event releases a photon in a random direction, with the atom (center-of-mass) recoiling to conserve momentum. This leads to an increase of the mean atomic energy (heating) at a rate

$$\Gamma_{\text{heat}} = 2E_R\Gamma_{\text{sp}}. \tag{2.6}$$

Because the recoil energy $E_R = \hbar^2 k_{eg}^2/2m_a$ (m_a denotes the atomic mass) associated with the spontaneous photon of wavevector k_{eg} can be large compared to energy scales characterizing the center of mass motion (*e.g.* the chemical potential μ for a Bose-Einstein condensate, on the order of $50-100\,$nK in typical situations), the resulting heating rate Γ_{heat} can still be problematic even if Γ_{sp} is very low. In the rest of these lecture notes, we will assume this is not the case and consider only the effect of the dipole potential on the atomic motion.

Laser wavelength	Power	Beam waist	$\Omega_L/(2\pi)$	V_0/k_B	Γ_{sp}
850 nm	100 mW	100 μm	1 GHz	500 nK	0.01 s^{-1}

Table 2.1.: Typical numbers characterizing an off-resonant optical dipole trap for ^{87}Rb atoms.

2.1.2. 1D optical lattice: a standing wave

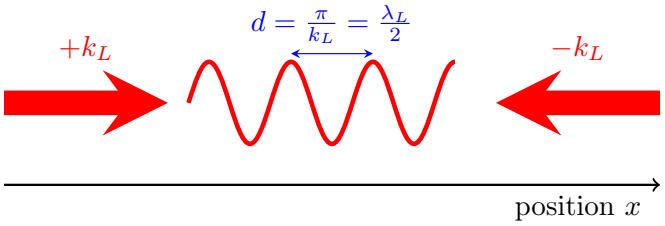

Figure 2.1.: Sketch of the laser arrangement to produce a 1D lattice. Two counter-propagating lasers at the same frequency produce a standing wave with spatial period $d = \lambda_L/2$, where λ_L is the wavelength of the lasers.

We are interested in the situation where several monochromatic plane waves with wave vectors $\mathbf{k}_n$, real amplitudes $\mathcal{E}_n$ and phases ϕ_n are involved. Then the total electric field $\boldsymbol{E} = \frac{1}{2}\sum_n \boldsymbol{\mathcal{E}}_n(\boldsymbol{r})e^{i\boldsymbol{k}_n\cdot\boldsymbol{r}-i\omega_L t+i\phi_n} + \text{c.c.}$ will generally display interferences between the various beams, with characteristic spatial frequencies $\mathbf{k}_n - \mathbf{k}_{n'}$ ($n \neq n'$).

The simplest example is that of two counter-propagating beams with $\mathbf{k}_1 = k_L\mathbf{e}_x, \mathbf{k}_2 = -\mathbf{k}_1$ (see Figure 2.1a). Choosing parallel polarizations and equal intensity to maximize the interference gives $|\mathcal{E}|^2 = \mathcal{E}_0^2\cos(k_L x + \phi_{21}/2)^2$, with $\mathcal{E}_1 = \mathcal{E}_2 = \mathcal{E}_0$ the amplitude of each beam and $\phi_{21} = \phi_2 - \phi_1$ the relative phase. Depending on the sign of the detuning δ_L, atoms will localize to the intensity maxima ($\delta_L < 0$ – attractive dipole potential) or minima ($\delta_L > 0$ – repulsive dipole potential). Choosing the former for concreteness, the dipole potential seen by the atoms is of the form

$$V_{1\text{D}} = -V_0\cos\left(2k_L x + \phi_{21}\right), \tag{2.7}$$

up to a constant term. Here $V_0 = d^2\mathcal{E}_0^2/|\delta_L|$ is the depth of the potential at the locations where the lasers interfere constructively[1]. The period of the potential, $d = \lambda_L/2$, can be increased by changing slightly the geometry (see Figure 2.1b) and sending the beams at an angle with the x axis. An important experimental problem is hidden in Eq. (2.7). From this equation, it is clear that the positions of the potential minima shift when the relative phase changes. In practice this phase will be random, due to uncontrolled changes in the optical path lengths of the two arms of the lattice (caused for instance by temperature fluctuations, vibrations, acoustic noise, ...). For a 1D lattice, this is not a terrible problem, since all sites shift together by the same quantity[2].

2.1.3. Square and cubic lattices

The problem becomes serious when trying to extend the scheme to higher dimensions (which requires more than two plane waves) to realize square (in two dimensions) or cubic (in three dimensions) lattices, as shown in Fig. 2.2. Then not only the position of the trapping sites, but also the topography of the potential can change wildly with the relative phases. Consider as an example a geometry with four beams with the same frequency, two counter-propagating along

[1] Note that V_0 is four times the potential depth created by one of the running wave alone

[2] If there is an additional potential superimposed to the lattice (see below), the random jittering of the minima can however lead to heating of the trapped atoms.

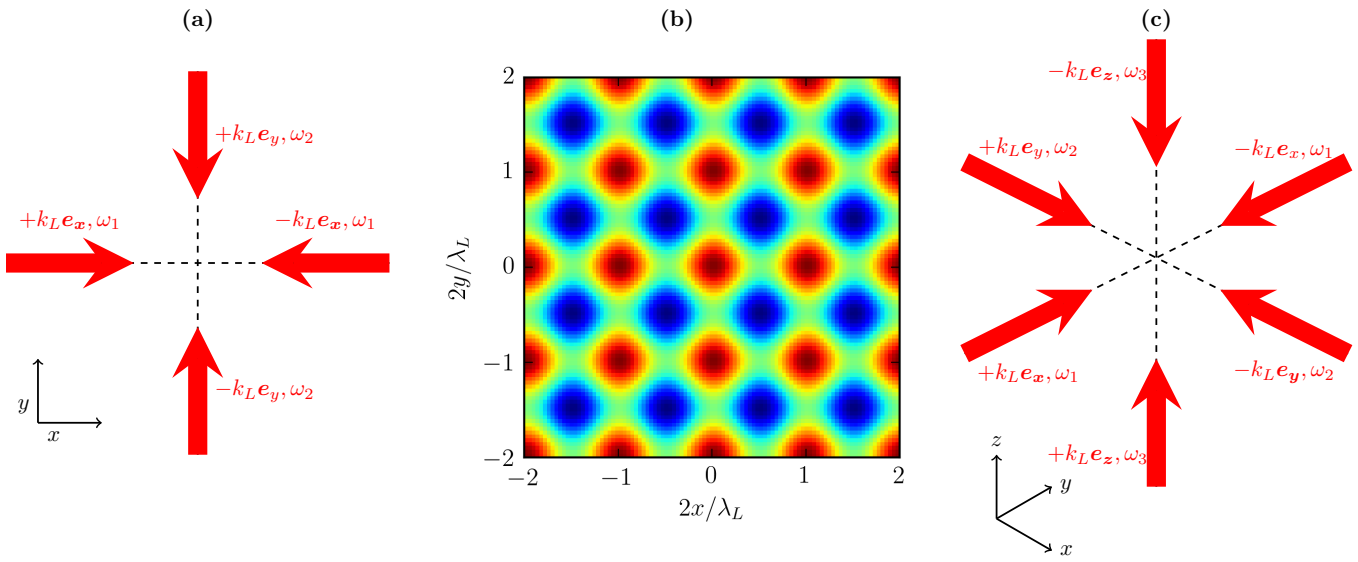

Figure 2.2.: **(a)**: Sketch of the laser arrangement to produce a 2D square lattice. The large red arrows indicate the laser wave vectors. **(b)**: Cut of the intensity seen by the atoms in the $x-y$ plane. The white circles locate the maxima (trapping sites for positive polarizability). **(a)**: Generalization to a 3D cubic lattice. The large red arrows indicate the laser wave vectors and the short black arrows their polarizations.

the horizontal and two along the vertical directions. The horizontal (vertical) beams have polarization $\boldsymbol{\epsilon}_1$ ($\boldsymbol{\epsilon}_2$), and the optical intensity is proportional to

$$|\boldsymbol{\mathcal{E}}(\boldsymbol{r})|^2 = \left|E_0 \cos(k_L x + \phi_x)\boldsymbol{\epsilon}_1 + E_0 \cos(k_L y + \phi_y) e^{i\phi_{xy}} \boldsymbol{\epsilon}_2\right|^2 . \tag{2.8}$$

For each direction, the relative phase of the beams ϕ_x and ϕ_y can be chosen to set the potential maximum at the origin. The remaining phase ϕ_{xy} is the relative phase between x and y, which is not fixed by the geometry. We show in Figure 2.3 that the potential landscape changes strongly with ϕ_{xy}. This does not seem very promising for an experimental implementation when taking into consideration that ϕ_{xy} is likely to suffer from uncontrolled changes: Atoms trapped in such a fluctuating potential will certainly heat up. We note that in principle, the interference pattern between the x and y beams can be cancelled by chosing the right polarizations, $\boldsymbol{\epsilon}_1 \perp \boldsymbol{\epsilon}_2$ (a generalization in three dimensions is indicated in Figure 2.2). This solution is not very stable in practice, at least if implemented passively: Polarizations tend to drift with the ambiant temperature and other environmental factors. Moreover, any deviation from perfect orthogonality (typically at the level of a few percent) leaves a residual modulation that can lead to heating.

Other geometries than square or cubic lattices are of course possible, from triangular or hexagonal lattices to more complex arrangements [1]. These geometries are created using several laser beams with well-chosen wavevectors, and generally suffer from the problem discussed above : The sensitivity to uncontrolled variations of the optical phases. A noticeable exception was pointed out by the group of Gilbert Grynberg [1]. They showed that in the special case where one uses the minimal number of plane waves (*i.e.* $D+1$ in D dimensions), the potential landscape becomes stable against changes of the relative phase: The latter only translates the potential as a whole as in 1 dimension. This allows one to realize triangular or honeycomb lattices in two dimensions (see Fig. 2.4 and [9, 10]).

In the more general case, there are several practical solutions for realizing a stable lattice geometry. The most straightforward one is to control the optical phases directly and stabilize them to a desired value using feedback control. For square lattices, the group of Ted Hänsch in Munich [11] devised an interferometric arrangement of the beams allowing to detect relative phase fluctuations and to cancel them actively using servo-loops. This method can be used to realize other lattice geometries, as for instance in [10, 12].

Another solution was found by the Munich group when studying Bose-Einstein condensates in such periodic potentials, and is now widely used in quantum gas experiments because of its simplicity and robustness. To ensure that cross-dimensional interference terms are negligible, one usually chooses slightly different frequencies[3] for the beams along x, y or z. Any remaining cross-dimensional term therefore oscillates at the frequency difference between the two interfering

[3]The frequencies differ typically by $\sim 100\,\mathrm{MHz}$, much less than the optical frequency ω_L ($|\Delta\omega_L|/\omega_L \sim 10^{-6}$). The beams are usually generated from the same parent beam, which is split and sent through independent acousto-optical modulators. These modulators shift their frequencies and also allow one to control their intensities independently. The change in the polarisability and in the wavevector magnitude can be neglected safely. Note that the technique only works for far-off resonant traps, where controlling precisely the laser frequencies is not important. The first experiments on optical lattices used near-resonant light, to provide cooling in addition to trapping the atoms. In this situation, the laser frequencies must be carefully chosen.

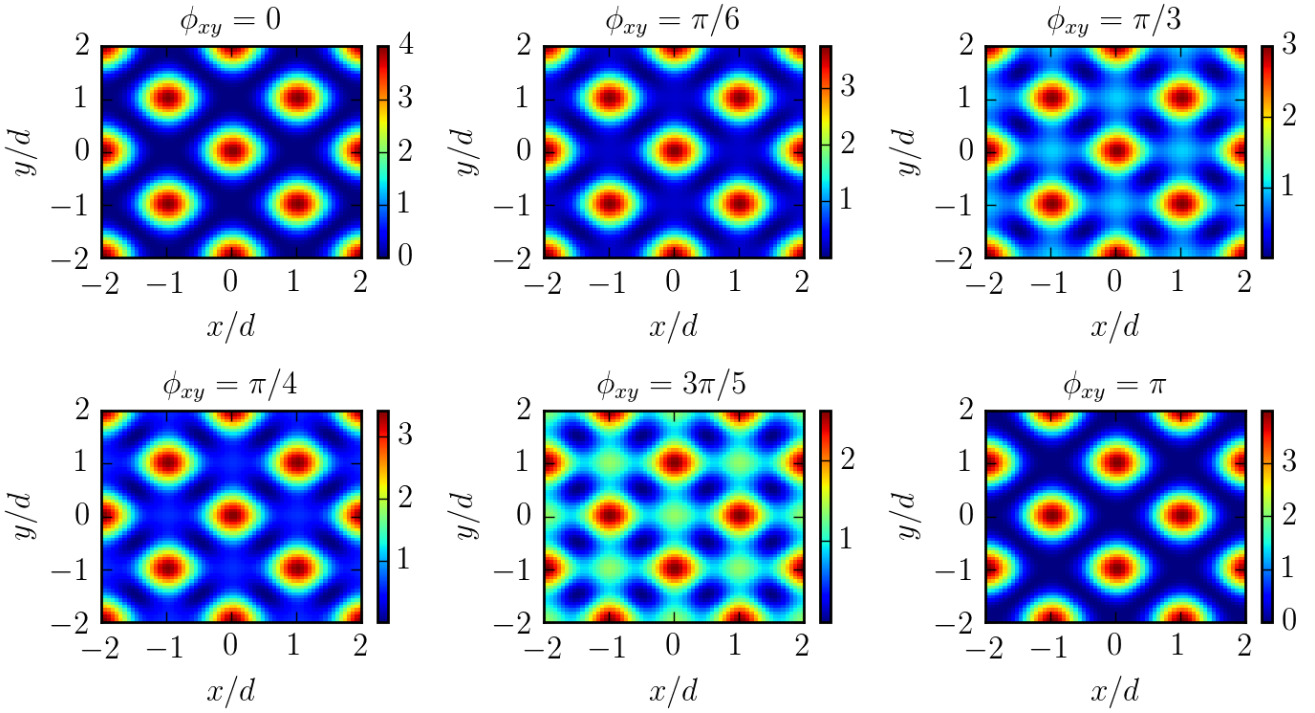

Figure 2.3.: Two-dimensional square lattice potential formed by four beams mutually coherent beams. The relative phase between the two horizontal (respectively vertical) beams is chosen to set the origin at $x = 0$ (resp. y=0). The relative phase ϕ_{xy} between the horizontal and vertical beam pairs is changing for each plot.

waves, which is extremely fast compared to the time scales of atomic motion. The result is that the atoms only feel the time-average of the potential, which is simply obtained by adding incoherently the potentials along each axis,

$$V_{2\mathrm{D}} = -\sum_{\alpha=1,\cdots,d} V_{0,\alpha} \cos^2\left(k_L x_\alpha + \phi_\alpha/2\right). \tag{2.9}$$

with $d = 2$ for a square lattice in two dimensions and $d = 3$ for a cubic lattice in three dimensions. Here ϕ_α denotes the relative phase of the beams creating the standing wave along axis α, that can be eliminated by a different choice for the origin of coordinates as in the 1D case.

2.2. Reminder on band theory

In this section, we refresh the main notions of band theory describing the motion of a quantum particle in a periodic potential. The reader can consult any reference book on solid state physics (*e.g.* [13]) or the 2013 Lecture at Collège de France by Jean Dalibard [14] for a more extensive treatment.

2.2.1. Bloch's theorem and Bloch's waves

We study first the simplest example, a standing wave in one dimension. The lattice is described by a potential which we rewrite as

$$V_{\mathrm{lat}} = V_0 \sin^2\left(k_L x\right), \tag{2.10}$$

so that the potential energy is zero at the potential minima. The natural unit for distance is the lattice spacing $d = \pi/k_L = \lambda_L/2$, the natural momentum is $(\hbar)k_L$ and the natural energy scale is the recoil energy $E_R = \hbar^2 k_L^2/2m_a$, with λ_L the wavelength of the laser creating the standing wave and m_a the atomic mass.

The lattice potential is invariant by a spatial translation of a multiple of the lattice spacing. This is expressed as $[\hat{T}_d, \hat{V}_{\mathrm{lat}}] = 0$, where $\hat{T}_d = \exp\left(i\hat{p}d/\hbar\right)$ is the operator that translates the position by d, $\langle x|\hat{T}_d|\phi\rangle = \phi\left(x + d\right)$ for any $|\phi\rangle$, and with $\hat{V}_{\mathrm{lat}} = V_{\mathrm{lat}}(\hat{x})$. Since the kinetic energy operator $\hat{p}^2/(2m_a)$ also commutes with $\hat{T}_d$, this amounts to

$$[\hat{T}_d, \hat{H}] = 0, \tag{2.11}$$

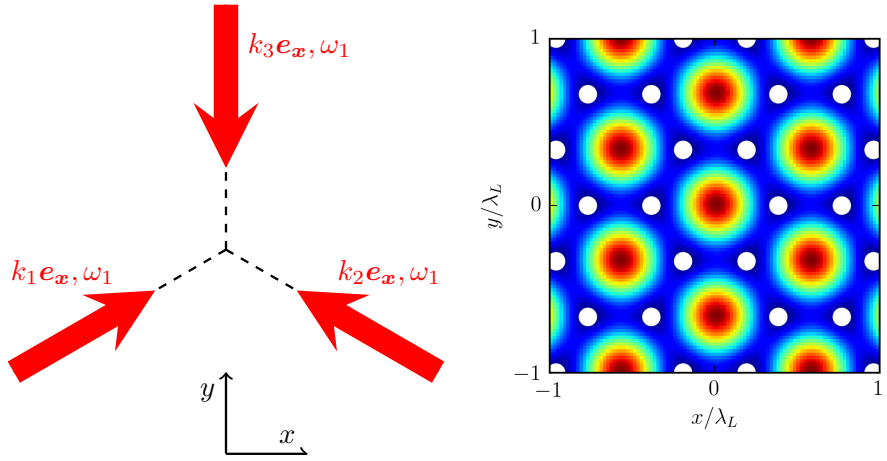

Figure 2.4.: **(a)**: Sketch of the laser arrangement to produce a 2D triangular or honeycomb lattice. The large red arrows indicate the laser wave vectors. **(b)**: Cut of the intensity seen by the atoms in the $x-y$ plane. The maxima of intensity are located on a triangular lattice, and the minima (marked by white dots) on a honeycomb (graphene-like) lattice.

with $\hat{H} = \hat{p}^2/(2m_a) + V_{\text{lat}}(\hat{x})$ the Hamiltonian. Therefore, one can find simultaneous eigenstates of the Hamiltonian and of $\hat{T}_d$. Since $\hat{T}_d$ is unitary, its eigenvalues have unit modulus and can be written as e^{iqd}, *i.e.* $\langle x|\hat{T}_d|\phi\rangle = e^{iqd}\phi(x)$ for an eigenstate $|\phi\rangle$. This implies that energy eigenstates are of the form

$$\phi_{n,q}(x) = e^{iqx} u_{n,q}(x), \tag{2.12}$$

where the $u_{n,q}$'s are periodic functions of space with period d. This is Bloch theorem. The usual terminology is to call the $\phi_{n,q}$'s Bloch waves and the $u_{n,q}$'s Bloch functions.

The label q is a quantum number imposed by symmetry considerations, with the quantity $\hbar q$ known as *quasi-momentum* (the other index n will be discussed shortly). The rest of the notes will use a slight abuse of language and use the term "quasi-momentum" for q. Changing the quasi-momentum by a multiple of $2\pi/d = 2k_L$ leads to the same eigenvalue of $\hat{T}_d$ and thus to the same state, *i.e.* $\phi_{n,q}(x) = \phi_{n,q+Q_m}(x)$ with $Q_m = 2mk_L$, $m \in \mathbb{Z}$.

In order to avoid double-counting states, one usually restricts the values of the quasi-momentum to the first Brillouin zone, defined for this simple case as $]-k_L, k_L]$. We will assume as usual for periodic problems a system of length $L = N_s d$ (N_s is thus the number of lattice sites) with periodic boundary conditions. This leads to quantized quasi-momenta, $q_p = (2\pi/L)p = (p/N_s) \times 2k_L$ with integer p as usual. This is the same trick as the finite volume usually introduced for plane waves in the continuum, to avoid dealing with energy-normalized continuum wave functions[4].

A better understanding of the physical significance of Bloch's theorem is gained by noting that since the potential (assumed sufficiently smooth) and the Bloch functions $u_{n,q}$ are periodic, they can be represented as Fourier series,

$$V(x) = \sum_{m\in\mathbb{Z}} \tilde{V}(m) e^{iQ_m x}, \tag{2.13}$$

$$u_{n,q}(x) = \sum_{m\in\mathbb{Z}} \tilde{u}_{n,q}(m) e^{iQ_m x}. \tag{2.14}$$

In the momentum representation, a Bloch wave with a well-defined quasi-momentum q is thus a superposition of plane waves at momenta $q + 2mk_L$ for all possible harmonics $m \in \mathbb{Z}$. One can reinterpret this fact by saying that an atomic matter wave interacts with the lattice potential by a virtual process where a photon is absorbed in one of the two traveling waves forming the lattice, and reemitted in the other one in a stimulated way. The net gain in momentum for this two-photon process (that can be repeated m times) is $\pm 2\hbar k_L$.

2.2.2. Band structure

Eqs. (2.13,2.14) are in fact very useful to find the actual spectrum and eigenfunctions. For the sinusoidal potential above, the expansion terminates at the first harmonic, $\tilde{V}(0) = V_0/2$, $\tilde{V}(\pm 1) = -V_0/4$. The Schrödinger equation for a

[4] A remark on the normalization of the Bloch waves : The normalization for $\phi_{n,q}$, $\int_0^L |\phi_{n,q}(x)|^2 dx = 1$, implies the condition $N_s \int_0^d |u_{n,q}(x)|^2 dx = 1$.

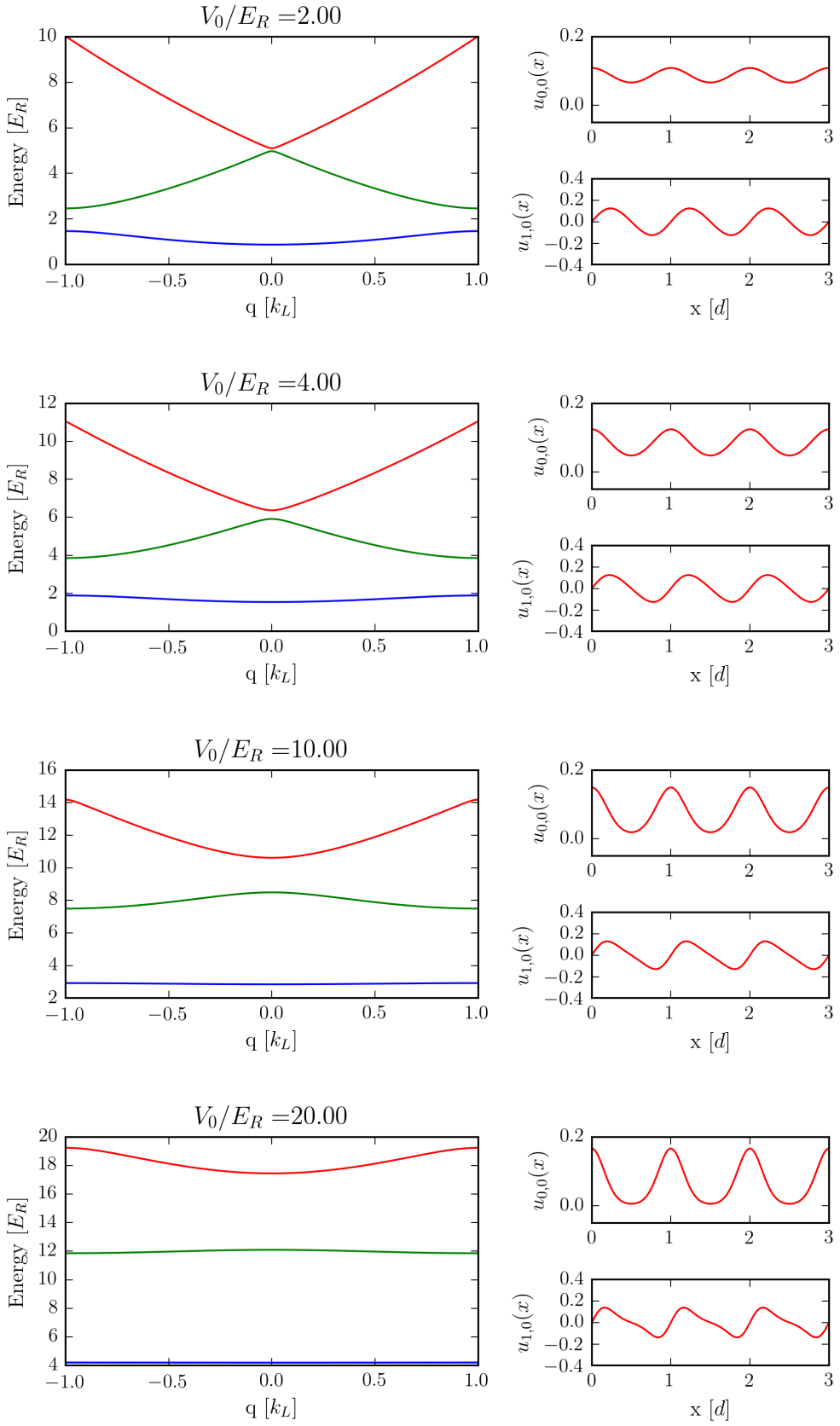

Figure 2.5.: Band structure of a 1D lattice, for several values of the lattice depth $V_0 = 2, 4, 10, 20\ E_R$ (from top to bottom). Left plot : Energy bands. Right plots : The Bloch functions $u_{n,q}$ for $n = 0, q = 0$ (upper plot) and $n = 1, q = 0$ (lower plot).

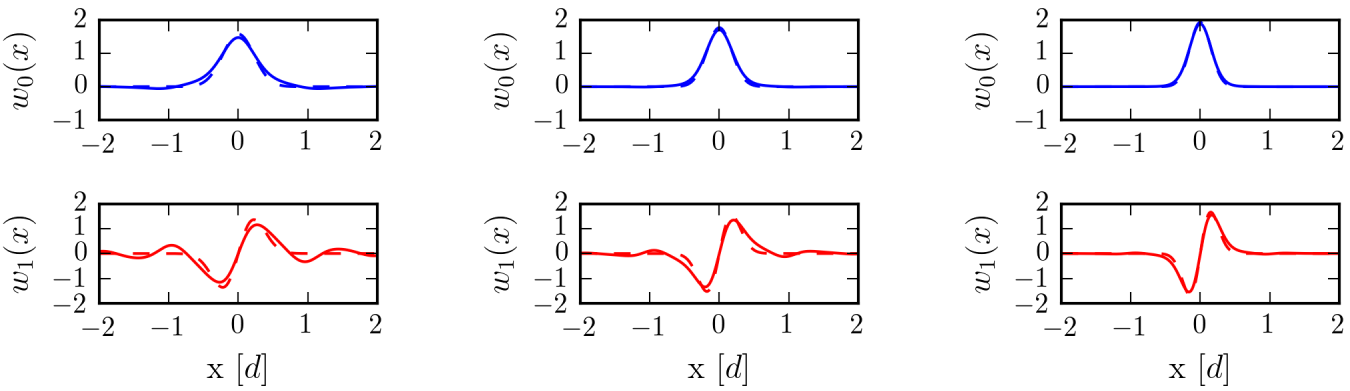

Figure 2.6.: Wannier functions centered at $x = 0$ for a 1D lattice for $V_0 = 4\ E_R$ (left),10 E_R (center), 20 E_R (right). We show the Wannier functions for the lowest band (blue lines) and for the first excited band (red lines). The solid lines show the exact functions computed numerically, and the dashed lines the harmonic oscillator approximation.

given q in the first Brillouin zone is then equivalent to the tridiagonal matrix equation

$$\begin{pmatrix} & \cdots & & & \\ \cdots & -\frac{V_0}{4} & \frac{\hbar^2(q+Q_{m-1})^2}{2m_a} & -\frac{V_0}{4} & 0 & \cdots \\ \cdots & 0 & -\frac{V_0}{4} & \frac{\hbar^2(q+Q_m)^2}{2m_a} & -\frac{V_0}{4} & \cdots \\ \cdots & 0 & 0 & -\frac{V_0}{4} & \frac{\hbar^2(q+Q_{m+1})^2}{2m_a} & \cdots \\ & & & \cdots & & \end{pmatrix} \cdot \begin{pmatrix} \cdot \\ \tilde{u}_{n,q}(m-1) \\ \tilde{u}_{n,q}(m) \\ \tilde{u}_{n,q}(m+1) \\ \cdot \end{pmatrix} = \left(\varepsilon_n(q) - \frac{V_0}{2}\right) \begin{pmatrix} \cdot \\ \tilde{u}_{n,q}(m-1) \\ \tilde{u}_{n,q}(m) \\ \tilde{u}_{n,q}(m+1) \\ \cdot \end{pmatrix}$$

with $\varepsilon_n(q)$ the eigenenergy. Practically, one truncates the plane wave basis to some maximum index $m_{\max}$ and diagonalizes the resulting matrix numerically.

As well-known [13], the energy spectrum obtained in this way splits into allowed and forbidden energy bands. The quantum number n (the "band index") allows one to label the allowed energy regions. Figure 2.5 shows the band structure for the sinusoidal potential in Eq. (2.10), together with examples of Bloch functions.

The case of the free particle is a special case with $V_0 = 0$. The state labeling in terms of quasi-momentum in the first Brilllouin zone, $q \in]-k_L, k_L]$, amounts to fold the free particle parabola around the points $(\pm n\pi/d, n^2 E_R)$, leading to $\varepsilon_n(q) = p^2/2m_a$ where q is the quasi-momentum, n the band index and $p = \hbar(q + 2nk_L)$ the true momentum. A weak lattice potential ($V_0 \ll 1\ E_R$) lifts the degeneracy near the edges of the Brillouin zone where two adjacent bands touch, introducing an energy gap $\propto V_0$ (the approximation of "weakly-bound electrons"). For cold atoms, this approximation is not terribly useful in practice because the interaction energy is usually on the order of E_R : it is then imperative to take interactions into account to obtain a sensible description of the system. The limit of large potential depths, where the interactions are a small perturbation compared to the band structure, is much more common in the experiments, and we are going to concentrate on it.

We note to conclude that for low quasi-momentum $q \ll k_L$, the band are approximately parabolic, $\varepsilon(q) \approx \hbar^2 q^2/2m^*$. The presence of the lattice is then hidden in the *effective mass* $m^* \leq m_a$, and the physics of non-interacting particles is otherwise similar to that in the continuum. As well-known from solid-state physics, the effective mass is often a useful concept to understand the propagation of wavepackets formed by superposing Bloch waves, or more generally transport experiments [13].

2.2.3. Wannier functions

The Bloch functions describe quantum states that are delocalized over the whole lattice, analogous to plane waves in the continuum. It is often convenient to use another basis, called Wannier basis, corresponding instead to wave functions localized around the lattice sites, which play the role of position eigenstates in the analogy.

The Wannier functions are defined by a discrete Fourier transformation of the Bloch wave functions with respect to the site locations,

$$w_n(x - x_i) = \frac{1}{\sqrt{N_s}} \sum_{q \in \mathrm{BZ1}} e^{-iqx_i} \phi_{n,q}(x). \tag{2.15}$$

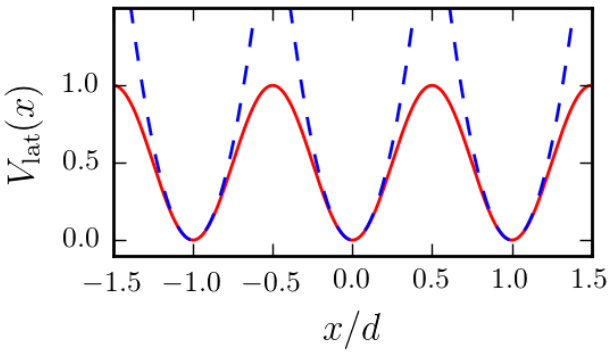

Figure 2.7.: Sketch of the lattice potential (solid line) and of the harmonic approximation near the bottom of each well (dashed line).

Here N_s is the total number of sites and BZ1 denotes the first Brillouin zone. The Wannier functions are orthogonal and normalized if the Bloch functions are,

$$\int w_n^*(x - x_i) w_m(x - x_j) dx = \delta_{n,m} \delta_{x_i, x_j}. \tag{2.16}$$

All Wannier functions can be deduced from each other by a simple translation by a lattice vector, as is clear from their definition. There are thus exactly N_s such functions per band (as many as Bloch functions). The relation above can be inverted,

$$\phi_{n,q}(x) = \frac{1}{\sqrt{N_s}} \sum_{x_i} e^{iqx_i} w_n(x - x_i). \tag{2.17}$$

As said before, the Wannier functions *can be chosen* to be well localized around each lattice site. There is some degree of arbitrariness in their definition. The global phase of the Bloch function can indeed be changed at will without modifying the result of the band structure calculation : $e^{i\gamma_{n,q}}\phi_{n,q}$ is a choice just as valid as $\phi_{n,q}$. Clearly, such a gauge transformation will change the associated Wannier function significantly. In one dimension, it can be shown that for a symmetric potential, *i.e.* one that fulfills $V(x) = V(-x)$, one can always choose the phase of the Bloch waves[5] in such a way that the Wannier functions are real, have a well defined parity (symmetric or anti-symmetric), and decay exponentially away from the site where they are maximum [15]. The problem can be more complicated in higher dimensions and for non-separable potentials [16].

2.2.4. Very deep lattices : disconnected harmonic wells

For deep lattice potentials ($V_0 \gg E_R$), one can see that the lowest energy energy bands become very flat. For the deeply bound bands (energies $\ll V_0$), the classical motion samples only the bottom of the potential wells, which can be locally approximated by an array of harmonic potentials centered near the lattice sites, and with the same curvature as the full lattice potential (see Figure 2.7),

$$V_{\mathrm{lat}}(x \approx x_i) \approx \frac{1}{2} m_a \omega_{\mathrm{lat}}^2 (x - x_i)^2, \quad \hbar\omega_{\mathrm{lat}} = 2\sqrt{V_0 E_R}. \tag{2.18}$$

The bands are centered near the energies $\overline{E}_n = (n + 1/2)\hbar\omega_{\mathrm{lat}}$ (see figures 2.5), such that the energy gap from the lowest to the first excited band is approximately given by $\hbar\omega_{\mathrm{lat}}$. The Wannier functions are well approximated by the corresponding harmonic oscillators wavefunctions (see Figure 2.6). For instance, the Wannier function for the lowest band is given by the gaussian ground state wavefunction,

$$w_0(x \approx x_i) \approx \frac{1}{\pi^{1/4}\sqrt{\sigma_{\mathrm{lat}}}} e^{-\frac{1}{2}\frac{(x-x_i)^2}{\sigma_{\mathrm{lat}}^2}}, \tag{2.19}$$

where $\sigma_{\mathrm{lat}} = \sqrt{\hbar/m_a\omega_{\mathrm{lat}}}$. Far away from the central site, the true Wannier functions decay exponentially (not as a Gaussian as predicted by the harmonic oscillator approximation) with additional oscillations around zero (see Figure 2.8).

[5] Specifically, this choice corresponds to $\sum_m \tilde{u}_{n,q}(m)$ real for even n and $\sum_m Q_m \tilde{u}_{n,q}(m)$ purely imaginary for odd n.

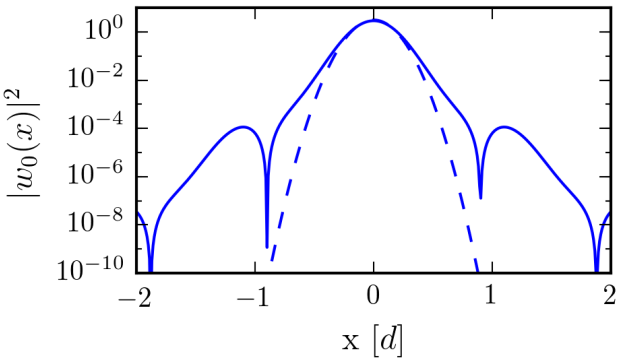

Figure 2.8.: Wannier function in logarithmic scale. The blue solid line shows the Wannier function centered at $x_i = 0$ and for the lowest band of a 1D lattice with depth $V_0 = 10\ E_R$, computed numerically. The dashed line shows the harmonic oscillator approximation.

The exponential decay is ensured by the choice of the phase of the Bloch waves, as discussed above, and the oscillations are required to ensure orthogonality of disjoint Wannier functions. One should thus keep in mind that the harmonic oscillator approximation, although useful for simple estimates, does not provide a complete description. In particular, it does not capture the residual curvature of the bands that remains even in the deeply bound limit, which corresponds to quantum tunneling through the potential barriers. To describe this, one needs to go beyond the harmonic oscillator approximation. This is the purpose of the next Section.

2.2.5. Tight-binding limit

The Hamiltonian is diagonal in the Bloch basis,

$$H = \sum_{n,q\in BZ1} \varepsilon_n(q)\hat{b}^\dagger_{n,q}\hat{b}_{n,q}. \tag{2.20}$$

Here, $\hat{b}_{n,q}$ is an annihilation operator for a particle in the Bloch state (n, q). In the Wannier basis, the Hamiltonian instead has off-diagonal terms

$$H = -\sum_{n,i,j} J_n(i-j)\hat{a}^\dagger_{n,i}\hat{a}_{n,j}, \tag{2.21}$$

with $\hat{a}_{n,i}$ the annihilation operator for a particle in the Wannier state $w_n(x - x_i)$ and with

$$J_n(i-j) = \int dx\ w^*_n(x-x_j)\left(\frac{\hbar^2}{2m_a}\Delta - V_{\text{lat}}(x)\right) w_n(x-x_i). \tag{2.22}$$

Due to the localized nature of the Wannier functions, one can interpret the matrix elements $J_n(i-j)$ as ($\hbar$ times) the characteristic rate to hop from one site at x_i to another one at x_j by quantum tunneling through the potential barriers. The tunneling energies $J_n(i-j)$ (also called hopping parameters) depend only on the relative distance $|x_i - x_j|$ between the two sites. They can also be expressed as a discrete Fourier transform of the band dispersion relation,

$$J_n(i-j) = \frac{1}{N_s}\sum_{q,q'\in BZ1} e^{-i(qx_i - q'x_j)} \int dx\ u^*_{n,q}(x)\left(\frac{\hbar^2}{2m_a}\Delta - V_{\text{lat}}(x)\right) u_{n,q'}(x), \tag{2.23}$$

$$= -\frac{1}{N_s}\sum_{q,q'\in BZ1} \varepsilon_n(q) e^{-i(qx_i - q'x_j)} \int dx\ u^*_{n,q}(x)u_{n,q'}(x), \tag{2.24}$$

$$= -\frac{1}{N_s}\sum_{q\in BZ1} \varepsilon_n(q) e^{-iq\cdot(x_i - x_j)}. \tag{2.25}$$

Without further approximation, this procedure is not helpful at all. It becomes interesting in the so-called *tight-binding* limit, where the lattice potential is very deep and the Wannier functions well-localized around each lattice site. In this limit, due to the exponential decay of the Wannier functions away from the central site, the tunneling energies $J_n(i-j)$'s fall off very rapidly with the distance $|x_i - x_j| = d|i-j|$ (see Figure 2.9). To a good approximation one can keep only the first few terms.

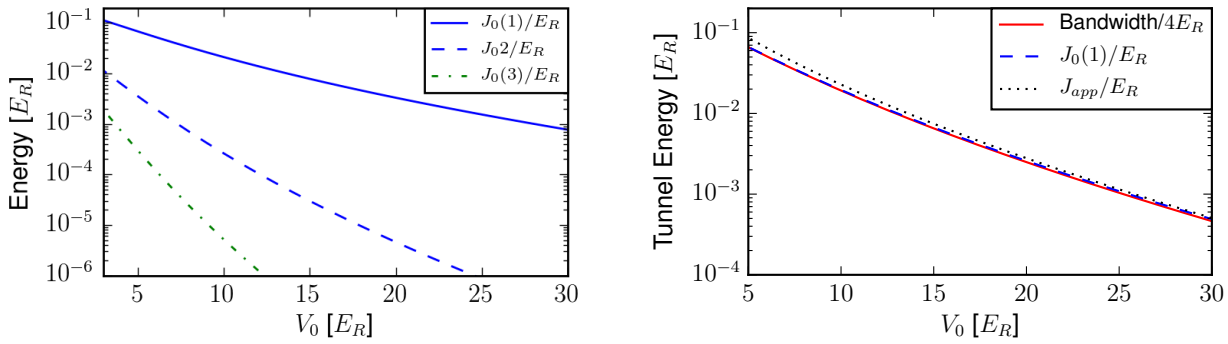

Figure 2.9.: Left plot: Comparison of the tunneling energies $J_0(|i-j|)$ in the lowest Bloch band. Right plot : Nearest-neighbor hopping $J_0(1) \equiv J_0$ (solid) compared to the width of the lowest band divided by 4 (dashed) and to the approximation Eq. (2.30).

The first term $J_n(0)$ is just (minus) the average energy of the band,

$$J_n(0) = -\frac{1}{N_s}\sum_k \varepsilon_n(k) = -\overline{E}_n. \tag{2.26}$$

Keeping only the first term, the bands are flat, which corresponds physically to unconnected wells without tunneling. This is the "harmonic oscillator limit" discussed before in Section 2.2.4, where $\varepsilon_n(q) \approx \hbar\omega_{\rm lat}(n+1/2)$.

The leading tunneling term is the one linking nearest neighbors, which we relabel as $J_n(1) \equiv J_n$. Keeping this additional term, we obtain the Hamiltonian (label "TB" for "tight-binding").

$$H_{TB} = \sum_{n,i} \overline{E}_n \hat{a}^\dagger_{n,i}\hat{a}_{n,i} - \sum_{n,\langle i,j\rangle} J_n \hat{a}^\dagger_{n,i}\hat{a}_{n,j}, \tag{2.27}$$

where the notation $\langle\cdot\rangle$ indicates that the sum has to be taken over nearest neighbours only. Going back to the Bloch basis, one readily finds that the band energies have a cosine form in the tight-binding limit. For instance, the dispersion in the lowest band is given by

$$\varepsilon_n(q) = -2J_0\cos(qx)\,. \tag{2.28}$$

The tight-binding bands have an energy width $4J_n$ determined by the nearest-neighbour tunneling energy[6].

If the atoms are cold enough, only the lowest band $n=0$ will be populated. Then, it is useful to adopt the point of view that J_0 is a parameter, that can be calculated explicitly from the lattice structure. The simplest option is to use the definition

$$J_0 = \int dx\; w_0^*(x+d)\left(\frac{\hbar^2}{2m_a}\Delta - V_{\rm lat}(x)\right) w_0(x)dx. \tag{2.29}$$

For the special case of the sinusoidal potential Eq. (2.10), an approximate formula is available [17],

$$\frac{J_0}{E_R} \approx \frac{4}{\sqrt{\pi}}\left(\frac{V_0}{E_R}\right)^{3/4} e^{-2\sqrt{\frac{V_0}{E_R}}}. \tag{2.30}$$

This agrees with the numerical result within 10 % from $V_0 = 4$ to 20 E_R (see Figure 2.9).

To summarize, the Bloch basis of energy eigenstates can be replaced by a Wannier basis of orthogonal wave functions well-localized in each well. The localized basis allows one to simplify a lot the treatment of interactions, which are dominated by local ("on-site") terms. We will use it extensively when discussing interacting gases in the next Chapter 3.

We conclude this Section by discussing the regime of validity of the tight-binding approximation. In practice (see below for a more detailed discussion), one also assumes that atoms are confined to the lowest band, and the population of the higher excited bands is negligible. This second approximation is typically more restrictive and requires sufficiently low temperatures and chemical potentials. If we consider that both are on the order of the bandwidth $4J_0$ of the lowest

[6] The tunneling energy cannot be computed from the harmonic oscillator approximation, since those predict bands with zero width. Alternatively, one can remark that the tunneling energy depends on the behavior of the Wannier functions below the potential barriers, where the harmonic approximation makes no sense.

band, then a criterion to neglect higher excited bands is $4J_0 \ll \Delta$, with $\Delta \approx \hbar\omega_{\rm lat}$ the gap to the first excited band. For a 1D lattice one has $\Delta/4J_0 \geq 10$ as soon as $V_0 \geq 5\ E_R$, which we can take as a lower limit for the validity of the TB approximation. Figure 2.9 shows that in this regime, tunneling terms beyond nearest-neighbors are smaller than J_0 by at least one order of magnitude.

atom	^{87}Rb
mass m_a	$1.45 \cdot 10^{-25}$ kg
Lattice wavelength λ_L	850 nm
Recoil energy E_R/h	≈ 3.15 kHz (≈ 150 nK)
on-site oscillation frequency $\omega_{\rm lat}/2\pi$ for $V_0 = 10\ E_R$	≈ 19.9 kHz
nearest-neighbor tunneling J/E_R for $V_0 = 10\ E_R$	$\approx 1.9 \cdot 10^{-2}$

Table 2.2.: Typical parameters for the experiment of [18].

2.2.6. Square and cubic lattices

The discussions of the previous section apply almost directly to square (in two dimensions) and cubic (in three dimensions) optical lattices, formed by superimposing two or three independent standing waves. For simplicity we assume here that the potential depths along each direction are equal. The total potential is separable, and the energy bands are given by

$$\epsilon_{\mathbf{n}}(\mathbf{q}) = \sum_{\alpha=x,y,z} \epsilon_{n_\alpha}(q_\alpha), \tag{2.31}$$

with $\epsilon_n(q)$ the 1d dispersion relation, with $\mathbf{n}$ a triplet of integers indexing the various bands[7] and with $\mathbf{q}$ the quasi momentum. The first Brillouin zone is $]-\pi/d, \pi/d]^3$. The eigenfunctions are obtained by taking the product of eigenfunctions in each direction,

$$\phi_{\mathbf{n},\mathbf{q}}(\mathbf{r}) = e^{i\mathbf{q}\cdot\mathbf{r}} u_{n_x,q_x}(x) u_{n_y,q_y}(y) u_{n_z,q_z}(z). \tag{2.32}$$

Wannier functions can be introduced similarly as in one dimension, leading to

$$W_{\boldsymbol{n}}(\mathbf{r} - \mathbf{r}_{\boldsymbol{m}}) = w_{n_x}(x - m_x d_x) w_{n_y}(y - m_y d_y) w_{n_z}(z - m_z d_z). \tag{2.33}$$

Generalizing to more complex lattice geometries require to introduce the machinery of Bravais lattices and crystallographic notations, which will not be needed in these notes. We refer the reader to any solid textbook on solid-state physics, for instance [13].

2.3. Thermodynamics of ideal gases in a cubic lattice

2.3.1. Bosons

Given a system of N bosons at temperature T, characterized by a single-particle energy spectrum $\{\epsilon_\nu\}$, thermodynamic quantities can be derived from the grand partition function

$$\ln\Theta = -\sum_\nu \ln\left[1 - z e^{-\beta\epsilon_\nu}\right], \tag{2.34}$$

with the fugacity $z = e^{\beta\mu}$ and the inverse temperature $\beta = 1/k_B T$. For instance, the mean number of particles and mean energy can be found from

$$\overline{N} = \frac{1}{\beta}\frac{\partial \ln\Theta}{\partial \mu} = \sum_\nu \frac{1}{e^{\beta(\epsilon_\nu - \mu)} - 1}, \tag{2.35}$$

$$\overline{E} = -\frac{\partial \ln\Theta}{\partial \beta} = \sum_\nu \frac{\epsilon_\nu}{e^{\beta(\epsilon_\nu - \mu)} - 1}. \tag{2.36}$$

The chemical potential μ is chosen to ensure that the first equation holds for given T and N. Since the Bose occupation numbers must stay finite, one has $\mu \leq \epsilon_0$, or $0 \leq z \leq 1$, with ϵ_0 the lowest single-particle energy. For high temperatures,

[7] For instance, the lowest band is indexed by $\mathbf{n} = (0,0,0)$ and the first excited band is triply degenerate with $\mathbf{n} = (1,0,0), (0,1,0), (0,0,1)$.

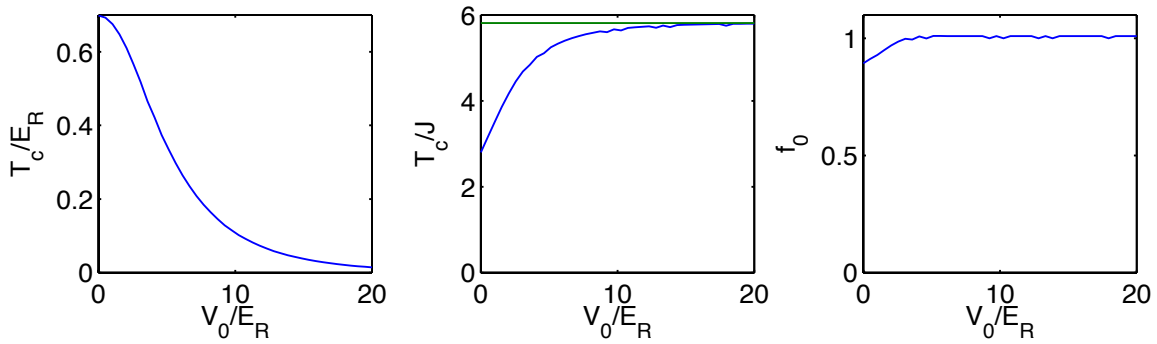

Figure 2.10.: Left: Critical temperature T_c for an ideal Bose gas in a 3D cubic lattice. Middle: The same in units of J_0, the nearest-neighbor tunneling energy in the lowest band. The blue line is calculated numerically, and the red line shows the tight-binding approximation. Right: fraction of atoms in the lowest band N_0/N at the critical point.

the gas is in a thermal regime where μ is large and negative: The Bose-Einstein distribution then reduces to Maxwell-Boltzmann statistics. When T decreases, the chemical potential gradually approaches the lowest single-particle energy. When $\mu = \epsilon_0$, the total population in the excited states N' saturates, and a Bose-Einstein condensate forms as the temperature is further lowered. This description of BEC as a saturation of the population in the excited states is completely general for a non-interacting gas. However the fact that it is possible or not to saturate this population at finite temperatures depends on the dimensionality and of the potential. For instance, in two dimensions, a gas of bosons in a box does not show BEC, but a gas in a harmonic trap does (see for instance [19]).

We now apply the general formalism to a gas of N bosons experiencing the band structure of a 3D cubic lattice. We first try to identify the critical temperature T_c below which our gas undergoes Bose-Einstein condensation in the lowest energy Bloch state ($\mathbf{n} = 0, \mathbf{q} = 0$). The atom number is given by

$$N = \sum_{\mathbf{n},\mathbf{q}} \frac{1}{e^{\beta(\epsilon_{\mathbf{n}}(\mathbf{q})-\mu)} - 1} = \left(\frac{L}{d}\right)^3 \sum_{m=0}^{+\infty} z^m \left(\sum_{n_x} \int_{\mathrm{BZ1}} \frac{d(q_x d)}{2\pi} \, e^{-m\beta\epsilon_{n_x}(q_x)} \right)^3 . \tag{2.37}$$

It is convenient to express this in terms of filling fraction, or equivalently number of particles per lattice site,

$$\overline{n} = \frac{N}{N_s} = \rho d^3, \tag{2.38}$$

with ρ the average spatial density and $N_s = (L/d)^3$. We also exclude the contribution of the lowest energy state from the sum (indicated by a $'$ subscript). We thus have

$$\overline{n}' = \frac{N'}{N_s} = \sum_{m=0}^{+\infty} z^m \left(\sum_{n_x} \int_{\mathrm{BZ1}} \frac{d(q_x d)}{2\pi} \, e^{-m\beta\epsilon_{n_x}(q_x)} \right)^3 . \tag{2.39}$$

The critical temperature for Bose-Einstein condensation is found by setting $z = 1$ in Eq. (2.39) and solving for $\beta_c = 1/k_B T_c$.

Typical experiments correspond to filling fractions on the order of $1 - 3$ at most. Although higher filling fractions are possible in principle, it turns out that they lead in practice to very high spatial densities $n > 10^{15}$ at/cm^3. For such high densities, three-body recombination of atoms into molecules become very frequent and limit the lifetime of the atoms in the trap[8]. For concreteness, we consider here a system with unit filling $\overline{n} = 1$. The result using the band structure calculated numerically is shown in Figure 2.10: T_c decreases quickly with lattice depth, and tends to a constant times the bandwidth J_0 of the lowest band.

An essential point is that as one increases the lattice depth (staying at the critical temperature T_c), the atoms gather very quickly into the lowest lattice band (right plot in Figure 2.10). This can be understood by considering how the band structure evolves: For $V_0 = 0$, the "band structure" is given by the free particle parabola $\epsilon_{n_x}(q_x) = \hbar^2 k_x^2/2m_a$ for a momentum along x $k_x = q_x + 2n_x k_L$. The critical temperature for a gas in a box is $k_B T_c^{(\mathrm{box})} = 2\pi\hbar^2\rho^{2/3}/(m_a \zeta(3/2)^{2/3})$,

[8] The molecule formed after the recombination and the third atom have a kinetic energy on the order of the binding energy to fulfill energy conservation, and this is typically very large compared to the trap depth. Weakly bound molecules near a Feshbach resonance can be an exception.

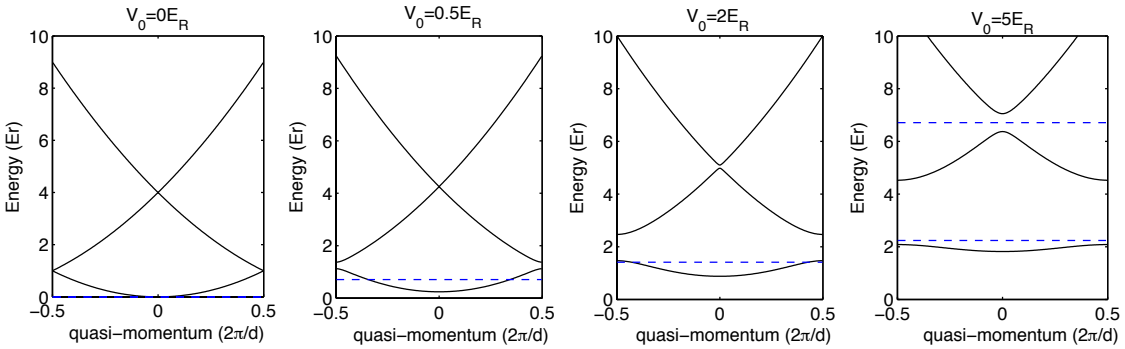

Figure 2.11.: Modification of the band structure as V_0 increases from zero to 5 E_R. Atoms initially prepared in the lowest branch of the parabola mostly stay in the lowest band. The dashed blue lines show the harmonic oscillator approximation.

with ρ the particle density. Using $\rho d^3 = \overline{n}$, this can be rewritten as

$$k_B T_c^{(\mathrm{box})} = \frac{4E_R}{\pi}\left(\frac{\overline{n}}{\zeta(3/2)}\right)^{2/3}, \tag{2.40}$$

leading to $T_c^{(\mathrm{box})}/E_R \approx 0.68$ for $\overline{n} = 1$. Thus, assuming one starts with a Bose gas right at $T = T_c$, most of the atoms reside initially in the lowest part of the parabola with energy $\leq E_R$. As one increases V_0, this branch turns into the lowest Bloch band (as illustrated in Figure 2.11), and the atomic distribution mostly follows the evolution of the single-particle energies and stay within that band. Note that the same reasoning can also be applied for filling fractions $\overline{n} \gg 1$, where it predicts that excited bands will be populated.

For a deep lattice ($V_0 \gg E_R$), the equations above can be simplified by assuming from the start that all atoms are confined to the lowest Bloch band, and by further making the tight-binding approximation. This gives

$$\overline{n}_{\mathrm{TB}} \approx \sum_{m=0}^{+\infty} z^m \left(\int_{-\pi}^{\pi} \frac{du}{2\pi}\, e^{2m\beta J_0[\cos(u)-1]}\right)^3 = \sum_{m=0}^{+\infty} \left(ze^{-6\beta J_0}\right)^m I_0(2m\beta J_0)^3, \tag{2.41}$$

with I_0 a Bessel function of the second kind,

$$I_0(x) = \frac{1}{2\pi}\int_{-\pi}^{\pi} e^{x\cos(\theta)} d\theta. \tag{2.42}$$

The density (and in fact, all thermodynamic functions) depend on two variables, the fugacity z and the temperature T/J_0 expressed in units of the width of the lowest Bloch band (or equivalently, in terms of the nearest-neighbour tunneling energy). This implies that the critical temperature, $T_c/J_0 = f(\overline{n})$, depends only on the filling fraction $\overline{n}$. For $\overline{n} = 1$, the numerical result is $f(1) \approx 5.8$. For $\overline{n} \ll 1$, the critical temperature becomes low so that at the critical point the atoms occupy mostly the bottom of the lowest Bloch band. The tight-binding dispersion relation simplifies to $\varepsilon_0(q_x) \approx -2J_0 + J_0 d^2 q_x^2$. Therefore, the atoms behave as a gas of free particles with effective mass m^* such that $\hbar^2/2m^* = Jd^2$. The critical temperature is thus approximately given by

$$k_B T_c^{(\mathrm{TB})} \approx \frac{2\pi\hbar^2}{m^*}\left(\frac{\rho}{\zeta(3/2)}\right)^{2/3} \approx 6.6 J \overline{n}^{2/3}. \tag{2.43}$$

We conclude that, as a rule of thumb, the critical temperature for a sufficiently deep lattice and filling close to one is approximately given by $k_B T_c \sim 6J_0$ where the factor of 6 coincides with the number of nearest neighbours for a cubic lattice.

2.3.2. Isentropic loading

Evaporative cooling is an essential method enabling the preparation of quantum gases in (typically) harmonic traps. However, the method no longer works once the atoms are trapped in the optical lattice. When the gas is held in a harmonic trap, the evaporation rate depends on the population of states near the trap threshold, $\Gamma_{\mathrm{ev}} \sim e^{-V_0/k_B T}$, with $V_0/k_B T \sim 5 - 12$ in typical experiments. If we are interested in a quantum gas in an optical lattice, cold enough that most of the atoms occupy the lowest band, the population of the band n is proportional to $p_n \sim e^{-\overline{E}_n/k_B T}$, with $\overline{E}_n$ the mean energy of the band and T the temperature. For a quantum gas in the lowest band, we can estimate

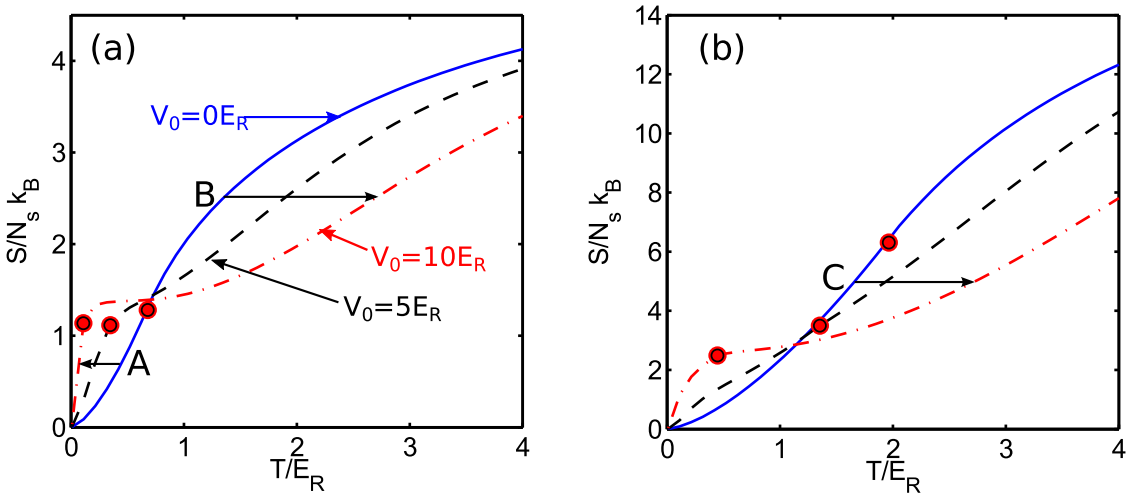

Figure 2.12.: Entropy-temperature curves for filling fraction $\overline{n} = 1$ (**(a)**) and $\overline{n} = 5$ (**(b)**) calculated for lattice depths $V_0 = 0, 5, 10\ E_R$ (solid, dashed and dash-dotted lines). The red circles show the location of the critical points where Bose-Einstein condensation occurs. The path A,B,C show different scenario for loading into the lattice at constant entropy : A corresponds to isentropic cooling, B to isentropic heating and C to a process where the gas uncondenses isentropically.

roughly that the temperature will be set by the bandwidth $\sim J_0$, leading to $p_n \leq e^{-a\overline{E}_n/J_0}$ with a some number. It is clear from the band structure calculations that this will be extremely small for lattice depths of a few E_R[9]. Since evaporative cooling is inefficient, the best one can do is to prepare a quantum gas prepared in a regular harmonic trap well below the degeneracy temperature, and to transfer this gas adiabatically into the lattice potential by gradually ramping up the lattice depth from zero to the desired final value.

At this point, we deviate slightly from the main topic to comment on the notion of adiabaticity. In Physics, this word can have two non-equivalent meaning. In Thermodynamics (classical or quantum), an adiabatic process is one where no heat is exchanged between the system and a surrounding heat bath (or to put it differently, this is a process that can be performed reversibly since only work is involved). For a thermodynamic adiabatic process, the entropy remains constant through the process[10]. In Quantum Mechanics, on the other hand, adiabaticity is linked to the quantum adiabatic theorem (see [20] and the appendix C). This theorem concerns the evolution in time of a quantum system when the Hamiltonian is time-dependent, $H(t)$, but varies arbitrarily slowly with some characteristic speed $\dot{H}$. Loosely speaking, it states that if a system is initially prepared in an eigenstate of $H(t = 0)$, say $|a(0)\rangle$, which remains well-isolated from other levels at all times (no level crossing), then the probability to find the system in $|a(t)\rangle$ tends to 1 as $\dot{H} \to 0$. This behaviour is usually termed "adiabatic following", since the instantaneous wave function follows the evolution of the energy eigenstates. The thermodynamical and quantum-mechanical adiabaticity are in general different, although the latter implies the former. To see this, we note that the statistical entropy of an equilibrium gas can be written as

$$S = -k_B \sum_\nu p_\nu \ln(p_\nu), \tag{2.44}$$

where p_ν is the probability to find the system in an energy eigenstate indexed by ν. Taking the time derivative, we see that (using $\sum_\nu \frac{dp_\nu}{dt} = 0$),

$$\frac{dS}{dt} = -k_B \sum_\nu \frac{dp_\nu}{dt} \ln(p_\nu). \tag{2.45}$$

Thus, $\frac{dp_\nu}{dt} = 0$ implies $\frac{dS}{dt} = 0$ (quantum-mechanical adiabaticity implies thermodynamical adiabaticity), but the converse is not true. In particular, the quantum adiabatic theorem cannot be used if the initial state is degenerate, or if degeneracies arise in the course of the evolution (*i.e.* level crossings occur). For many-body systems, the norm is to have many degenerate states and adiabaticity must be considered with care.

[9] Referring to Fig. 2.9, one has $J_0 \sim 10^{-2} E_R$ and $\overline{E}_0 \sim 7$ for $V_0 = 10\, E_r$, leading to $\overline{E}_n/J_0 \sim 700$, far greater than the corresponding factor $V_0/k_BT \sim 5 - 12$ for a purely harmonic trap.

[10] This allows to characterize such a process even when there is no heat bath.

In this Sectione first consider the adiabatic transfer of an ideal Bose gas into the 3D lattice potential in the thermodynamical sense, which we will call *isentropic loading* to avoid confusion. The term *adiabatic loading* will be reserved to adiabaticity in the quantum mechanical sense, which will be studied next in Section 2.4.1. We follow closely the discussion in [21]. The gas starts in a box-like potential, at some initial temperature T_i with some characteristic density $\overline{n}$. This is supposed to model an ultracold atomic gas cooled down using evaporative cooling. The initial entropy per site is given by

$$\frac{S_i}{N_s k_B} \approx -\overline{n} \ln\left(\frac{\overline{n}\lambda_{\text{th}}^3}{d^3}\right) \quad (T \gg T_c), \tag{2.46}$$

$$\approx 1.28\overline{n}\left(\frac{T}{T_c}\right)^{3/2} \quad (T \leq T_c). \tag{2.47}$$

For high temperatures, the entropy per site is large compare to unity since the phase-space density $\overline{n}\lambda_{\text{th}}^3/d^3 = \rho\lambda_{\text{th}}^3 \ll 1$. Close to T_c, $S_i/N_s k_b$ is on the order of the filling $\overline{n}$. The coldest clouds that can be produced by evaporative cooling have condensed fractions > 90 %, corresponding to temperatures $\sim 0.1T_c$ and entropy per site $\sim 0.05k_B$ for our box model[11].

Since we assume that entropy is conserved during the loading process, we can determine the temperature in the final state if we know the relation $S(T_f)$ in presence of the lattice potential and solve $S(T_f) = S_i$ for T_f. From the definition of the Gibbs free energy, $G = U - TS - \mu N = -k_B T \ln \Theta$, and the results of Section 2.3.1, one can compute the entropy in the final state as

$$\frac{S}{k_B} = \beta\left(U - \mu N\right) + \ln \Theta. \tag{2.48}$$

Figure 2.12 shows the result of this calculation for a Bose gas in a cubic lattice for various lattice depths and constant filling factor. The red circles mark the location of the critical point where a BEC appears. We consider for concreteness an increase of the lattice depth from $V_0 = 0$ to $V_0 = 10\ E_R$. An isentropic path corresponds to a horizontal line in the $S - T$ diagram, and generally results in a final temperature T_f different from the initial one T_i. As can be seen in Figure 2.12a, if the gas is initially below the BEC transition (path A), isentropic loading results in a reduction of the final temperature ($T_f < T_i$). Loading into the lattice results in *isentropic cooling* in this case. On the contrary, if the gas starts above the BEC transition, *isentropic heating* will occur (path B).

The frontier between these two behavior correspond to a common point through which the $S - T$ isentropic curves approximately pass. For temperatures/entropies below that point, one notices a plateau where the entropy remains approximately constant with temperature, before dropping to zero. We can understand this behavior from using an elementary argument. The maximum entropy that the lowest band can accommodate is reached for equal population of each Bloch states in that band. Equivalently, this is achieved in a regime of temperatures much greater than the bandwidth (so that all occupation numbers in this band are approximately equal independently of quasi-momentum), but still much smaller than the band gap to the first excited bands (so that the occupation numbers outside of the lowest band are very small)[12]. In the lowest Bloch band, we have already noticed that there are N_s independent single-particle states. The number of possible ways to distribute N bosons among N_s degenerate sites is thus

$$\Omega = \frac{(N_s + N - 1)!}{N!(N_s - 1)!}. \tag{2.49}$$

Using Stirling's formula, we find the entropy per site

$$\frac{S}{N_s k_B} \approx \overline{n}\ \ln\left(1 + \frac{1}{\overline{n}}\right) + \ln\left(1 + \overline{n}\right). \tag{2.50}$$

This formula gives $\frac{S}{N_s k_B} = 2\ln 2 \approx 1.39$ for $\overline{n} = 1$, and $\frac{S}{N_s k_B} \approx 2.70$ for $\overline{n} = 5$, which reproduces the value of the entropy plateau computed directly.

2.3.3. Fermions

We mention very briefly the case of single-component fermionic gases. Due to the low temperatures, $p-$wave collisions are suppressed, and $s-$wave collisions are forbidden by the Pauli principle. The total atom number is determined by the temperature T and the chemical potential according to

$$N(T, \mu) = \sum_{\mathbf{n},\mathbf{q}} \frac{1}{e^{\beta(\epsilon_{\mathbf{n}}(\mathbf{q}) - \mu)} + 1} \tag{2.51}$$

[11] In actual experiments, atoms are confined in harmonic traps and interactions affect the thermodynamics. These additional effects do not change the qualitative conclusions obtained in this Section, but should be accounted for a quantitative description of experimental results.

[12] Note that this is only possible in the tight-binding limit where the bandwidth is very small compared to the gap.

In the limit where $k_B T \ll \mu$, the Fermi-Dirac distribution tends to the zero temperature limit where all states are occupied up to an energy threshold set by $\mu \equiv E_F$, the Fermi energy,

$$N(T=0, \mu = E_F) = \sum_{\mathbf{n},\mathbf{q}} \Theta \left[E_F - \epsilon_{\mathbf{n}}(\mathbf{q}) \right], \tag{2.52}$$

with Θ the Heaviside step function. For a fixed filling fraction $\overline{n} = N/N_s$, this equation allows one to deduce the Fermi energy E_F. This leads to "metallic" states for partially filled bands ($\overline{n} \neq$ integer)and "band insulators" for completely filled bands ($\overline{n} =$ integer), in analogy with the solid-state terminology [13]. Isentropic transfer from a cloud prepared by evaporative cooling (using a mixture with another atomix species or with another spin state of the same species, the "secondary" species being removed from the trap before ramping up the lattice) could be studied in the same way as we did for bosons. Note that by increasing the number of particles it is much easier to fill isentropically higher excited bands for fermions than for bosons, as the latter tend to cluster together in the lowest band.

2.4. Dynamics of a Bose-Einstein condensate in an optical lattice : Adiabatic loading, time of flight expansion and band mapping

The discussion of the last Section showed that a non-interacting quantum gas can be transferred at constant entropy into the optical lattice potential. In the remainder of this Chapter, we will consider that $T = 0$. Of course, this situation is never strictly realized in experiments. However it is a good approximation when one starts from a gas where almost all atoms belong to the condensate. The initial entropy is then negligibly small and can be ignored to a first approximation.

2.4.1. Adiabatic loading

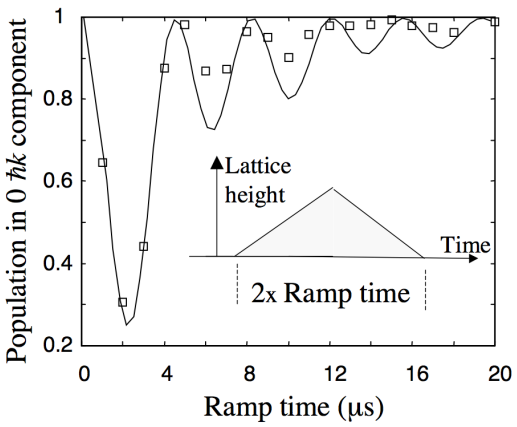

Figure 2.13.: Non-adiabatic loading of a Bose-Einstein condensate in a one-dimensional optical lattice. Here the condensate is prepared in a narrow wave packet near momentum $k_0 = 0$ without lattice, corresponding to $q_0 \approx 0$ and $n_0 = 0$. The population remaining in the initial momentum state is monitored after ramping up and down the lattice using a triangular ramp with varying ramp times (inset). The maximum lattice depth is $V_{0,\mathrm{f}} = 14\ E_R$.

We now ask whether the optical lattice potential can be increased adiabatically from zero in the quantum-mechanical sense, which is a stronger requirement than the isentropic loading studied before. For bosons this is the proper criterion at very low temperatures, where almost all atoms condense in the same state. Since we are treating ideal gases in this Chapter, all atoms are expected to condense into the single-particle ground state at $T = 0$. It is thus sufficient to consider a single atom initially in free space ($V_{0,i} = 0$) in momentum state k_0. At time $t = 0$, one starts ramping up the lattice potential to a final value $V_{0,f}$. We take for simplicity a linear ramp, $V_0(t) = V_{0,f} t/T_{\mathrm{ramp}}$ (in a real experiment choosing a function smoother for low lattice depths is better). Importantly, the time dependence enters only in a scale factor for the potential, which remains periodic in space with the same period at all times (the lattice translation operator commutes with $H(t)$ at all times). Therefore the quasi-momentum is conserved, Bloch theorem applies, and the Bloch wave functions are the eigenstates of the Hamiltonian at all times (including $t = 0$ when there is no lattice). The band index, however, can change. We can estimate the time scale over which inter-band transitions

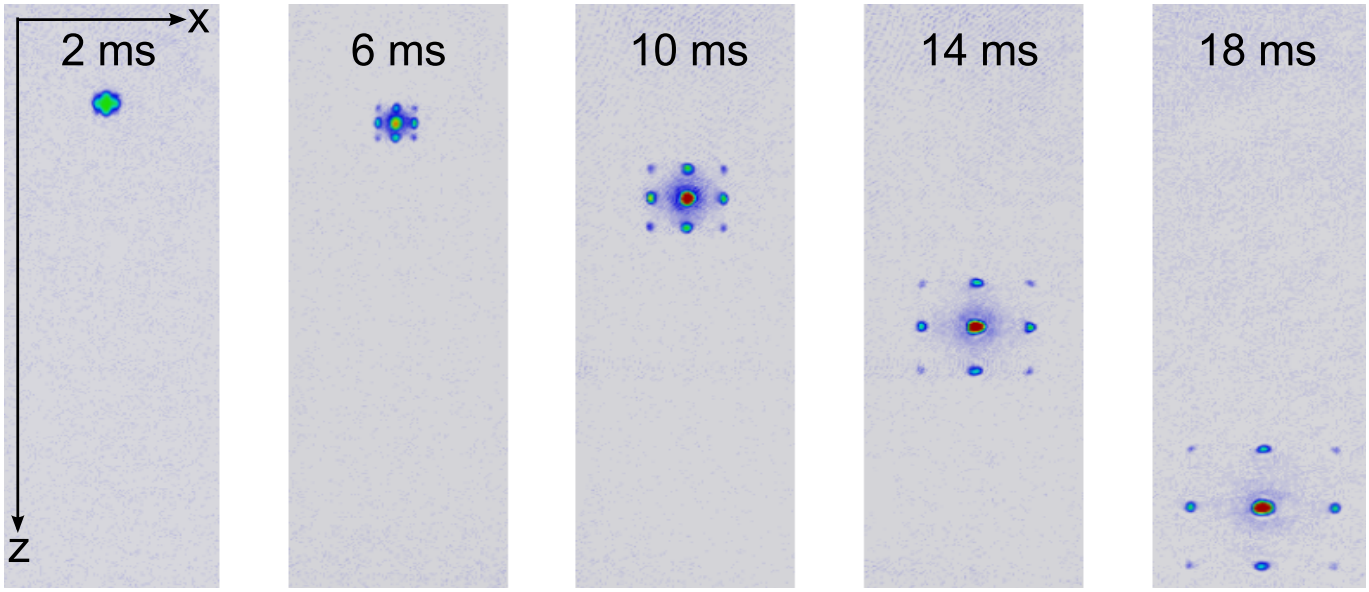

Figure 2.14.: Absorption images of expanding Bose-Einstein condensates released from a 3D cubic lattice. The t.o.f. is indicated for each picture, z is the direction of gravity. [Figure courtesy of I. Bloch].

become important using the approximate adiabaticity criterion given in Appendix C (see also [20]),

$$\left|\langle\phi_{n,q_0}|\dot{V}_0|\phi_{m,q_0}\rangle\right| \ll \frac{\left(\varepsilon_m(q_0)-\varepsilon_n(q_0)\right)^2}{\hbar}. \tag{2.53}$$

A typical ramp time for $q_0 = 0, n_0 = 0$ can be estimated by noting that the energy difference is always larger than $4E_R$ (the value for $V_0 = 0$). The most restrictive condition is thus obtained for shallow lattices,

$$\left|\dot{V}_0\right| = \frac{V_{0,\mathrm{f}}}{T_{\mathrm{ramp}}} \ll \frac{16E_R^2}{\hbar}, \tag{2.54}$$

leading to $T_{\mathrm{ramp}} \gg \hbar V_{0,\mathrm{f}}/16E_R^2$. For Rubidium atoms and the parameters in Table 2.2 and $V_{0,\mathrm{f}} = 10\ E_R$, this translates to $T_{\mathrm{ramp}} \gg 80\ \mu$s.The experiments shown in Figure 2.13 are done with Sodium atoms and a lattice wavelength near 589 nm ($E_R/h \approx 25$ kHz). This gives $T_{\mathrm{ramp}} \gg 5\ \mu$s. This highlights that actual time scales can strongly differ from one experiment to the next, due to the difference in the intrinsic energy scale E_R that depend on atomic mass and lattice wavelength. We note that for a quasi-momentum at the edge of the Brillouin zone, $q_0 = \pm k_L$, the rhs vanishes for vanishing lattice depths. Hence in that case the adiabaticity criterion can never be fulfilled. For $q_0 \neq \pm k_L$, the rhs is always non-zero so that adiabaticity can be maintained for long enough ramp times. We thus conclude that adiabatic loading is possible if the initial state is sufficiently narrow in momentum space to sample only the bottom of the lowest Bloch band. In this case, the criterion given above is sufficient to avoid inter-band transitions (in the literature this is usually termed "adiabaticity with respect to the band structure").

In actual experiments, the adiabatic criterion we have derived in this Section gives a necessary condition but not a sufficient one. When taking interactions, additional potentials, etc ... into account, the quasi-momentum is no longer a good quantum number and can change during the loading process. Adiabaticity is then determined by energy scales much smaller than the recoil energy, typically the bandwidth J_0 of the lowest Bloch band or even slower time scales determined by the many-body state. We will discuss the role of interactions at length in the next Chapter, but only at zero temperature. Finite temperature effects in interacting lattice gases are currently under a lot of discussion. Thermometry is also not firmly established, and currently involves comparing experimental data to (fairly elaborate) numerical simulations. Finally, the lack of active cooling techniques strongly limits the ability to reach interesting many-body phases. For a review of these issues, we refer the reader to [22].

2.4.2. Time of flight

Assuming that a BEC has been successfully produced in the optical lattice, we now aim to discuss the result of a time-of-flight (t.o.f.) experiment performed by removing suddenly the trapping potential and watching the expansion of the cloud. In appendix A, we remind that (neglecting the effect of interactions during expansion), the wave function

$\psi(\boldsymbol{r},t)$ after a sufficiently long t.o.f. t becomes proportional to the initial wave function $\tilde{\psi}_0$ expressed in momentum space,

$$\psi(\boldsymbol{r},t) \approx \left(\frac{m_a}{\hbar t}\right)^{3/2} \tilde{\psi}_0\left(\boldsymbol{k}=\frac{m_a \boldsymbol{r}}{\hbar t}\right) e^{i\frac{m_a r^2}{2\hbar t}}, \tag{2.55}$$

up to an unimportant global phase. This equation shows that the density of the cloud after expansion[13] is directly proportional to the initial momentum distribution $\mathcal{P}(\boldsymbol{k}) = |\tilde{\psi}_0(\boldsymbol{k})|^2$.

For a cubic lattice, if the system is infinite and uniform, the atoms condense at the energy minimum with band index $\boldsymbol{m} = 0$ and quasi-momentum $\boldsymbol{q} = 0$. Using the three-dimensional generalization of Eq. (2.13) expressing the decomposition of a Bloch wave in the momentum basis, we have

$$\tilde{\phi}_{\mathbf{0},\mathbf{0}}(\boldsymbol{k}) \propto \sum_{\boldsymbol{m}\in\mathbb{Z}^3} \tilde{u}_{\mathbf{0},\mathbf{0}}(\boldsymbol{m})\delta(\boldsymbol{k}-\boldsymbol{Q}_{\boldsymbol{m}}), \tag{2.56}$$

where $\boldsymbol{Q}_{\boldsymbol{m}} = 2k_L\boldsymbol{m}$, and where $\boldsymbol{m}$, a vector with integer components, spans the reciprocal cubic lattice dual to the main one. The momentum distribution of a Bloch state corresponds to a comb structure with Dirac peaks at the positions $\boldsymbol{Q}_{\boldsymbol{m}}$ of the reciprocal lattice, modulated by an envelope $|\tilde{u}_{0,0}(\boldsymbol{m})|^2$. For a finite system, the peaks acquire a finite width but the periodic structure is not affected. We show in Figure 2.14 a typical image which shows an expanding BEC released from a lattice (and falling because of gravity), where the sharp peaks become clearly visible.

Another interpretation arises from writing the Bloch wavefunction in the Wannier basis,

$$\phi_{\mathbf{0},\mathbf{0}}(\boldsymbol{r}) = \frac{1}{\sqrt{N_s}} \sum_{\boldsymbol{R}_i} W(\boldsymbol{r}-\boldsymbol{R}_i), \tag{2.57}$$

$$\tilde{\phi}_{\mathbf{0},\mathbf{0}}(\boldsymbol{p}) \propto \tilde{w}(\boldsymbol{p}) \sum_{\boldsymbol{R}_i} e^{i\frac{\boldsymbol{p}\cdot\boldsymbol{R}_i}{\hbar}}. \tag{2.58}$$

This pattern is exactly analogous to the diffraction pattern obtained by sending a monochromatic wave to a 2D square diffraction grating. One can interpret the images as the interference pattern between matter waves "diffracted" from each lattice site and interfering coherently with each other in the directions corresponding to the reciprocal lattice ($\boldsymbol{p}$ such that $\boldsymbol{p}\cdot\boldsymbol{R}_i = 2\pi\times$integer [13]), in complete analogy with Bragg spots in optics or x-ray diffraction from a solid.

2.4.3. Band mapping

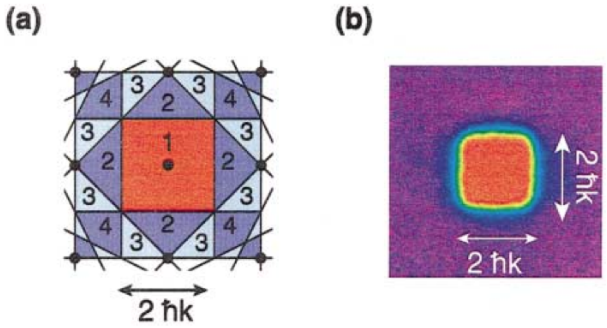

Figure 2.15.: Band mapping of a high temperature Bose gas with $J_0 \ll k_B T \ll \hbar\omega_{\text{lat}}$ [23]. Panel **(a)** shows the different Brillouin zones for the cubic lattice in the imaging plane. Panel **(b)** shows an experimental image for a high temperature gas, with quasi-uniform occupation of the lowest band.

Time-of-flight experiments of the kind described before gives access to the momentum distribution, which is different from the quasi-momentum distribution characteristic of the lattice structure. In particular, the t.o.f. picture does not reveal which energy bands were occupied before releasing the atoms from the lattice. In order to access this information, a different technique is used in experiments, which is basically the reverse of the adiabatic loading technique seen before. Here the lattice depth is ramped down slowly enough that atoms follow adiabatically the lattice band structure, which is "mapped" to the free particle parabola, but fast enough that atoms do not have time to move from their initial

[13] Actual images obtained using absorption techniques are integrated over the direction defined by the probe line-of-sight, *i.e.* they are proportional to $\int dk_z\, |\tilde{\psi}_0(\boldsymbol{k})|^2$.

positions in the time it takes to ramp the lattice down. Figure 2.15 shows such a measurement for a high temperature Bose gas, heated on purpose so that the temperature T is much larger than the width of the lowest band but smaller than the gap to the first excited one, $J_0 \ll k_B T \ll \hbar\omega_{\rm lat}$. In this limit, the occupation of Bloch states in the lowest Bloch band is quasi-uniform, while the populations in excited Bloch bands is small. Increasing the filling further, higher bands would become populated and visible in the second Brillouin zone.

Figure 2.16 shows an example of this procedure applied to a single-component Fermi gas with increasing filling factor. Low filling factors corresponds to populating Bloch states near the minimum $\mathbf{q} = 0$ in the lowest band with one fermion. Many states remain unoccupied, so this corresponds to the analog of a metallic system. Increasing the filling factor, more and more states are populated until $\overline{n} = 1$, where each state in the lowest band is occupied by exactly one fermion (at zero temperature). For such uniform filling, the quasi-momentum distribution is uniform in the first Brillouin zone, and this is experimentally observed. We noted before that adiabatic following becomes problematic near the edges of the Brillouin zone. This is clearly seen from these images, where a substantial rounding of the theoretically sharp edges is observed. Therefore, the band mapping technique must be taken with care for quantitative measurements [24].

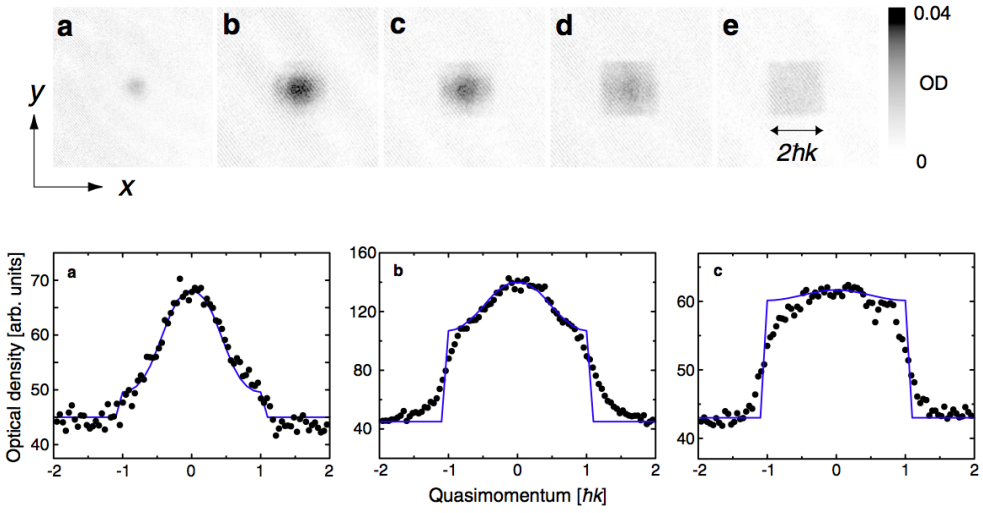

Figure 2.16.: Band mapping of a nearly ideal Fermi gas with increasing filling fraction [25]. The lower panel shows cut through the experimental distributions, together with the one expected for purely adiabatic following. The failure of adiabaticity near the band edges is evident from these plots.

3. Superfluid-Mott insulator transition for bosons

3.1. Bose-Hubbard model

The system we are considering in this chapter is a collection of N spinless identical bosons, trapped in a 3D cubic lattice, and interacting via short-range repulsion. In second-quantized notation, the Hamiltonian governing the properties of this system is

$$\hat{H} = \hat{H}_0 + \hat{H}_{\rm int}, \tag{3.1}$$

$$\hat{H}_0 = \int d\mathbf{r}\ \ \hat{\Psi}^\dagger(\mathbf{r})\Big[-\frac{\hbar^2}{2m_a}\Delta + V_{\rm lat}(\mathbf{r})\Big]\hat{\Psi}(\mathbf{r}), \tag{3.2}$$

$$\hat{H}_{\rm int} = \frac{g}{2}\int d^{(3)}\mathbf{r}\ \hat{\Psi}^\dagger(\mathbf{r})\hat{\Psi}^\dagger(\mathbf{r})\hat{\Psi}(\mathbf{r})\hat{\Psi}(\mathbf{r}). \tag{3.3}$$

Here $\hat{\Psi}(\mathbf{r})$ is the field operator annihilating a boson a position $\mathbf{r}$, $V_{\rm lat}(\mathbf{r})$ is the lattice potential, and $g = 4\pi\hbar^2 a/m_a$ is the coupling constant for $s-$wave collisions described by a scattering length a. $\hat{H}_0$ corresponds to the single-particle part of the many-body Hamiltonian (kinetic plus potential energy) and $\hat{H}_{\rm int}$ to the interaction part.

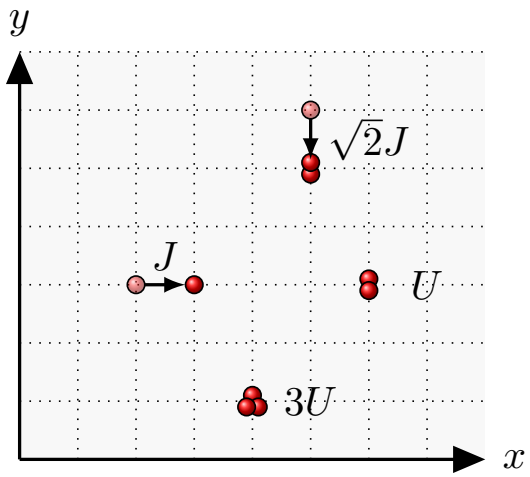

Figure 3.1.: Sketch of a two-dimensional square lattice showing tunneling processes to a neighboring empty site (tunneling energy $-J$) or to a singly-occupied site (tunneling energy $-J\sqrt{2}$), as well as on-site interactions with energy U for doubly-occupied sites and $3U$ for triply-occupied sites.

As such, solving for the eigenstates of this Hamiltonian is impossible (except for very small systems with a few particles), and we need approximations to make progress. We will use the basis of Wannier functions $W_\nu(\boldsymbol{r}-\boldsymbol{r}_i)$, where $\boldsymbol{r}_i$ denotes the position of site i and ν is the band index (recall that both i and ν are triplets of integers for a 3D cubic lattice). Equipped with the basis for the single-particle Hilbert space, we can use the machinery of second quantization to construct a many-particle Fock space spanned by Fock states $\{|n_{\nu,i}\rangle\}$. We denote by $\hat{a}^\dagger_{\nu,i}$ the operator creating a particle in the single-particle state $W_\nu(\boldsymbol{r}-\boldsymbol{r}_i)$, and $n_{\nu,i}$ the occupation number of this state. We can then write the field operator as

$$\hat{\Psi}(\mathbf{r}) = \sum_{\nu,i} W_\nu(\boldsymbol{r}-\boldsymbol{r}_i)\hat{a}_{\nu,i}. \tag{3.4}$$

Inserting this expression into the Hamiltonian (3.1) yields a description which is fully equivalent to the initial one.

Our first approximation to simplify the problem will be the *single-band approximation* : We consider that the populations of all bands but the lowest one to be negligible. As we have seen for the case of an ideal gas, this requires a deeply quantum degenerate gas near unity filling. Keeping only the lowest Bloch band (and dropping the band index

ν to simplify the notations), we obtain the single-band Hamiltonian

$$\hat{H}_{\text{one band}} = -\sum_{i,j} J(|\boldsymbol{r}_i - \boldsymbol{r}_j|)\hat{a}_i^\dagger \hat{a}_j + \sum_{ijkl} \frac{U_{ijkl}}{2} \hat{a}_i^\dagger \hat{a}_j^\dagger \hat{a}_k \hat{a}_l, \tag{3.5}$$

with interaction matrix elements

$$U_{ijkl} \quad = g \int d\mathbf{r}\ W^*(\boldsymbol{r} - \boldsymbol{r}_i) W^*(\boldsymbol{r} - \boldsymbol{r}_j) W(\boldsymbol{r} - \boldsymbol{r}_k) W(\boldsymbol{r} - \boldsymbol{r}_l). \tag{3.6}$$

Our second approximation will be to consider the limit of deep lattices (lattice depth $V_0 \gg E_R$), which allows us to simplify the kinetic terms and the interaction terms in the single-band description. First, the motion of the atoms is well described by the tight-binding approximation and we can neglect all tunneling matrix elements $J(|\boldsymbol{r}_i - \boldsymbol{r}_j|)$ going beyond the nearest neighbors. The notation $\langle i, j\rangle$ indicates a summation on i and j restricted to nearest-neighbors, and we note J the nearest-neighbor tunneling matrix element. Second, the interaction term can be drastically simplified. Noting that Wannier functions are by construction strongly localized around each site i, the most important term in the interactions energy is the one where all site indices coincide, $i = j = k = l$, which we note simply U,

$$U \quad = g \int d\mathbf{r}\ w(\mathbf{r})^4. \tag{3.7}$$

This approximation is discussed in more details in the Appendix D.

Combining the "single-band" and "deep lattice" approximations, one finds a single-band Hamiltonian known as *Bose-Hubbard model* [26, 27],

$$\mathcal{H}_{\text{BH}} = -J \sum_{\langle i,j\rangle} \hat{a}_i^\dagger \hat{a}_j + \frac{U}{2} \sum_i \hat{n}_i \left(\hat{n}_i - 1\right). \tag{3.8}$$

We have noted $\hat{n}_i = \hat{a}_i^\dagger \hat{a}_i$ the operator counting the number of particles at site i.

An analytical expression for the on-site interaction energy can be obtained in the harmonic oscillator approximation, where each lattice well is approximated locally by an harmonic oscillator with frequency $\omega_{\text{lat}} = 2\sqrt{V_0 E_R}$. The Wannier function around that site is then well approximated by the ground state of this harmonic oscillator (see Section 2.2.4). This gives

$$U \quad \approx \sqrt{\tfrac{8}{\pi}} k_L a E_R \left(\tfrac{V_0}{E_R}\right)^{3/4}. \tag{3.9}$$

This formula shows that U increases with lattice depth, but relatively slowly (especially compared to the exponential variation of J with V_0). The on-site interaction energy and tunnel energy (computed numerically from the band structure) are shown in Figure 3.2 for a cubic lattice.

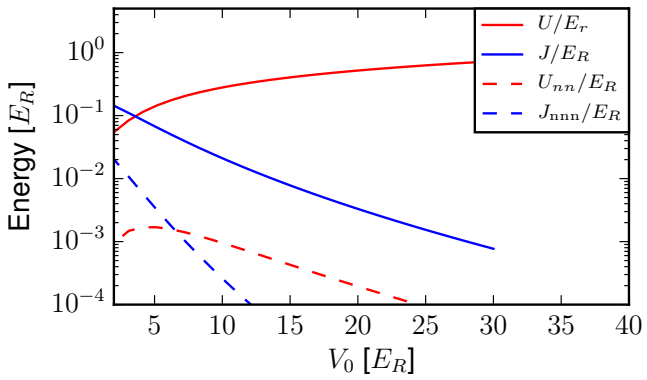

Figure 3.2.: Parameters U, J of the BH model as a function of lattice depth. Energy unit is E_R. The calculation is done using parameters appropriate for ^{87}Rb atoms in a lattice with wavelength $\lambda_L = 850$ nm (approximately the experimental situation in [18]). The next-nearest-neighbor tunneling (nnn) and nearest neighbor interaction are also shown for comparison.

3.2. Ground state of the Bose-Hubbard model

In this Section, we will explore the physics of the ground state of the Bose-Hubbard Hamiltonian, looking first at the extreme limits with $U = 0$ and $J = 0$. The reader can refer to the review articles [28, 17] for an alternative discussion.

3.2.1. Non-interacting condensate, $U = 0$

Fixed atom number N

For a non-interacting gas, we know that the atoms condense in the single-particle state of lowest energy, in our case the lowest Bloch state at $\mathbf{q} = 0$. If there are exactly N atoms in the system, the corresponding many-body state at zero temperature is

$$|\Psi_N\rangle = \frac{1}{\sqrt{N!}} \left(\hat{b}^\dagger_{\mathbf{q}=0}\right)^N |\varnothing\rangle = \frac{1}{\sqrt{N!}} \left(\frac{1}{\sqrt{N_s}} \sum_i \hat{a}^\dagger_i\right)^N |\varnothing\rangle. \tag{3.10}$$

We use the same notation as in the previous chapter:

- $\hat{b}_{\mathbf{q}=0}$ is an annihilation operator for a particle in the lowest energy Bloch state $\mathbf{q} = 0$,
- N_s is the total number of sites,
- $\overline{n} = N/N_s$ is the filling fraction.

We note $\{n_i\}$ a configuration of occupation numbers for which the site i contains n_i particles, and $|\{n_i\}\rangle = \prod_i |n_i\rangle_i$ the corresponding Fock state.

In principle, the many-body state $|\Psi_N\rangle$ is the right choice to describe the experimental situation, where the total atom number N is fixed[1]. This implies that only Fock states $|\{n_i\}\rangle$ with $\sum_i n_i = N$ enter in the decomposition of $|\Psi_N\rangle$. While this does not pose any conceptual problem in the non-interacting case, the constraint $\sum_i n_i = N$ 1) can be tedious for actual calculations even for ideal gases, and 2) further complicates the treatment of the interacting case.

To illustrate the first point, let us take a specific example. We aim to compute the probability $p(n_i)$ to find n_i atoms at one particular site i. Using the multinomial formula[2], one can rewrite Eq. (3.10) as

$$|\Psi_N\rangle = \sum_{\{n_i\}, \sum_i n_i = N} \sqrt{\frac{N!}{N_s^N \prod_i n_i!}} |\{n_i\}\rangle. \tag{3.11}$$

The probability $p(n_i)$ is found by taking the expectation value of the projector $|n_i\rangle_{i\,i}\langle n_i|$ on the subspace spanned by Fock states with exactly n_i particles at site i. This is

$$p(n_i) = |\langle \Psi_N | n_i \rangle_i|^2 = \frac{N!}{N_s^N n_i!} \underbrace{\sum_{\{n_j\}, \sum_j n_j = N - n_i} \frac{1}{\prod_{j\neq i} n_j!}}_{= \frac{1}{(N-n_i)!}(N_s-1)^{N-n_i}} = \underbrace{\frac{N!}{(N-n_i)!}}_{\approx N^{n_i}} \underbrace{\frac{(N_s-1)^{N-n_i}}{N_s^N}}_{\approx e^{-N/N_s}/N_s^{n_i}} \frac{1}{n_i!},$$

where we used the multinomial formula again and Stirling's formula, $N! \approx \sqrt{2\pi N} N^N e^{-N}$, to simplify the factorials. The probability $p(n_i)$ can thus be rewritten as

$$p(n_i) \approx e^{-\overline{n}} \frac{\overline{n}^{n_i}}{n_i!}, \tag{3.12}$$

up to small corrections $\sim 1/N, 1/N_s$ that vanish in the thermodynamic limit $N, N_s \to \infty$. This is a Poisson distribution, with mean value $\overline{n}$ and standard deviation $\sqrt{\overline{n}}$.

From this example, we conclude that calculations with a fixed total number can be done, at least for non-interacting particles, but also that they require a bit of work. It turns out that an alternative description using the so-called *coherent states* $|\Psi\rangle_{\text{coh}}$ allows one to simplify drastically the calculations[3] and the treatment of interactions later on. Provided one calculates properties involving only a few sites, the predictions made using $|\Psi\rangle_{\text{coh}}$ are the same than using the state $|\Psi\rangle_N$ with a fixed number of particles, up to corrections scaling as $1/N, 1/N_s$ that are negligible for large systems. The "price to pay" is that we forfeit the exact conservation of the number of atoms, which holds only on average in the coherent state description.

[1] This statement is a little idealized, since we have discussed already various loss processes (three-body recombination, for instance). They do not change the main point of the discussion provided they are very slow compared to a "typical thermalisation time" (the usual case away from Feshbach resonances). In this situation, it is valid to consider that the system reaches an equilibrium state, and that this equilibrium can adapt to the slowly-decaying atom number in the trap. When the loss processes occur at a rate comparable or greater than the thermalisation time, assuming an equilibrium situation is no longer justified.

[2] $\left(\sum_{i=1}^N a_i\right)^M = \sum_{\{n_i\}_{i=1,\cdots,N}, \sum_i n_i = M} \prod_{i=1}^N \frac{M! a_i^{n_i}}{n_i!}$

[3] This kind of behavior is familiar from statistical quantum mechanics: computing the grand-canonical partition function is much simpler than computing the canonical partition function [29].

Coherent states of the harmonic oscillator :

To set the stage, we first give a brief reminder about how coherent states are introduced in the discussion of the quantum mechanics of a 1d harmonic oscillator [30]. In terms of the ladder operators $\hat{a} = (\hat{x} + i\hat{p})/\sqrt{2}$ and $\hat{a}^\dagger$, the Hamiltonian is $\hat{H} = \hbar\omega(\hat{a}^\dagger\hat{a} + \frac{1}{2})$. Coherent states are defined as

$$|\alpha\rangle = \hat{D}(\alpha)|n = 0\rangle, \tag{3.13}$$

i.e. they result from the action of a *displacement operator*

$$\hat{D}(\alpha) = e^{\alpha\hat{a}^\dagger - \alpha^*\hat{a}} \tag{3.14}$$

on the ground state. Using the Glauber formula[4], we have $\hat{D}(\alpha) = e^{\alpha\hat{a}^\dagger}e^{-\alpha^*\hat{a}}e^{-\frac{1}{2}|\alpha|^2}$ and

$$|\alpha\rangle = e^{-\frac{1}{2}|\alpha|^2}e^{\alpha\hat{a}^\dagger}|n = 0\rangle = e^{-\frac{1}{2}|\alpha|^2}\sum_{n=0}^{+\infty}\frac{\alpha^n}{\sqrt{n!}}|n\rangle. \tag{3.15}$$

Coherent states have several interesting properties :

- **Eigenstates of $\hat{a}$:** They are the eigenstates of the ladder operator $\hat{a}$,

  $$\hat{a}|\alpha\rangle = \alpha|\alpha\rangle. \tag{3.16}$$

  This property simplifies the calculation of expectation values. For instance, the mean number of quanta $\langle\alpha|\hat{n}|\alpha\rangle = \langle\alpha|\hat{a}^\dagger\hat{a}|\alpha\rangle = |\alpha|^2$ can be obtained by letting annihilation operators acting on the right ket and creation operators on the right bra.

- **Poisson distribution :** The probability to find n quanta in a given coherent state is

  $$P(n) = \frac{\langle n\rangle^n e^{-\langle n\rangle}}{n!}, \tag{3.17}$$

  a Poisson distribution of mean $\langle n\rangle = |\alpha|^2$ and variance $\sigma_n^2 = |\alpha|^2$. For large occupations $\langle n\rangle \gg 1$, the Poisson distribution is peaked around $\langle n\rangle$, $P(n) \propto e^{-(n-\langle n\rangle)^2/(2\sigma_n^2)}$.

- **Classical dynamics :** An initial state $|\alpha_0\rangle$ evolves in time as $|\alpha_0 e^{-i\omega t}\rangle$, *i.e.* remains a coherent state with $\alpha(t) = \alpha_0 e^{-i\omega t}$. This implies that $\langle\hat{a}\rangle = \alpha_0 e^{-i\omega t} = (\langle\hat{x}\rangle + i\langle\hat{p}\rangle)/\sqrt{2}$. In the "semi-classical limit" where many oscillator states are occupied ($\langle n\rangle \gg 1$), the uncertainties $\sim\sqrt{\langle n\rangle}$ of x and p are small compared to the mean values $\langle\hat{x}\rangle$ and $\langle\hat{p}\rangle$. In this limit, a coherent state wave packet describes a particle with well-defined (mean) position and momentum, both evolving according to classical mechanics.

Coherent states of a bosonic field :

Coming back to the many-bosons problem, we remark that the Hamiltonian of a free bosonic field is nothing but a collection of independent harmonic oscillators, $\hat{H} = \sum_{\boldsymbol{q}}\varepsilon(\boldsymbol{q})\hat{b}_{\boldsymbol{q}}^\dagger\hat{b}_{\boldsymbol{q}}$. As a result, one can construct coherent states for each mode $\boldsymbol{q}$, as done for instance for the electromagnetic field in quantum optics [30, 31, 32]. For an ideal gas at zero temperature, only the $\boldsymbol{q} = 0$ mode matters and we ignore the others from now on. The various Fock states $|n : \boldsymbol{q} = 0\rangle$ correspond to the eigenstates of the harmonic oscillator. We define a coherent state $N-$body wavefunction with amplitude $\alpha = \sqrt{N}$,

$$|\Psi_{\rm coh}\rangle = e^{-\frac{|\alpha|^2}{2}}e^{\alpha\hat{b}_{\boldsymbol{q}=0}^\dagger}|\varnothing\rangle, \tag{3.18}$$

with the same properties as discussed previously. Using the Wannier expansion $\hat{b}_{\mathbf{q}=0} = \frac{1}{\sqrt{N_s}}\sum_i\hat{a}_i$, and the fact that the operators $\hat{a}_i$ for different sites commute, we have

$$|\Psi_{\rm coh}\rangle = e^{-\frac{N}{2N_s}\times N_s}e^{\sum_i\sqrt{\frac{N}{N_s}}\hat{a}_i^\dagger}|\varnothing\rangle = \prod_i e^{-\frac{N}{2N_s}}e^{\sqrt{n}\hat{a}_i^\dagger}|\varnothing\rangle = \prod_i|\alpha_i = \sqrt{n}\rangle, \tag{3.19}$$

$$|\alpha_i\rangle = e^{-\frac{|\alpha_i|^2}{2}}\sum_{n_i=0}^{\infty}\frac{\alpha_i^{n_i}}{\sqrt{n_i!}}|n_i\rangle_i. \tag{3.20}$$

[4] Glauber formula : $e^{\hat{A}+\hat{B}} = e^{\hat{A}}e^{\hat{B}}e^{-\frac{1}{2}[\hat{A},\hat{B}]}$, a special case of the more general Baker-Campbell-Hausdorff formula valid when $[\hat{A},\hat{B}]$ commutes with both $\hat{A}$ and $\hat{B}$.

This shows that the many-body state can also be expressed as a product over all sites of "'local" coherent states $|\alpha_i\rangle_i$ with amplitudes $\alpha_i = \sqrt{\bar{n}}$, obeying

$$\hat{a}_i|\alpha_i\rangle_i = \alpha_i|\alpha_i\rangle_i. \tag{3.21}$$

As for the simple harmonic oscillator, this property simplifies the calculations of expectation values of normally ordered operators. For instance, $\langle\Psi_{\rm coh}|\hat{a}_j^\dagger\hat{a}_i|\Psi_{\rm coh}\rangle = {}_j\langle\alpha|\hat{a}_j^\dagger\hat{a}_i|\alpha_i\rangle_i = \alpha_j^*\alpha_i$. Note also the non-zero expectation value of the matter wave field,

$$\langle\Psi_{\rm coh}|\hat{a}_i|\Psi_{\rm coh}\rangle = \alpha_i = \sqrt{\bar{n}}, \tag{3.22}$$

which will be discussed further later on.

What is the advantage of introducing $|\Psi_{\rm coh}\rangle$ over the state $|\Psi\rangle_N$ with fixed atom number ? The answer is simplicity and easier calculations. Taking the distribution $p(n_i)$ as an example, we obtain directly the same Poisson distribution found in Eq. (3.12). In the following, we will use $|\Psi_{\rm coh}\rangle$ to describe the state of N condensed bosons. Since the total atom number is no longer fixed but fluctuates by $\sim\sqrt{N}$ around the mean value N, this requires to work in the grand canonical ensemble[5]. The equilibrium state is then obtained by minimizing the free energy

$$\mathcal{G}_{\rm BH} = \mathcal{H}_{\rm BH} - \mu\sum_i \hat{n}_i, \tag{3.23}$$

with μ the chemical potential.

3.2.2. Gross-Pitaevskii theory for weak interactions, $U \ll J$

Let us now consider the case of a weakly-interacting system, where we expect that the Gross-Pitaevskii (GP) theory applies. In essence, the GP theory amounts to postulate an "adiabatic continuity" from the ideal gas to the weakly-interacting case, in the sense that the many-body wavefunction remains close to a product state as in the ideal case. Using the coherent state $|\Psi_{\rm coh}\rangle$ as an *ansatz* for the many-body wavefunction, we obtain the mean free energy as

$$\langle\Psi_{\rm coh}|\mathcal{G}_{\rm BH}|\Psi_{\rm coh}\rangle = -J\sum_{\langle i,j\rangle}\alpha_i^*\alpha_j + \sum_i\frac{U}{2}|\alpha_i|^4 - \mu|\alpha_i|^2. \tag{3.24}$$

As this stage the α_i's are arbitrary. Following the spirit of the GP theory, we use variational calculus, treating α_i, α_i^* as independent variables, to minimize the free energy. Canceling the first derivative of the free energy with respect to α_i^*, we get

$$\mu\alpha_i = -J\sum_{\langle j\rangle_i}\alpha_j + U|\alpha_i|^2\alpha_i, \tag{3.25}$$

where the notation $\langle j\rangle_i$ indicates that the sum runs over all nearest neighbors j of the site i we are interested in. Eq. (3.25) is the discrete analogue on a lattice of the continuum GP equation describing weakly-interacting Bose-Einstein condensates.

The coherent state approach is equivalent to start from this continuum equation and then specialize to the Bose-Hubbard regime by making the tight-binding and single-band approximations. To convince ourselves, we go back to the point of view where the atom number N is fixed. The GP theory then postulates a ground state many-body wavefunction of the form $\Psi_N(\boldsymbol{r}_1,\cdots,\boldsymbol{r}_N) = \prod_{i=1}^N\phi(\boldsymbol{r}_i)$, with ϕ the condensate wavefunction. The energy expectation value is

$$E_N(\phi,\phi^*) = \int d^3\boldsymbol{r}\left(-\frac{\hbar^2}{2M}N\phi^*\Delta\phi + V_{\rm lat}(\boldsymbol{r})N|\phi|^2 + \frac{g}{2}N(N-1)|\phi|^4\right). \tag{3.26}$$

Minimization of the energy E_N with respect to ϕ under the normalization constraint $\langle\phi|\phi\rangle = 1$ gives the GP equation

$$\mu\phi = -\frac{\hbar^2}{2M}\Delta\phi + V_{\rm lat}\phi + g(N-1)|\phi|^2\phi. \tag{3.27}$$

Assuming that the condensate only occupies the lowest band of the lattice, we expand ϕ in the Wannier basis, $\phi(\boldsymbol{r}) = (1/\sqrt{N_s})\sum_{\nu,i}W_i(\boldsymbol{r})\tilde{\alpha}_i$, with $\sum_{\nu,i}|\tilde{\alpha}_i|^2 = N_s$ to ensure the normalisation of ϕ. We insert this expansion in the GP equation, multiply by $W_i(\boldsymbol{r})^*$ and integrate over space. This gives

$$\frac{\mu\tilde{\alpha}_i}{\sqrt{N_s}} = -\sum_{i,j}\underbrace{\left(\int d\boldsymbol{r}\,W_i^*(\boldsymbol{r})\left[\frac{\hbar^2}{2M}\Delta\psi - V_{\rm lat}(\boldsymbol{r})\right]W_j(\boldsymbol{r})\right)}_{=J(|\boldsymbol{r}_i-\boldsymbol{r}_j|)}\frac{\tilde{\alpha}_j}{\sqrt{N_s}} + \sum_{j,k,l}\underbrace{\left(g\int d\boldsymbol{r}\,W_i^*(\boldsymbol{r})W_j^*(\boldsymbol{r})W_k(\boldsymbol{r})W_l(\boldsymbol{r})\right)}_{=U_{ijkl}}\frac{N-1}{N_s^{3/2}}\tilde{\alpha}_j^*\tilde{\alpha}_k\tilde{\alpha}_l$$

[5] This should not be interpreted as a statement that the number of particles fluctuate in actual experiments. Rather, the statement is that one can calculate the equilibrium properties *as if* the system was in contact with a particle reservoir. The results will be the same as for a fixed number of particles up to corrections $\sim 1/N, 1/N_s$.

Making the same assumptions entering in the derivation of the BH model and letting $\alpha_i = \sqrt{N/N_s}\tilde{\alpha}_i$, we indeed recover the discrete GP equation Eq. (3.25).

Long-wavelength limit :

The family of coherent states with amplitudes α_i that vary slowly with the site index i provides not only the (approximate) ground state, but also (equally approximate) low-energy excited states. Because the amplitudes are assumed to vary slowly in space, one can perform a continuum approximation where α_i is taken as the limit of a continuous field $\Psi(x)$ evaluated at each lattice site x_i. The continuum limit corresponds to

$$\sum_i \cdots \longrightarrow \frac{1}{d^3}\int d\boldsymbol{r}\cdots, \qquad \alpha_i \longrightarrow \Psi(\boldsymbol{r}_i) = \frac{\alpha_i}{d^{3/2}}, \qquad \sum_i |\alpha_i|^2 \longrightarrow \int d\boldsymbol{r}\,|\Psi(\boldsymbol{r})|^2\cdots$$

Note the step ensuring the normalization of the wavefunction Ψ. The mean-energy in the state $|\Psi_{\rm coh}\rangle$ is given by Eq. (3.24). In the continuum limit, one can approximate the discrete differences in Eq. (3.24) by derivatives of the continuous field Ψ. Writing $\boldsymbol{r}_i$ and $\boldsymbol{r}_j = \boldsymbol{r}_i \pm d\boldsymbol{e}_\alpha$ the locations of two neighboring sites ($\alpha = x, y, z$),

$$\alpha_j \approx d^{3/2}\Psi(\boldsymbol{r}_i \pm d\boldsymbol{e}_\alpha) \approx d^{3/2}\left(\Psi(\boldsymbol{r}_i) \pm \left.\frac{\partial\Psi}{\partial x_\alpha}\right|_{\boldsymbol{r}_i} d + \frac{1}{2}\left.\frac{\partial^2\Psi}{\partial x_\alpha^2}\right|_{\boldsymbol{r}_i} d^2 + \cdots\right). \tag{3.28}$$

Performing the substitution in Eq. (3.24), one finds

$$E_{\rm GP}[\Psi^*,\Psi] = \int d\boldsymbol{r}\left(-Jd^2\Psi^*\Delta\Psi + \frac{Ud^3}{2}|\Psi|^4 - (\mu + zJ)|\Psi|^2\right), \tag{3.29}$$

and z is the number of nearest neighbors ($z = 6$ for a cubic 3d lattice). The functional form of $E_{\rm GP}$ is identical to the continuum GP energy functional in Eq. (3.26), and it may seem at first sight that we have come back to our starting point. This is not the case, because the coefficients entering in $E_{\rm GP}$ are *effective* parameters valid only for low-energy configurations. The coefficient in front of the kinetic energy term is $Jd^2 = \frac{\hbar^2}{2m*}$, with m^* the effective mass, and the coefficient in front of the interaction term is $g^* = Ud^3 = gd^3\int d\boldsymbol{r}\,|W(\boldsymbol{r})|^4 \geq g$. This is an example of renormalization at work : the low-energy behavior of a many-body system is determined by an effective (classical in this case) field theory with the same functional form as the original microscopic theory, but with renormalized parameters $m \to m^*$ and $g \to g^*$.

It is intesting to rework the criterion for strong correlations discussed in the introduction. Using the effective low-energy parameters, the ratio between kinetic and potential energies is given by

$$\frac{E_{\rm kin}}{E_{\rm int}} \sim \frac{\frac{\hbar^2 n^{2/3}}{2m^*}}{g^* n} \sim \frac{U\overline{n}^{1/3}}{J}. \tag{3.30}$$

We recover the results announced in the introduction : even if one starts with a gas which would be in the weakly-interacting regime ($E_{\rm kin} \ll E_{\rm int}$), transferring it to a deep lattice where $U \gg J$ allows one to enter a strongly-correlated regime. In this regime, neither the coherent state ansatz nor the GP theory are appropriate, and this gives a condition of validity for the coherent state approach as $U\overline{n}^{1/3} \ll J$.

Spontaneous gauge symmetry breaking :

We come back to the fact that the matter field $\hat{a}_i$ acquires a non-zero expectation value in a coherent state,

$$\langle\Psi_{\rm coh}|\hat{a}_i|\Psi_{\rm coh}\rangle = \alpha_i = \sqrt{\overline{n}}e^{i\theta},$$

where the *global* phase θ is arbitrary. This is an example of a *spontaneous symmetry breaking*, a concept prevalent in quantum field theory, high-energy and many-body physics. The underlying Hamiltonian obeys a so-called gauge symmetry, *i.e.* is left invariant by a gauge transformation $\hat{\Psi} \to e^{i\theta}\hat{\Psi}$. However in the coherent state description the ground state does not obey this symmetry which transforms one coherent state into another. In principle, breaking the gauge symmetry is forbidden by a *superselection rule* that states that the particle number $\hat{N}$ is an exactly conserved quantity. By using a coherent state description, we chose to violate this selection rule but "not too much": The mean atom number remains the same, $\langle\hat{N}\rangle = N$, and fluctuations around the mean $\Delta N = \sqrt{N}$ are small for $N \gg 1$. In the thermodynamic limit where $N, N_s \to \infty$, the selection rule is restored and the predictions made assuming spontaneous symmetry breaking or not are identical.

The physical reality behind a statement like $\langle\Psi_{\rm coh}|\hat{a}_i|\Psi_{\rm coh}\rangle \neq 0$ is that of *off-diagonal long-range order*, originally introduced by Penrose and Onsager in the context of liquid helium [33, 2]. Penrose and Onsager considered a bosonic

system and argued that the presence of a condensate was manifest in the long-distance behavior of the single-particle density matrix,

$$\langle \hat{\Psi}^\dagger(\boldsymbol{r})\hat{\Psi}(\boldsymbol{r}')\rangle \xrightarrow[|\boldsymbol{r}-\boldsymbol{r}'|\to\infty]{} N_c \Phi^*(\boldsymbol{r})\Phi(\boldsymbol{r}').$$

Here $\Phi(\boldsymbol{r})$ is formally defined as the eigenvector of $\langle \hat{\Psi}^\dagger(\boldsymbol{r})\hat{\Psi}(\boldsymbol{r}')\rangle$ with the largest eigenvalue N_c, which must be macroscopic ($\sim N$) to speak of Bose-Einstein condensation. Note that $N_c \leq N$, the equality being fulfilled only for an ideal gas. The discrete version for a lattice system is

$$\langle \hat{a}_i^\dagger \hat{a}_j\rangle \xrightarrow[|\boldsymbol{r}_i-\boldsymbol{r}_j|\to\infty]{} \alpha_i^* \alpha_j.$$

If the system is indeed in a coherent state, *then* the Penrose-Onsager criterion is fulfilled. However the converse is not true, and it is certainly possible to build states with fixed atom number also obeying the Penrose-Onsager criterion (for instance, $|\Psi\rangle_N$). Coherent states and spontaneous symmetry breaking are convenient tools to use in the theory, but one should be careful not to push the interpretation of quantities like $\langle \hat{a}_i\rangle$ too far. The reader can consult refs. [34, 35, 2] for a further discussion.

3.2.3. Strongly interacting gas, $U/J \to \infty$

We look next at the strongly interacting $U/J \to \infty$. This is equivalent to taking the limit of a disconnected lattice ($J = 0$), where the lattice sites are independent from each other. The Hamiltonian reduces to the interacting part of the Bose-Hubbard model, and the free energy to

$$\mathcal{G}_{J=0} = \sum_i \frac{U}{2}\hat{n}_i\left(\hat{n}_i - 1\right) - \mu\hat{n}_i = \sum_i \mathcal{G}_i. \tag{3.31}$$

Since all sites have the same occupation number, we are left with a single-well problem. We remark that $\mathcal{G}_i$ is diagonal in the Fock basis, for commensurate fillings $\overline{n} = n_0$ ($n_0 \in \mathbb{N}$). The ground state wave function is then given by a product over all sites of identical Fock states,

$$|\Psi_{\text{Fock}}\rangle = \prod_i |n_0\rangle_i. \tag{3.32}$$

Here n_0 is the (integer) number of atoms per well that minimizes $\mathcal{G}_i$. We plot $\mathcal{G}_i$ as a function of μ in Figure 3.3 for $n_0 = 0, 1, 2, 3$. The configuration with minimal free energy is achieved for $n_0 = \overline{n} = \text{int}(\mu/U) + 1$, where int denotes the integer part. The Fock state in Eq. (3.32) strongly differs from the condensed state found for weak interactions. The density is pinned at integer values with zero fluctuations, at variance with the Poisson distribution found for $U = 0$. This type of state of matter is called a *Mott insulator*, to contrast with bosonic states with non-zero condensed fraction that are able to carry superfluid currents. As we shall see later in details, most physical observables have a completely different behavior in a superfluid/condensed state and in a Mott insulator.

The case where the filling is not commensurate with the lattice ($\overline{n}$ is not an integer) corresponds to $\mu/U = p$ with p integer. In this case, the on-site Fock states with p and $p+1$ atoms are degenerate, and the on-site wave function can be any superposition of the two. The ground state is then of the form

$$|\Psi_N\rangle = \prod_i \left(\cos\left(\frac{\theta}{2}\right)|p\rangle_i + \sin\left(\frac{\theta}{2}\right)e^{i\phi}|p+1\rangle_i\right), \tag{3.33}$$

with $\overline{n} = p + \sin^2(\theta/2)$. All states with filling factor $\in]p, p+1[$ are degenerate in the limit $J = 0$, however the degeneracy is immediately lifted as soon as $J \neq 0$. This will be treated in a later Section.

3.2.4. Gutzwiller ansatz for the ground state in a cubic lattice

For arbitrary U/J, there is no longer a simple and exact solution for the ground state of the Bose-Hubbard model. One possibility to understand the physics at work in experiments is to perform Monte-Carlo simulations, which work well for bosons and have become very powerful tools in recent years (see [36] for a recent review). Another strategy is to use to approximate methods, which will hopefully capture most of the underlying physics while staying relatively simple.

We follow here the latter strategy, using an approximate variational method proposed by several authors following the work of Gutzwiller for the equivalent fermionic model [37, 38, 39]. The method postulates a many-body wave function Ψ which factorizes as a product of on-site wave functions ϕ_i at each site i,

$$|\Psi\rangle_{\text{Gutzwiller}} = \prod_{\text{sites } i} |\phi_i\rangle, \tag{3.34}$$

$$|\phi_i\rangle = \sum_{n_i=0}^{\infty} c(n_i)|n_i\rangle_i. \tag{3.35}$$

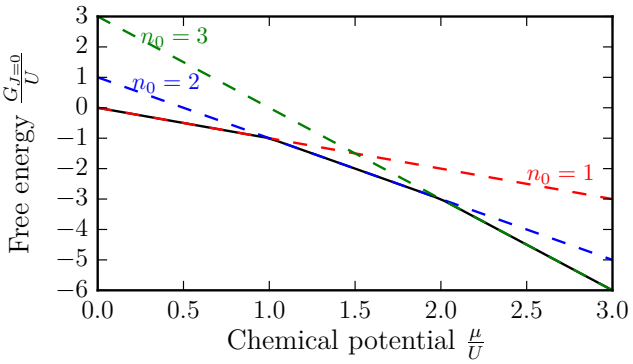

Figure 3.3.: On-site free energies as a function of μ for $\overline{n} = 0, 1, 2, 3$ in the atomic limit ($J = 0$).

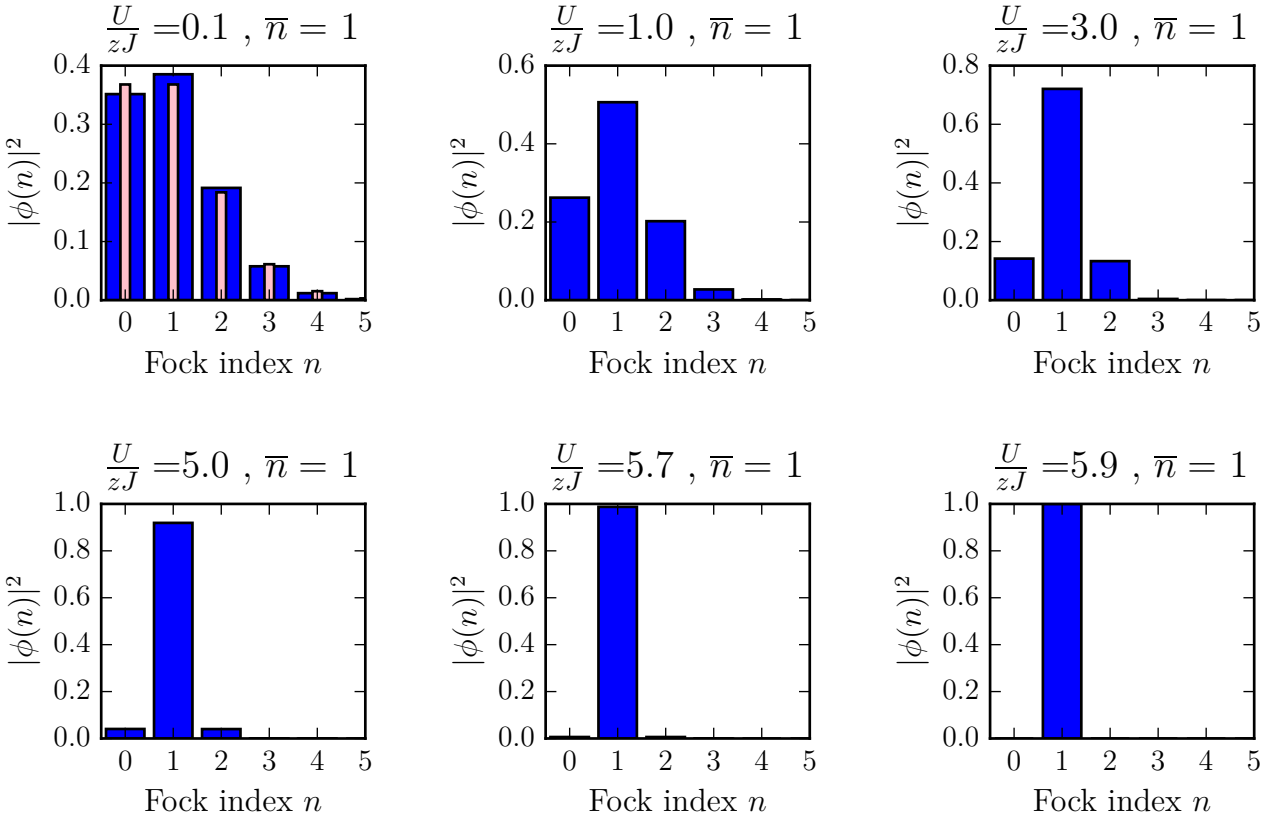

Figure 3.4.: Ground state of the Bose-Hubbard model for $\overline{n} = 1$ in the Gutzwiller approximation. The gray bars in the plot for $U = 0.1\, zJ$ show the Poisson distribution with mean $\overline{n} = 1$.

This trial wave function is exact in the two limits $J \to 0$ ($|\phi_i\rangle$ is a Fock state) and $U \to 0$ ($|\phi_i\rangle$ is a coherent state), so that one can expect this is a reasonable approximation in between. One then calculates the free energy corresponding to the Gutwziller trial wave function and minimizes it with respect to the coefficients $c(n_i)$ to obtain the best variational estimate of the ground state, under the constraint $\langle n \rangle = \sum_{n=0}^{\infty} |c(n)|^2 n = \overline{n}$. Using the ansatz Eq. (3.34), the average free energy is given by

$$\langle \mathcal{G}_{\mathrm{BH}} \rangle_{\mathrm{Gutzwiller}} = -J \sum_{\langle i,j \rangle} \alpha_i^* \alpha_j + \sum_i \sum_{n_i=0}^{\infty} \left[\frac{U}{2} n_i(n_i - 1) - \mu n_i \right] |c(n_i)|^2. \tag{3.36}$$

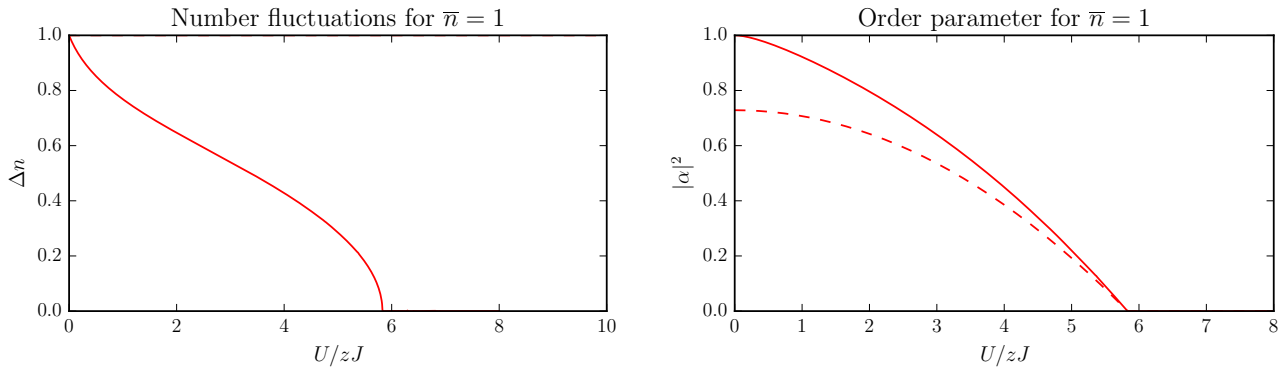

Figure 3.5.: Density fluctuations $\Delta n = \langle \hat{n}_i^2 \rangle - \langle \hat{n}_i \rangle^2$ (left panel) and order parameter $|\alpha|^2$ (right panel) for unity filling $\overline{n} = 1$. The solid line is a numerical result, the dashed line the prediction of the particle-hole approximation.

One can evaluate the average density and density fluctuations,

$$\langle \hat{n}_i \rangle = \sum_{n_i=0}^{\infty} n_i |c(n_i)|^2, \qquad \langle \hat{n}_i^2 \rangle - \langle \hat{n}_i \rangle^2 = \sum_{n_i=0}^{\infty} \left(n_i - \langle \hat{n}_i \rangle \right)^2 |c(n_i)|^2, \tag{3.37}$$

and the expectation value of the matter wave field at each site,

$$\alpha_i = \langle \phi_i | \hat{a}_i | \phi_i \rangle = \sum_{n_i=0}^{\infty} \sqrt{n_i + 1} c^*(n_i) c(n_i + 1). \tag{3.38}$$

The superfluid phase is characterized, as for the non-interacting case, by $\alpha_i \neq 0$.

For a uniform system, all sites are equivalent and one has the simpler equation

$$\langle \mathcal{G}_{\mathrm{BH}} \rangle_{\mathrm{Gutzwiller}} / N_s = -zJ|\alpha|^2 + \frac{U}{2} \langle n^2 \rangle - \left(\mu + \frac{U}{2} \right) \langle n \rangle. \tag{3.39}$$

In general, one has to do the minimization numerically to find the coefficients $c(n_i)$. The result is shown in Figure 3.4 for $\overline{n} = 1$, where the Fock basis has been truncated to $n \leq 10$ to perform the minimization. For weak interactions, the number distribution $p(n_i)$ shown in Figure 3.4 is close to a Poisson distribution expected for a coherent state, shown as thin gray bars for $U \approx 0.1\, zJ$. As interactions increase, $p(n_i)$ deviates strongly from the Poisson distribution. The repulsion between the bosons narrows down the distribution of occupation numbers which becomes more and more concentrated around $n_i = \overline{n}$ (a phenomenon known as "number squeezing" due to the strong decrease of the variance with increasing U, see Fig. 3.5). For large interactions, only one Fock state is populated, as in Eq. (3.32).

Condensate fraction :

For the uniform case we are considering, Bose-Einstein condensation always occur in the single-particle state with quasi-momentum $\boldsymbol{q} = 0$. The condensate fraction f_c is defined as the normalized population of the quasi-momentum state $\boldsymbol{q} = 0$,

$$f_c = \frac{1}{N} \langle \hat{b}_{\boldsymbol{q}=0}^{\dagger} \hat{b}_{\boldsymbol{q}=0} \rangle = \frac{1}{N N_s} \sum_{i,j} \langle \hat{a}_i^{\dagger} \hat{a}_j \rangle. \tag{3.40}$$

For the Gutzwiller trial wavefunction, one has $\langle \hat{a}_i^{\dagger} \hat{a}_i \rangle = \overline{n}$ and $\langle \hat{a}_i^{\dagger} \hat{a}_j \rangle = \alpha_i^* \alpha_j = |\alpha|^2$ for $i \neq j$, where the order parameter α_i is defined in Eq. (3.38). The condensed fraction is then given by

$$f_c = \frac{1}{N N_s} \sum_i \langle \hat{a}_i^{\dagger} \hat{a}_i \rangle + \frac{1}{N N_s} \sum_{i \neq j} \langle \hat{a}_i^{\dagger} \hat{a}_j \rangle, \tag{3.41}$$

$$= \frac{\overline{n}}{N} + \frac{N_s - 1}{N} |\alpha|^2 = \frac{1}{N_s} + \frac{|\alpha|^2}{\overline{n}} \left(1 - \frac{1}{N_s} \right) \underset{N_s, N \to \infty}{\longrightarrow} \frac{|\alpha|^2}{\overline{n}} \tag{3.42}$$

We recover that for the non-interacting/Gross-Pitaevskii case with $\alpha = \sqrt{\overline{n}}$, the condensed fraction is $f_c = 1$, as it should be for an ideal gas at $T = 0$. Conversely, for an array of Fock states with n_0 atoms per site, one has $\alpha = 0$, and the condensed fraction $f_c = n_0 N_s / N N_s = 1/N_s$ goes to zero in the thermodynamic limit $N, N_s \to 0$.

In the general case described by the Gutzwiller trial wavefunction, the condensed fraction is determined by the expectation value of the matter wave field α. The global phase (uniform in the ground state) is irrelevant, and the modulus $|\alpha|$ can be taken as the *order parameter* characterizing the superfluid phase[6].

In Figure 3.5, we show how the order parameter and the number fluctuations evolve with increasing U/J. We find that they both vanish at a specific value of the interaction strength and above. This behavior signals a *quantum phase transition* (at zero temperature) between a condensed state with macroscopic occupation of the $\mathbf{q} = 0$ mode to a Mott insulator state. This transition only occurs for integer filling $\overline{n}$, since the particle number must be commensurate with the number of sites to accommodate a Mott state (3.32).

Mean-field formulation:

The Gutzwiller variational approach is equivalent to a mean-field theory, first formulated in [39], where the variational free energy is seen as the expectation value of an effective single-site Hamiltonian, $H_{\text{eff}} = \sum_i \hat{h}_i^{(\text{eff})}$ with

$$\hat{h}_i^{(\text{eff})} = -zJ\left(\gamma \hat{a}_i^\dagger + \gamma^* \hat{a}_i - |\alpha|^2\right) + \frac{U}{2}\hat{n}_i^2 - \left(\mu + \frac{U}{2}\right)\hat{n}_i. \tag{3.43}$$

The quantity $\gamma = (1/z)\sum_{j\,\text{nn}} \alpha_j$ can be interpreted as a "mean atomic field" from all nearest neighbors seen by the ith site. The advantage of the mean field formulation is that it can also be used to compute the excitation spectrum [39, 42, 43].

3.2.5. Particle-hole approximation

Analytical results can be obtained using a simplified version of the Gutzwiller wave function, where one truncates the on-site Fock basis to just three states [44],

$$|\phi_i\rangle = c(n_0 - 1)|n_i = n_0 - 1\rangle_i + c(n_0)|n_i = n_0\rangle_i + c(n_0 + 1)|n_i = n_0 + 1\rangle_i, \tag{3.44}$$

with n_0 the integer closest to the average filling fraction $\overline{n}$ and the nearest integers. This wave function will certainly not be valid for $U \ll zJ$, but is reasonable in the regime where interactions become strong enough (see Figure 3.4). We will call it the "particle-hole" approximation for reasons that will be apparent later on. Taking the normalization of $|\phi_i\rangle$ into account, the coefficients can be parametrized as

$$c(n_0 - 1) = \cos(\chi)\sin(\theta)\, e^{i\phi_-}, \tag{3.45}$$

$$c(n_0) = \cos(\theta), \tag{3.46}$$

$$c(n_0 + 1) = \sin(\chi)\sin(\theta)\, e^{i\phi_+}, \tag{3.47}$$

where $\theta, \chi \in [0, \pi/2]$ and $\phi_\pm \in [0, 2\pi]$. The average filling is given by

$$\overline{n} = n_0 - \sin^2(\theta)\cos(2\chi). \tag{3.48}$$

For $\chi = \pi/4$, the atomic filling is thus commensurate with the lattice with n_0 atoms per site on average.

Commensurate filling $\overline{n} = n_0$

We focus first on the commensurate case where $\overline{n} = n_0$ (or equivalently $\chi = \pi/4$). Computing the variational energy gives

$$\frac{\langle \mathcal{G}_{\text{BH}}\rangle_{\text{Gutzwiller}}}{N_s} = \mathcal{G}_{J=0} + \frac{U}{2}\sin^2(\theta) - \frac{zJ}{4}\sin^2(2\theta)\left(2n_0 + 1 + 2\sqrt{n_0(n_0+1)}\cos(\phi_+ - \phi_-)\right), \tag{3.49}$$

where $z = 6$ is the number of nearest neighbors. Minimizing with respect to the phases $\phi_\pm$ yields immediately $\cos(\phi_+ - \phi_-) = 1$ (this is true as well for arbitrary filling fractions). Taking this into account, the free energy simplifies to

$$\frac{\langle \mathcal{G}_{\text{BH}}\rangle_{\text{Gutzwiller}}}{N_s} = \mathcal{G}_{J=0} + \frac{U}{2}\sin^2(\theta) - \frac{zJ}{4}A(n_0)\sin^2(2\theta). \tag{3.50}$$

[6] There is a subtle distinction between the condensate fraction and the superfluid fraction, which are related but in general not equal to each other. We will not explicitely calculate the superfluid fraction in these notes, and always refer to the condensate fraction to characterize the superfluid phase (see [40] for a general discussion, and [41] for the specific case of the Bose-Hubbard model).

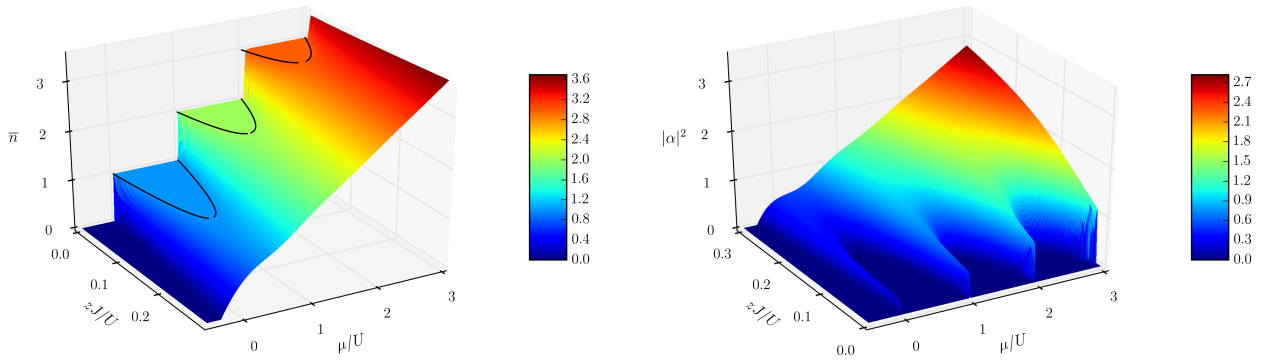

Figure 3.6.: Phase diagram of the Bose-Hubbard model in the $J-\mu$ plane at zero temperature. The left panel shows the filling factor and the right panel the order parameter $|\alpha|^2$ versus tunneling J and chemical potential μ. Note the zJ/U axis of the two plots are reversed to make the interesting parts more visible.

where the coefficient $A(n_0) = (\sqrt{n_0} + \sqrt{n_0+1})^2$. The variational free energy is minimized with respect to θ when

$$(1) \quad \cos(2\theta) = \frac{U}{zJA(n_0)} \quad \text{or} \quad (2) \quad \sin(2\theta) = 0.$$

The first solution exists if the ratio U/zJ is lower than a critical value,

$$U \leq U_c = zJA(n_0) = zJ\left(2n_0 + 1 + 2\sqrt{n_0(n_0+1)}\right). \tag{3.51}$$

and it has the lowest free energy. This solution corresponds to a superfluid state, with an order parameter

$$\alpha = \langle \hat{a}_i \rangle = \begin{cases} \sqrt{\frac{A(n_0)}{2}\left[1 - \left(\frac{U}{U_c}\right)^2\right]} & \text{if} \quad U \leq U_c, \\ 0 & \text{if} \quad U \geq U_c, \end{cases} \tag{3.52}$$

with a condensate fraction $f_c = |\alpha|^2/n_0$. When U becomes larger than the critical value U_c, only the second solution is possible, with free energy $\mathcal{G}_{J=0}$; This is nothing but the Mott insulator state for $J = 0$ given earlier in Eq. (3.32). The boundaries between the two phases are $(U/zJ)_c \approx 5.8$ for $\overline{n} = 1$ and $(U/zJ)_c \approx 9.9$ for $\overline{n} = 2$ (see Figure 3.2).

3.2.6. Phase diagram

In the generic case where $\overline{n}$ is not integer, one cannot "fill" the lattice uniformly with an integer number of atoms per site. The extra (or missing) atoms will be mobile, and generally form a superfluid phase. For $J \to 0$, this superfluid phase connects to the degeneracy points where the chemical potential μ/u is integer (see Section 3.2.3). At these points, the Fock states with $n_0 - 1$ atoms and n_0 atoms are degenerate, where $n_0 - 1$ is the integer part of $\overline{n}$, and all densities intermediate between n_0 and $n_0 - 1$ are possible. A weak tunneling lifts this degeneracy and allows the superfluid phase to exist for a broader range of chemical potentials. Using the same variational equations as before with the additional parameter χ, one finds superfluid-type solutions (i.e. $\theta \neq 0$) only for a certain interval of chemical potentials,

$$\mu_{n_0}^{(+)} \leq \mu \leq \mu_{n_0+1}^{(-)}. \tag{3.53}$$

Here $\mu_{n_0}^{(+)}$ (resp. $\mu_{n_0+1}^{(-)}$) are the upper (resp. lower) boundary of the Mott region with occupation number n_0 (resp. $n_0 + 1$). As the chemical potential is varied from the upper n_0 boundary to the lower $n_0 + 1$ boundary , the density interpolates continuously from n_0 to $n_0 + 1$.

A simple method to determine the boundaries of the Mott phase is to consider the effective single-site Hamiltonian given in Eq. (3.43). The leading term is the on-site free energy $\mathcal{G}_i$ in Eq. 3.31. The unperturbed ground state is the Fock state $|n_0\rangle_i$ with n_0 atoms per site. One treats the tunneling term as a perturbation, and looks when the perturbation is sufficiently strong to destabilize the Fock state. The first-order perturbed ground state is given to by

$$|\phi_i\rangle_{\text{pert}} = |n_0\rangle_i + \frac{zJ\alpha\sqrt{n_0}}{\mu - U(n_0-1)}|n_0 - 1\rangle_i + \frac{zJ\alpha\sqrt{n_0+1}}{Un_0 - \mu}|n_0+1\rangle_i. \tag{3.54}$$

The on-site matter wave field $\alpha = \langle \phi_i | \hat{a}_i | \phi_i \rangle$ is determined by the self-consistency condition,

$$\alpha = zJ\alpha \left(\frac{n_0}{\mu - U(n_0 - 1)} + \frac{n_0 + 1}{Un_0 - \mu} \right). \tag{3.55}$$

One possible solution is $\alpha = 0$ (the Mott phase). The other solution corresponds to the superfluid phase, and exists if the equation

$$\frac{U}{zJ} = \frac{n_0}{\mu - U(n_0 - 1)} + \frac{n_0 + 1}{Un_0 - \mu} \tag{3.56}$$

admits a real solution for μ. The roots of this quadratic equation are

$$\mu_{n_0}^{(\pm)} = U \left(n_0 - \frac{1}{2} \right) \pm \frac{zJ}{2} \pm \sqrt{U^2 - 2UzJ(2n_0 + 1) + (zJ)^2}. \tag{3.57}$$

For chemical potentials inside the interval $\mu_{n_0}^{(-)}, \mu_{n_0}^{(+)}]$, the system prefers to form a Mott insulator state (the ground state remains a Fock state in our mean-field model). As soon as μ is outside this interval, there is another solution with $\alpha \neq 0$ which is thermodynamically more favourable. A superfluid component then develops. The resulting phase diagram in the $J - \mu$ plane [26, 45] is shown in Figure 3.6, featuring a serie of Mott "lobes" for $U \geq U_c(n_0)$. For $U < U_c(n_0 = 1)$, the width of the largest Mott lobe ($n_0 = 1$)goes to zero and only a superfluid phase remains.

The strongly interacting superfluid phase that lies between Mott regions is quite different from the "usual" condensate found for weak interactions. The condensate fraction is substantially lower than unity, as in superfluid ^{4}He. In fact, using a variational wave function that only retains the n_0 and $n_0 + 1$ components, one finds a condensate fraction

$$f_c = \frac{n_0 + 1}{\overline{n}} (\overline{n} - n_0)(n_0 + 1 - \overline{n}). \tag{3.58}$$

It goes to zero at the Mott boundaries, as expected, and takes a maximum value $(n_0 + 1)/2(2n_0 + 1)$ when the density $\overline{n} = n_0 + 1/2$: This is only $1/2$ for $n_0 = 0$ and $\to 1/4$ for large filling $\overline{n} \gg 1$. The quantum depletion of the condensate in the superfluid layers is therefore rather strong, and standard methods for weakly interacting gases (Gross-Pitaevskii or Bogoliubov theories) are not expected to be good descriptions in this strongly interacting regime.

3.3. Interference experiments

3.3.1. Phase coherence

We now revisit time-of-flight experiments, as discussed in Section 2.4.2 for non-interacting gases, in the light of the discussion about interacting systems. The wave function of a particle released from the lattice can be written in the Wannier basis as

$$\hat{\psi}(\mathbf{r}, t) = \sum_i W(\mathbf{r} - \mathbf{r}_i, t) \hat{b}_i = \left(\frac{m_a}{\hbar t} \right)^{3/2} \tilde{W} \left(\mathbf{k} = \frac{m_a \mathbf{r}}{\hbar t} \right) \sum_i e^{i \frac{m_a \mathbf{r} \cdot \mathbf{r}_i}{\hbar t}} \hat{b}_i. \tag{3.59}$$

Assuming interactions do not perturb the expansion significantly, which is typically a good approximation [46], the atomic density for long time of flights, $n_{\text{tof}}(\mathbf{K}) = \langle \hat{\psi}^\dagger(\mathbf{r}, t) \hat{\psi}(\mathbf{r}, t) \rangle$, is determined as the product of two factors,

$$\langle n_{\text{tof}}(\mathbf{K}) \rangle \approx \mathcal{G}(\mathbf{K}) \, \mathcal{S}(\mathbf{K}). \tag{3.60}$$

Here $\mathbf{K} = \frac{m_a \mathbf{r}}{\hbar t}$ is a rescaled position and $\mathcal{G}(\mathbf{K}) = \left(\frac{m_a}{\hbar t} \right)^3 |\tilde{W}(\mathbf{K})|^2$ is a smooth enveloppe function. The *structure factor*

$$\mathcal{S}(\mathbf{K}) = \sum_{i,j} e^{i\mathbf{K} \cdot (\mathbf{r}_j - \mathbf{r}_i)} \langle \hat{b}_i^\dagger b_j \rangle. \tag{3.61}$$

determines the fine structure of the interference pattern, and is the Fourier transform of the first-order correlation function

$$\mathcal{C}(i, j) = \langle \hat{b}_i^\dagger b_j \rangle \tag{3.62}$$

quantifying the spatial range over which phase coherence is established. For a BEC in a coherent state, one simply finds

$$\mathcal{C}_{\text{BEC}}(i, j) = \sqrt{\overline{n}_i \overline{n}_j}, \tag{3.63}$$

i.e. phase coherence extends over the whole lattice. As seen before, this gives rise to sharp peaks in the distribution pattern,

$$\mathcal{S}_{\mathrm{SF}}\left(\mathbf{K}\right) \approx \left| \sum_i e^{i\mathbf{K}\cdot\mathbf{r}_i} \sqrt{\overline{n_i}} \right|^2 , \tag{3.64}$$

which we interpreted as the signature of the lattice band structure. Eq. (3.64) suggests another interpretation in terms of interfering matter waves: The density distribution results from the coherent superposition of many matter waves "emitted" coherently from each lattice sites and propagating in free space. The interference peaks results from the coherent superposition of all these waves along well-defined directions corresponding to vectors of the reciprocal lattice, exactly as for Bragg diffraction of x-rays on solids. The interference peaks are often termed "Bragg peaks" to stress the analogy.

Phase coherence is progressively lost as U/J increases from zero and the condensate is depleted. In the Mott insulator state (3.32), phase coherence vanishes completely,

$$\mathcal{C}_{\mathrm{Mott}}(i,j) = n_0 \delta_{i,j}, \tag{3.65}$$

so that the average t.o.f. density is

$$\mathcal{S}_{\mathrm{Mott}}\left(\mathbf{K}\right) \approx N_s n_0 = N. \tag{3.66}$$

The disappearance of the Bragg peaks from the t.of. pattern was the first experimental signature of the superfluid to Mott insulator transition, observed in the Munich group in 2002 [18] after a proposal in [27]. This is shown pictorially in Figure 3.7. Importantly, the experiment proved that the loss of phase coherence was *reversible*, *i.e.* an interference pattern was restored after performing a ramp back to the superfluid regime. This step was crucial to show that phase coherence was not due to a parasitic effect, *e.g.* heating above the critical temperature when ramping up the lattice potential.

3.3.2. Noise correlations

In the Mott state, the t.o.f. distribution (3.66) seems completely featureless, part from the global Gaussian-like envelope determined by the Wannier functions at each site. Yet information about the initial state is still present, and can be revealed by noise analysis [48]. Let us consider the correlation function of the t.o.f. pictures given by

$$\langle n_{\mathrm{tof}}(\mathbf{K}) n_{\mathrm{tof}}(\mathbf{K}')\rangle = \mathcal{G}\left(\mathbf{K}\right)\mathcal{G}\left(\mathbf{K}'\right) \sum_{i,j,k,l} e^{i\mathbf{K}\cdot(\mathbf{r}_j-\mathbf{r}_i)+i\mathbf{K}'\cdot(\mathbf{r}_l-\mathbf{r}_k)} \langle \hat{a}_i^\dagger \hat{a}_j \hat{a}_k^\dagger \hat{a}_l\rangle \tag{3.67}$$

The spatial correlation function in the initial state (before release) can be rewritten as a normal-ordered correlation function plus an autocorrelation term,

$$\langle \hat{a}_i^\dagger \hat{a}_j \hat{a}_k^\dagger \hat{a}_l\rangle = \langle \hat{a}_i^\dagger \hat{a}_k^\dagger \hat{a}_j \hat{a}_l\rangle + \langle \hat{a}_i^\dagger \hat{a}_l\rangle \delta_{kj}. \tag{3.68}$$

The second term gives a contribution

$$\mathcal{G}\left(\mathbf{K}\right)\mathcal{G}\left(\mathbf{K}'\right) \sum_{i,l} e^{i(\mathbf{K}'\cdot\mathbf{r}_l - \mathbf{K}\cdot\mathbf{r}_i)} \langle \hat{a}_i^\dagger \hat{a}_l\rangle \times \sum_j e^{i(\mathbf{K}-\mathbf{K}')\cdot\mathbf{r}_j} = N_s \delta(\mathbf{K}-\mathbf{K}') \langle n_{\mathrm{t.o.f.}}\rangle.$$

This term accounts for the autocorrelation of each particle with itself. It is always present in a density-density correlation function, and do not carry any particular information. We omit it for the rest of the discussion.

The normal-ordered correlation is the interesting term. For an array of Fock states with n_0 atoms per site, as given in (3.32), one can evaluate it explicitly,

$$\langle \hat{a}_i^\dagger \hat{a}_k^\dagger \hat{a}_j \hat{a}_l\rangle_{\mathrm{Mott}} = n_0^2 \left(\delta_{i,j}\delta_{k,l} + \delta_{i,l}\delta_{k,j}\right) - n_0 \delta_{i,j}\delta_{i,k}\delta_{i,l}. \tag{3.69}$$

Plugging this back into Eq. (3.67), one finds

$$\langle n_{\mathrm{tof}}(\mathbf{K}) n_{\mathrm{tof}}(\mathbf{K}')\rangle = \mathcal{G}\left(\mathbf{K}\right)\mathcal{G}\left(\mathbf{K}'\right) \left(n_0^2 N_s^2 + n_0^2 \sum_{i,j} e^{i(\mathbf{K}-\mathbf{K}')\cdot(\mathbf{r}_j-\mathbf{r}_i)} - N_s n_0 \right). \tag{3.70}$$

When discussing the spatial behavior of density-density correlation functions, one should take care to separate the variations that are already there in the average density from those that are genuinely correlation features. In analogy with quantum optics, we thus consider the normalized second-order correlation function

$$g^{(2)}_{\mathrm{Bosons}}(\mathbf{K};\mathbf{K}') = \frac{\langle n_{\mathrm{tof}}(\mathbf{K}) n_{\mathrm{tof}}(\mathbf{K}')\rangle}{\langle n_{\mathrm{tof}}(\mathbf{r},t)\rangle \langle n_{\mathrm{tof}}(\mathbf{r}',t)\rangle} \approx 1 + \frac{1}{N_s^2} \sum_{i,j} e^{i(\mathbf{K}-\mathbf{K}')\cdot(\mathbf{r}_j-\mathbf{r}_i)}, \tag{3.71}$$

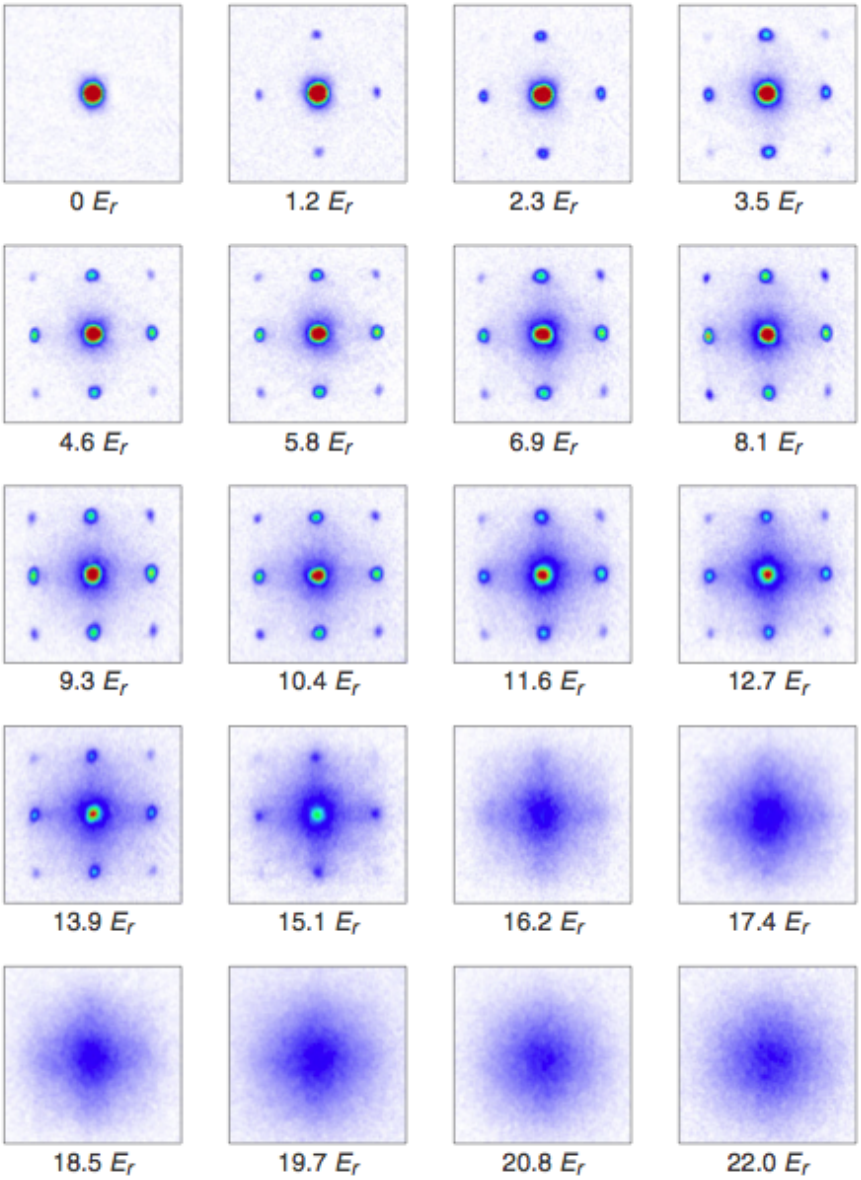

Figure 3.7.: Series of t.o.f. pictures of a cold bosonic gas released from a 3D cubic lattice [Figure taken from the PhD thesis of Markus Greiner [47]].

where a small term $\propto 1/N$ has been neglected compared to 1. The second term displays Bragg-like interference peaks, spaced by a reciprocal lattice vector. Figure 3.9A1-B1 shows experimental results that confirm this prediction [49]. We will now give a different point of view that allows one to understand better the fundamental nature of these results.

Interpretation in terms of the Hanbury-Brown and Twiss effect : The interpretation of this result is illustrated in Fig.3.8 for two particles trapped at well-defined sites of a one-dimensional lattice. The quantity above is the number of particles jointly detected at x and $x' = x + l$. Consider first only two atoms tightly localized at two particular site i and j. There are two possibilities to detect them: (1) the first atom starts from site i and flies to point x, and the second starts from j and flies to x', or (2) the reverse, the first atom starts from i and flying to x', while the second starts from j and flies to x. The quantum mechanical amplitudes associated to each of these two processes should be added to obtain the total amplitude $\mathcal{A}(x, x')$ for joint detection,

$$\mathcal{A}(x, x') \propto e^{i(Kx_i + K'x_j)} + e^{i(K'x_i + Kx_j)}, \tag{3.72}$$

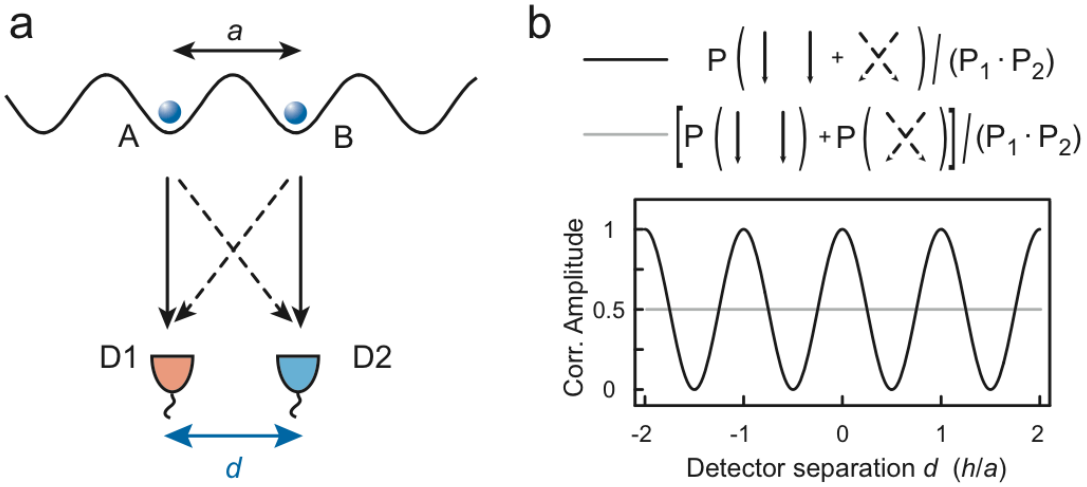

Figure 3.8.: Hanbury-Brown and Twiss experiment with two atoms released from an optical lattice. Illustration of the correlation effect for two *localized* particles.

with $K(K') = m_a x(x')/\hbar t$. The probability for joint detection then displays interferences as the path difference is varied by varying $|x - x'|$,

$$\mathcal{P}(x, x') = |\mathcal{A}(x, x')|^2 \propto 1 + \cos\left(2\pi \frac{x - x'}{d_{\rm tof}} \frac{x_i - x_j}{d}\right), \tag{3.73}$$

with $d_{\rm tof} = 2\hbar k_L t/m_a$. This is an illustration of the Hanbury-Brown-Twiss effect, which was first observed with classical waves [50, 51] but is now considered as a pillar of quantum optics [52]. For $x \approx x'$, the interference is constructive for bosons (exchanging the two paths yields a phase of 2π): the probability to find two bosons at the same point is enhanced compared to classical particles.

Consider now a 1D string of N_s atoms (unity filling), and as a first step, let us single out one particular atom (say 1). The above two-particle effect now exists for each possible pair formed with atom 1 and another atom i, but due to the regular filling the relative phase between the amplitude associated to pair $(1, i)$ and $(1, j)$ is fixed and depends of $i - j$ only. The two-particle amplitude associated to the pairs $(1, j)$ therefore add constructively for the value of $(x - x')$ that match the Bragg conditions $m_a(x - x')/\hbar t = p2\pi/d$ with p integer. One thus finds that a "grating-like" interference pattern constructs instead of the simpler double-slit pattern found for just two atoms. As a second step, we note that that the atom 1 has nothing special, and that for each atom in the string the same total amplitude is found, adding constructively to the total signal.

If the atoms can be considered as "localized" , but with random positions (a hot Bose gas without a lattice), then the different amplitudes add with random phases. After the first step only, a density modulation would still exists (albeit probably a very irregular one). However the interference pattern disappears after the second step since all modulations are uncorrelated: only a peak near zero momentum survives (with a width $\sim$ the De Broglie wavelength). With a special detection system (which only works with metastable atoms, such as ^{4}He), such correlations can be detected [53] but they are usually buried in the noise for traditional absorption images. However, with a tight lattice (and a "hot" gas filling the lowest Bloch band almost uniformly), the same reasoning applies as for the Mott state above: translational order and bosonic statistics are enough to restore the correlation peak.

On the contrary, in the condensate case, the atomic wave function is instead completely delocalized over the lattice. Already, the first step involves coherent summation of amplitudes over all possible positions of the first atom in the lattice, each of these carrying a different phase. In the limit of a large lattice, this is already sufficient to kill the interference and to flatten $g^{(2)}$. In other words, the second order correlation function factorizes,

$$\langle \hat{n}(\mathbf{K})\hat{n}(\mathbf{K}')\rangle_{BEC} = \quad \langle \hat{n}(\mathbf{K})\rangle_{BEC}\langle \hat{n}(\mathbf{K}')\rangle_{BEC},$$

or $g^{(2)}(\mathbf{K}, \mathbf{K}') = 1$. This is often called "second-order coherence" in analogy with optics. We note finally that, for the thermal gas case, as the De Broglie wavelength becomes larger than a lattice spacing, the atoms are increasingly delocalized over the lattice, and smearing of the correlation should also occur progressively with a suppression factor scaling as $(d/\lambda_{dB})^3$.

Finally, figure 3.9C1-D1 shows experimental results for this quantity for fermions in a band insulator state [54]. The argument goes along the same lines as for the bosonic Mott insulator state, except that now the interference is

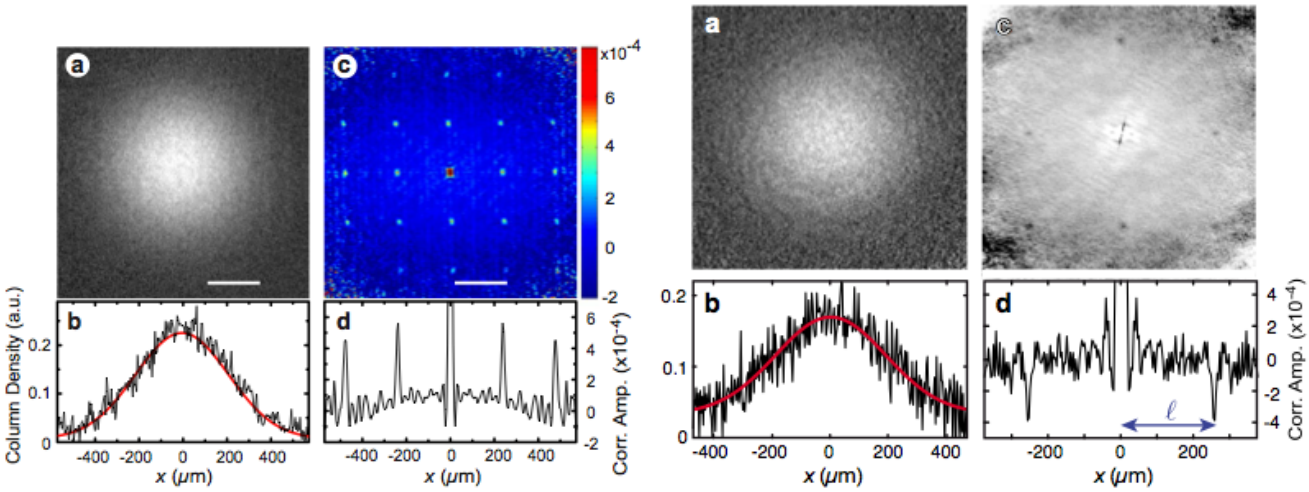

Figure 3.9.: Noise correlations for atoms relased from optical lattices. Figures A1, B1 correspond to absorption images of bosonic clouds in the Mott insulator regime [49]: A is the average density and B the density-density correlation function. C1 and D1 are the same figures but for fermionic clouds [54], where anti-correlations appear instead of correlations.

destructive (the phase associated with exchanging the path is π),

$$g^{(2)}_{\text{Fermions}}(\mathbf{K};\mathbf{K}') \approx 1 - \frac{1}{N_s^2}\sum_{i,j} e^{i(\mathbf{K}-\mathbf{K}')\cdot(\mathbf{r}_j-\mathbf{r}_i)}, \tag{3.74}$$

This results in a lattice of anti-correlation peaks with the same geometry as the reciprocal lattice, as observed experimentally.

3.4. Particle-hole excitations in a Mott insulator

3.4.1. Strong-coupling expansion for a Mott insulator

In Section 3.2.4 we have considered only the ground state of the Bose-Hubbard model using the Gutzwiller ansatz. For a commensurate filling $\overline{n} = n_0$, we found a transition between a delocalized state and a perfect array of Fock states at a finite U/J. Our aim in this Section is to emphasize that this is actually an artifact of the Gutzwiller ansatz, and that the real ground state still features residual motion in the form of particle-hole excitations.

This can be seen by starting from the limit $J = 0$ and treating the tunneling term as a perturbation (strong-coupling expansion). For $J = 0$, the Fock state $|\Psi_0\rangle = \prod_i |n_0\rangle_i$ is the ground state with energy $E_0[N] = N_s\left(\frac{U}{2}n_0(n_0-1) - \mu n_0\right)$, with $N = n_0 N_s$ the total atom number and N_s the number of sites. The lowest excited states are created by removing or adding one particle to a given site,

$$|p : \boldsymbol{r}_i\rangle = \frac{1}{\sqrt{n_0+1}}\hat{a}_i^\dagger|\Psi_0\rangle, \tag{3.75}$$

$$|h : \boldsymbol{r}_i\rangle = \frac{1}{\sqrt{n_0}}\hat{a}_i|\Psi_0\rangle, \tag{3.76}$$

with energies

$$E_p = E_0[N] + Un_0 - \mu, \tag{3.77}$$

$$E_h = E_0[N] + \mu - U(n_0-1). \tag{3.78}$$

The labels "p" and "h" stand for "particles" and "holes", respectively. These states are not directly connected to the ground states, since the total particle number differ by ± 1. Hence we need to consider composite "particle-hole" states of the form,

$$|p : \boldsymbol{r}_i, h : \boldsymbol{r}_j\rangle = \frac{1}{\sqrt{n_0(n_0+1)}}\hat{a}_i^\dagger\hat{a}_j|\Psi_0\rangle. \tag{3.79}$$

Such a state describes an excitation with one extra atom at site i and a missing one ("hole") at site j. Such excitations have an energy

$$E_{ph} = E_0[N] + U. \tag{3.80}$$

Ground state for $J \neq 0$: We now introduce tunneling $\hat{T} = -J\sum_{\langle i,j\rangle} \hat{a}_i^\dagger \hat{a}_j$ and compute the new ground state using first-order perturbation theory with the small parameter J/U,

$$|\Psi_g\rangle \approx |\Psi_0\rangle + \sum_{\nu\neq 0} \frac{J}{E_\nu - E_0}\langle\Psi_\nu|\hat{T}|\Psi_0\rangle \approx |\Psi_0\rangle + \frac{J\sqrt{n_0(n_0+1)}}{U}\sum_{\langle i,j\rangle} |p:\boldsymbol{r}_i, h:\boldsymbol{r}_j\rangle. \tag{3.81}$$

Here we noted $|\Psi_\nu\rangle$ the excited many-body states with energy E_ν, and used the fact that $\hat{T}$ couples the ground state only to excited states of the particle-hole type with i and j nearest-neighbors. We conclude that the true ground state is not a perfect array of Fock states, but instead features an admixture of particle-hole excitations localized (to this order of perturbation) on neighbouring sites. Pushing perturbation theory to order n will allow the particle and hole to "separate" and move to larger distances nd, with an amplitude $\sim (J/U)^n$. This leads to the qualitative conclusion that the first-order correlation function $\mathcal{C}(i,j)$ should decay exponentially with a coherence length $\sim d$, a conclusion supported by numerical investigation and by experiments.

Excited states for $J \neq 0$: The excited states are modified by the small tunneling perturbation in a different way. All particle and all hole states are degenerate, and tunneling lifts this degeneracy by allowing the extra particle or hole to move through the lattice. Differently from the ground state, one has to use degenerate perturbation theory to find the new eigenstates. One can check that the "Bloch" states

$$|p:\boldsymbol{q}\rangle = \frac{1}{\sqrt{N_s}}\sum_i e^{i\boldsymbol{q}\cdot\boldsymbol{r}_i}|p:i\rangle, \tag{3.82}$$

is an eigenstate of the tunneling Hamiltonian restricted to the degenerate particle states subspace with energy

$$E_p(\boldsymbol{q}) = E_0 + Un_0 - \mu - zJ(n_0+1)\gamma_{\boldsymbol{q}}, \tag{3.83}$$

$$\gamma_{\boldsymbol{q}} = \frac{1}{z}\sum_{\boldsymbol{\delta}\,\mathrm{nn}} e^{i\boldsymbol{q}\cdot\boldsymbol{\delta}} = \frac{2}{z}\sum_{\alpha=x,y,z}\cos(q_\alpha d). \tag{3.84}$$

Here $\delta = \pm\boldsymbol{e}_x, \pm\boldsymbol{e}_y, \pm\boldsymbol{e}_z$ denotes a vector joining nearest neighbors, and the factor $\gamma_{\boldsymbol{q}} \in [-1,1]$ is the dimensionless form of the single-particle dispersion relation. A similar reasoning for the degenerate hole states subspace lead to the hole dispersion relation

$$E_h(\boldsymbol{q}) = E_0 + \mu - U(n_0-1) - \mu - zJn_0\gamma_{\boldsymbol{q}} \tag{3.85}$$

Experimental signature : The modification of the correlation function $\mathcal{C}(i,j)$ from zero range for $J=0$ to short range can be observed in time-of-flight experiments. For the corrected ground states given in Eq. (3.81), the structure factor $\mathcal{S}(\boldsymbol{q})$ determining the interference pattern is now

$$\mathcal{S}(\boldsymbol{q}) = N_s\left(1 + \frac{2zJn_0(n_0+1)}{U}\gamma_{\boldsymbol{q}}\right). \tag{3.86}$$

We conclude that a residual modulation appears on the scale of the first Brillouin zone (thus much broader than the narrow Bragg peaks of the superfluid state), with an amplitude $\sim 2zJn_0(n_0+1)/U$ that vanishes in the limit of completely disconnected wells but is finite otherwise.

This decay was observed experimentally by monitoring the evolution of the "visibility" of the interference pattern [55], defined as

$$V = N_s\frac{\mathcal{S}(\boldsymbol{q}_1) - \mathcal{S}(\boldsymbol{q}_2)}{\mathcal{S}(\boldsymbol{q}_1) + \mathcal{S}(\boldsymbol{q}_2)}. \tag{3.87}$$

In the usual definition of visibility used for optical interferometers, $\boldsymbol{q}_{1/2}$ are chosen to correspond to the maxima and minima of the optical intensity. For our case, a convenient choice is indicated in Figure 3.10 where the white dot shows the location of q_1 at one of the Bragg spot, and the black dot the location of q_2, which is not exactly at the minimum but at the same radial distance from the central peak. In this way, the envelope $\mathcal{G}$ cancels out automatically when taking the ratio and the visibility V can be evaluated directly from the images. The experimental results shown in Figure 3.10 confirm clearly the residual short-range coherence in the Mott insulator phase and its expected scaling with U/J [55].

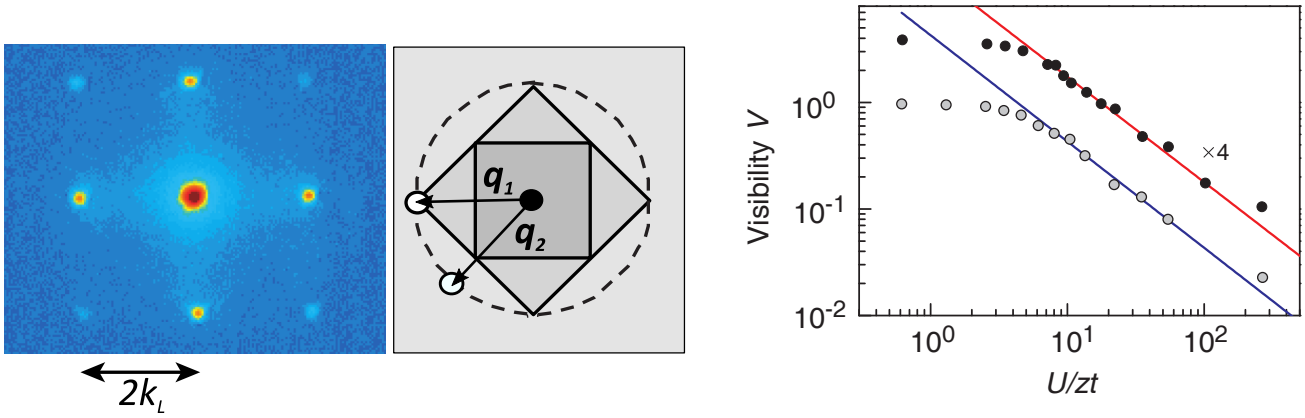

Figure 3.10.: Left : experimental time-of-flight picture. Middle : Sketch of the Brillouin zone, showing the locations where the maximum and minimum are evaluated to obtain the visibility. Right: Experimental visibility for different filling at the trap center ($n_0 = 1$ and $n_0 = 2$), demonstrating the slow decay $\propto zJ/U$ of the visibility in the Mott insulator phase. According to mean-field theory, the MI transition is expected at $V_0 \approx 13\, E_R$ and $V_0 \approx 15\, E_R$ for $n_0 = 1$ and $n_0 = 2$.

3.4.2. Lattice modulation spectroscopy

Another piece of evidence for the existence of particle-hole excitations as well-defined quasi-particles of a Mott insulator comes from lattice modulation spectroscopy. In this type of experiments, the lattice depth is modulated at a frequency $\omega_{\rm mod}$, *i.e.* the potential is now of the form

$$V(t) = V_{\rm lat}(\boldsymbol{r})\left[1 + \epsilon\cos(\omega_{\rm mod}t)\right]. \tag{3.88}$$

with $\epsilon \ll 1$. In the Hubbard regime, the small modulation of the potential does not affect the band structure, and simply results in modulated tunneling and interaction parameters. The former largely dominates over the latter, because the tunneling energy is exponentially sensitive to the lattice depth V_0. As a result, the problem can be modelled by a time-dependent perturbation

$$H_{\rm mod} \approx -\frac{1}{J}\frac{dJ}{dV_0}\epsilon\cos(\omega_{\rm mod}t)\hat{T} \tag{3.89}$$

on top of the time-independent Bose-Hubbard Hamiltonian. This perturbation generates excitations with energy close to the "modulation quantum" $\hbar\omega_{\rm mod}$. Figure 3.11 shows the result of such experiments for varying lattice depths. In the superfluid regime (shallow lattices), one finds a broad continuum of excitations. This corresponds to excitations of collective modes ("phonons") which are qualitatively similar from the one found in the continuum using Bogoliubov's approach. The spectrum is gapless, so that one can find resonant excitations for any $\omega_{\rm mod}$ (the overall shape of the spectrum is not necessarily flat : it determined, among other things, by the excitation *strength* – *i.e.* the matrix element of the perturbation– and by the density of final states, both depending in general on the excitation energy). Conversely, for deep lattices where a Mott insulator is presumably present, the excitations are concentrated around well-defined peaks. The peak at $\hbar\omega_{\rm mod} = U$ is in accordance with our understanding of the spectrum of the Mott state and of the structure of the perturbation term, which directly generates particle-hole excitations of energy U independently of the density distribution. The presence of harmonics at $\hbar\omega_{\rm mod} = 2U, \cdots$ stems from the non-linear nature of the excitation : for strong driving (as done in this experiment) the linear response is unsufficient to account for the results [56]. Going beyond linear response predicts that excited states with more than one particle-hole pair are generated, corresponding to multiple of the on-site interaction, as well as processes where two modulation quanta can be absorbed (leading to a resonance peak near $U/2, \cdots$).

3.5. Transport experiments

3.5.1. Moving optical lattice

In this Section, we consider experiments performed in a *moving optical lattice*, where the potential takes the form

$$V_{\rm lat} = V_0\sin(k_L x - \delta t)^2 \tag{3.90}$$

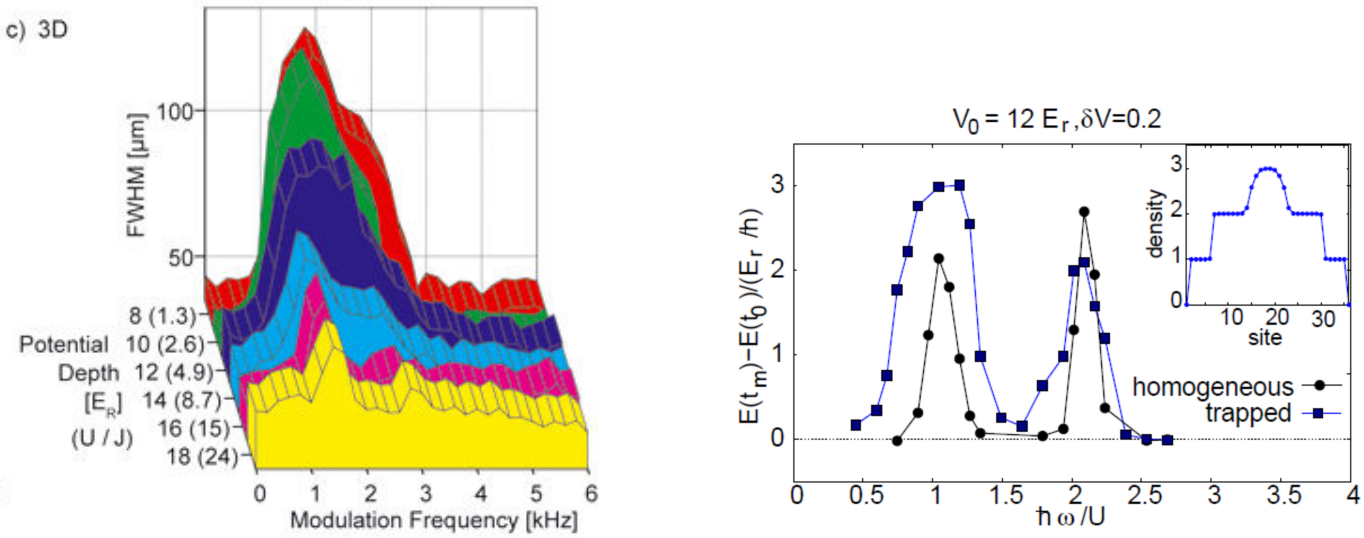

Figure 3.11.: Lattice modulation spectroscopy. Left: experimental results showing the energy absorbed by the system (as measured by the increase in the size after tof) versus frequency, for different lattice depths [57]. Right: theoretical modelling in 1D (using time-dependent density matrix renormalization group techniques) [56]. The circles are for a uniform system, while the squares are for a system with an additional harmonic trap.

The plane of constant potential travel with a velocity $v = \delta/k_L$. If we go to the moving frame where the potential is stationary, the potential is now stationary. In quantum mechanics, the change of reference frame from the lab frame to the moving frame is expressed by a unitary transformation ("Galilean boost"),

$$\hat{U} = e^{-i\frac{m_a\hat{\boldsymbol{x}}\cdot\boldsymbol{v}+\hat{\boldsymbol{p}}\cdot\boldsymbol{v}t}{\hbar}} = e^{-i\frac{m_a\boldsymbol{v}^2 t}{2\hbar}} e^{-i\frac{m_a\hat{\boldsymbol{x}}\cdot\boldsymbol{v}}{\hbar}} e^{-i\frac{\hat{\boldsymbol{p}}\cdot\boldsymbol{v}t}{\hbar}}, \tag{3.91}$$

where we used the Baker-Campbell-Hausdorff formula to split the exponential into a phase shift, a momentum translation by $-m_a\hat{\boldsymbol{v}}$ and a spatial translation by $-\boldsymbol{v}t$. The Hamiltonian in the moving frame is

$$\hat{H}' = \hat{U}^\dagger \hat{H} \hat{U} + i\hbar \frac{d\hat{U}^\dagger}{dt}\hat{U} = \frac{\left(\hat{\boldsymbol{p}} - m_a\hat{\boldsymbol{v}}\right)^2}{2m_a} + V_0 \sin(k_L x) + m_a \dot{v}\hat{\boldsymbol{x}}. \tag{3.92}$$

The quasi-momentum (which is still a good quantum number) becomes in the moving frame $\boldsymbol{q}' = \boldsymbol{q} - m_a\boldsymbol{v}/\hbar$ with $\boldsymbol{v} = v\boldsymbol{e}_x$: A Bloch state $|q\rangle$ in the lab frame thus becomes $|q - m_a v/\hbar\rangle$ in the moving frame.

Neglecting interactions, a condensate in such a moving lattice corresponds to the Bloch state with quasi-momentum zero in the lab frame, and $q' = -\frac{m_a v}{\hbar}$ in the moving frame. Assuming the lattice velocity is small compared to the width of the Brillouin zone, one can approximate the Bloch dispersion by $\varepsilon(q) \approx \hbar^2 q^2/(2m^*)$ with $m_a^* = \frac{d^2\varepsilon(q)}{dq^2}$ the effective mass. The condensate thus moves with a group velocity $v_g = -\frac{m_a}{m^*}v$ in the moving frame, or $v_{\mathrm{BEC}} = v + v_g = \left(1 - \frac{m_a}{m^*}\right)v$ in the lab frame. We thus conclude that two regimes exist depending on the depth of the lattice :

- for shallow lattices with $V_0 \lesssim E_R$, one has $m^* \approx m_a$, $v_{\mathrm{BEC}} \approx 0$ and the condensate remains essentially at rest.
- for deep lattices with $V_0 \gg E_R$, one has instead $m^* \ll m_a$, $v_{\mathrm{BEC}} \approx v$, and atoms are dragged by the moving lattice.

We stress that this behaviour is a consequence of the *single-particle* dynamics in a moving periodic potential, and has nothing to do with superfluidity or its absence (there is no "friction" exerted by the moving lattice, as would be the case for the seemingly related case of superfluid Helium in a moving container).

Interactions can significantly modify this simple picture and lead to remarkably rich behaviour. Here we only mention that the motion of a superfluid atomic cloud can be disrupted by two different effects :

- an energetic instability, where it becomes energetically favorable to remove condensed atoms and emit phonons. This is similar to the continuum case where it leads to the famous Landau criterion for superfluidity,
- a dynamic instability, where one excitation mode of the moving condensate becomes unstable and undergoes exponential growth. Figure 3.13 shows that this is specific to the lattice band structure. If we consider two atoms

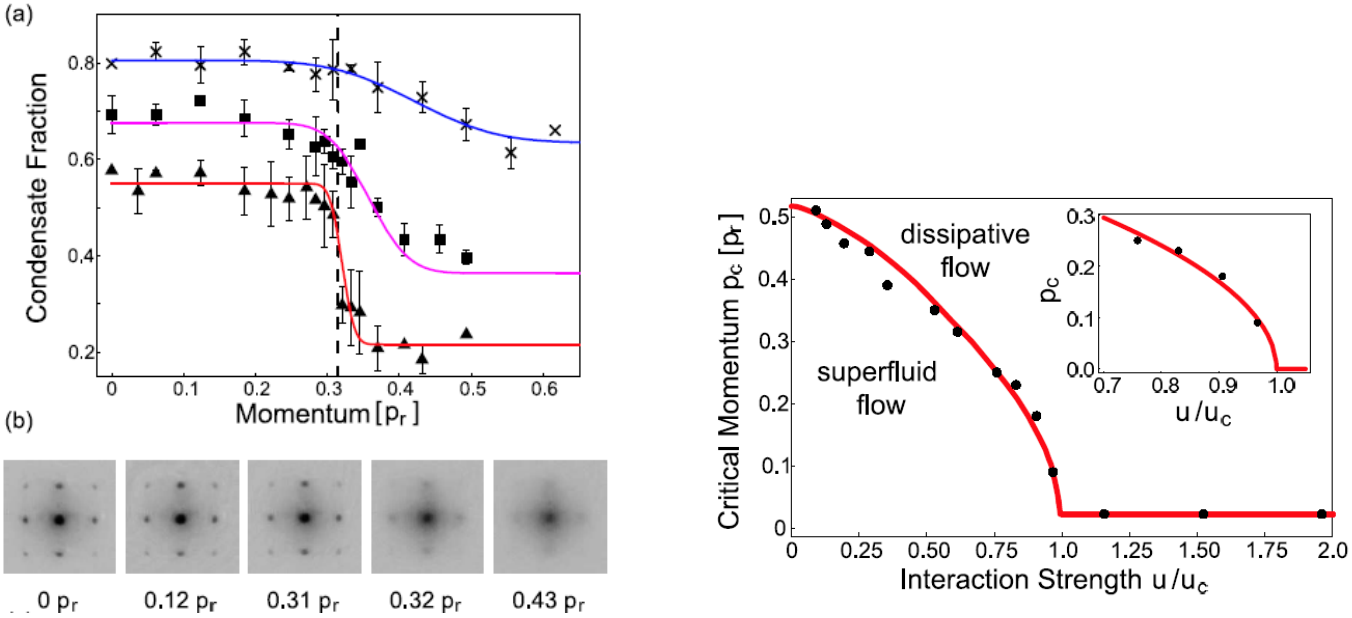

Figure 3.12.: Experiment of [58] looking for dissipation in a moving lattice with modulated velocity [Eq. 3.93]. Left : remaining fraction of condensed atoms after one (crosses), two (squares) or three (triangles) cycles of modulation. A sharp transition where superfluid flow does not survive the moving lattice emerges. The images show the interference pattern after expoising the sample to the moving lattice. Right: Phase diagram showing the critical momentum p_c where superfluid flows disappears. p_r denotes the recoil momentum $\hbar k_L/m_a$.

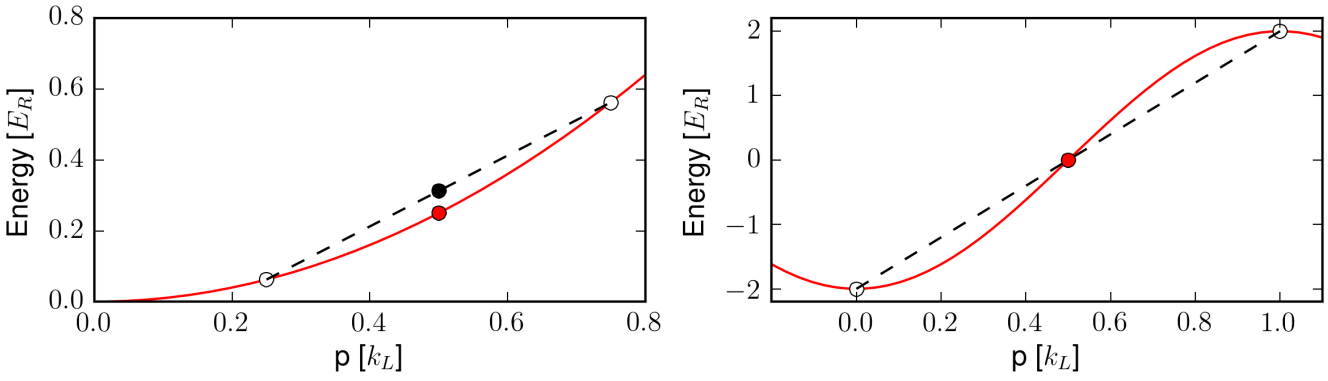

Figure 3.13.: Available phase space for a collision between two particles with the same momentum p_0 in the lab frame in free space (left) and in the lattice (right).

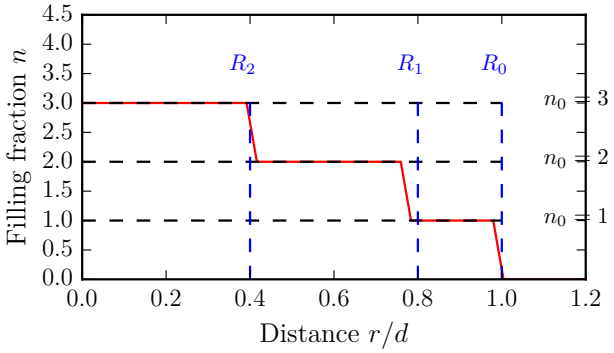

Figure 3.14.: Shell structure of a trapped Mott insulator for $J = 0$, $\mu = 2.4U$.

with equal momentum p_0 in the continuum, the parabolic dispersion relation forbids to fulfill simultaneously the conservation of energy and momentum: There are no available final states for a collision where the two atoms change their momentum (see left panel in Figure 3.13). In the lattice, due to the band structure the situation is different. Two atoms with quasi-momentum $p_0 = k_L/2$, for instance, can collide and transfer one atom to $q = 0$ and the second one to $q = k_L$. The band structure enables conservation of energy that was forbidden in the free particle case (see right panel in Figure 3.13). Similar phenomenon appear in non-linear optics (with optical non-linearities providing the analog of the interactions), where they are known as "modulational instabilities".

A more detailed discussion of the various instabilities can be found in the review [59] and in the references quoted in this article. For our purpose, the important conclusion from these studies is that for a superfluid state moving in an optical lattice, there is a critical current (or equivalently, critical momentum p_c) where superfluid flow becomes unstable. In the weakly-interacting (Gross-Pitaevskii) limit, this critical momentum is $p_c = \hbar k_L/2$ (see Figure 3.13).

3.5.2. Critical velocity for a Bose-Hubbard system

How does the critical momentum change when interactions become stronger ? This question was adressed experimentally in [58] following theoretical work in [60, 61]. In this work, a static condensate was submitted to a moving lattice. For technical reasons, the lattice velocity was modulated at low frequencies,

$$v(t) = \frac{p_m}{m_a} \cos(\omega_{\mathrm{mod}} t) \tag{3.93}$$

for a given time. Figure 3.12 shows the result of the experiment, which records the "condensed fraction" (the fraction of atoms surviving in the Bragg peaks of the interference pattern) after several modulation cycles. The superfluid survives for a range of modulation amplitudes p_m up to a critical value p_c. Recording p_c for various interaction strength, the authors find that it decreases with increasing lattice depth (equivalently, with increasing U) until a critical U_c where it vanishes. This experiment illustrate in a clear way the change in the transport properties of the bosons, with the clear inability to sustain superfluid motion above U_c. The measured value of $U_c \approx 34.2J$ was found to be in excellent agreement with the Gutzwiller ansatz prediction ($U_c/J \approx 34.8$), but in disagreement with the result of Monte-Carlo simulations ($U_c/J \approx 29$) which are in principle more accurate. Both predictions were made at $T = 0$, and for a uniform system, and the authors of [58] conjecture that small experimental differences could be explained by either a finite temperature or the trapping potential.

3.6. Shell structure in a trap

3.6.1. Auxiliary potential due to the Gaussian laser beams

Actual lasers used in experiments are of course not plane waves (as assumed so far) but instead have a Gaussian spatial profile, with a modulus (near the beam focus[7]) of the form $E(\mathbf{r}) = E_0 e^{-(y^2+z^2)/w^2}$. For red detunings, the full potential for a one-dimensional lattice is

$$V_{1\mathrm{D}} = -V_0 \left(1 - \sin^2(k_L x)\right) e^{-2\frac{y^2+z^2}{w^2}}. \tag{3.94}$$

[7] Strictly speaking, there is also an additional dependence on z on the scale of the Rayleigh length, $z_R = \pi w^2/\lambda_L$. Typically this dependence is negligible compared to the transverse variations, since $z_R \gg w$.

Here we took the laser wave vector along x, and introduced the waist w giving the typical length scale over which the intensity varies in the plane transverse to the propagation direction. Typically, the length scale w that dictates the modulation of the lattice depth is chosen to be large compared to the dimensions of the atomic cloud (and by extension much larger than the lattice period). As a result, the lattice potential is weakly modulated by the Gaussian laser beam envelope. Until now, we have neglected this perturbation of the periodic potential for the sake of simplicity. Most of what we have discussed is not qualitatively altered when taking it into account, because the modulation varies smoothly on the scale of the lattice spacing. However, in order to understand the spatial structure of atomic Mott insulators, this feature plays an important role and cannot be ignored.

We now consider how this affects the atoms in a 3D lattice, in the regime where the BH model is valid. In the usual experimental regime where the cloud dimensions are small compared to w, one can approximate $e^{-2\frac{y^2+z^2}{w^2}} \approx 1 - 2\frac{y^2+z^2}{w^2}$, and treat the non-periodic part $\delta V_{1\mathrm{D}} = 2V_0\left[1-\sin^2\left(k_L x\right)\right]\frac{y^2+z^2}{w^2}$ perturbatively. In the Wannier basis, the modified optical potential δV_{x} due to the standing wave creating the x lattice reads

$$\begin{aligned}\delta V_{\mathrm{x}} = &\sum_i \frac{2V_0}{w^2} \times \int \cos^2\left(k_L x\right) w(x-x_i)^2 dx \times \int y^2 w(y-y_i)^2 dy \times \hat{a}_i^\dagger \hat{a}_i \\ &+ \sum_i \frac{2V_0}{w^2} \times \int \cos^2\left(k_L x\right) w(x-x_i)^2 dx \times \int z^2 w(z-z_i)^2 dz \times \hat{a}_i^\dagger \hat{a}_i. \end{aligned} \tag{3.95}$$

We consider (to be coherent with the Bose-Hubbard model) a sufficiently deep lattice, such that the Wannier functions are well-localized around each site. We note σ_{W} their r.m.s. spread[8], such that $\sigma_{\mathrm{W}}^2 = \int x^2 w(x)^2 dx \ll d^2$. The potential term becomes

$$\delta V_{\mathrm{x}} \approx \sum_i \frac{2V_0}{w^2} \times \left[1 - \frac{1}{2}\left(k_L \sigma_{\mathrm{W}}\right)^2\right] \times \left(y_i^2 + z_i^2 + 2\sigma_{\mathrm{W}}^2\right) \hat{a}_i^\dagger \hat{a}_i.$$

Apart from a uniform shift, the potential term reads

$$\delta V_{\mathrm{x}} \approx \sum_i \frac{1}{2} m_a \Omega^2 \left(y_i^2 + z_i^2\right) \hat{a}_i^\dagger \hat{a}_i, \tag{3.96}$$

with $\Omega^2 = \left(4V_0/m_a w^2\right)\left[1 - \left(k_L\sigma_{\mathrm{W}}\right)^2/2\right]$. The calculation is approximate and valid if $\sigma_{\mathrm{W}} \ll d \ll w$, a hierarchy usually satisfied for actual Bose-Hubbard systems. The same reasoning applies for the y and z lattices. We thus find that the modulation of the lattice depth due to the Gaussian envelope of the laser intensity amounts to an additional harmonic potential superimposed on the optical lattice. In some experiments, the magnetic or optical trap in which the condensate is produced in the first place is maintained as well. The total potential added to the periodic part is then also harmonic, with total frequencies given by the quadratic sum of the initial trap frequencies and of the additional confinement due to the lattice lasers. Note that the confinement strength Ω increases with V_0, so that the harmonic trap is not independent of the Bose-Hubbard parameters J, U.

The two terms contributing to the "auxiliary" trap frequency Ω can be interpreted as follows. Moving away from the trap center, the energy at the potential minima increases with position because of the Gaussian envelope. This corresponds to the first contributing term, but also implies a variation of the zero-point energy of atoms trapped near the minima. Approaching the lattice potential by an harmonic oscillator potential with frequency $\omega_{\mathrm{lat}} = 2\sqrt{V_0(\boldsymbol{r}_i)E_R}$ near the site at $\boldsymbol{r}_i$ (see Section 2.2.4), the local zero-point energy can be written $\frac{\hbar\omega_{\mathrm{lat}}}{2}\sqrt{1-2\left(\frac{x_i}{w}\right)^2} \approx \frac{\hbar\omega_{\mathrm{lat}}}{2} - \frac{\hbar\omega_{\mathrm{lat}}}{2w^2}x_i^2$. The site-dependent correction leads (using $\sigma_{\mathrm{W}} \approx \sqrt{\hbar/m_a\omega_{\mathrm{lat}}}$) to the second term contributing to Ω. Higher-order corrections scale as powers of $k_L\sigma_{\mathrm{lat}}$, which must be $\ll 1$ for the derivation to be valid. In practice, the error made by Taylor expansion of the cosine inEq. 3.95 is less than 5

3.6.2. Local density approximation

The auxiliary harmonic potential V_{h} breaks the discrete translational invariance of the lattice, so that strictly speaking one cannot apply Bloch theorem anymore. Fortunately, in most cases the harmonic confinement is weak enough to enable a local density approximation (LDA). This approximation considers a large system with smoothly varying density profile. One can then divide (mentally) the system into cells which are at the same time quasi-macroscopic (in the sense that they contain a large number of atoms so that thermodynamics can be applied) and quasi-homogeneous (in the sense that the gradient of density is weak and can be neglected over the extent of the cell). Then for each cell centered at $\mathbf{r}$, one can define a local chemical potential,

$$\mu_{\mathrm{loc}}(\mathbf{r}) = \mu - V_{\mathrm{h}}(\mathbf{r}), \tag{3.97}$$

[8] Using the harmonic oscillator ground state as an approximation for the Wannier functions (section 2.2.4), one has $\sigma_{\mathrm{W}} \approx k_L^{-1}(E_R/V_0)^{1/4}$.

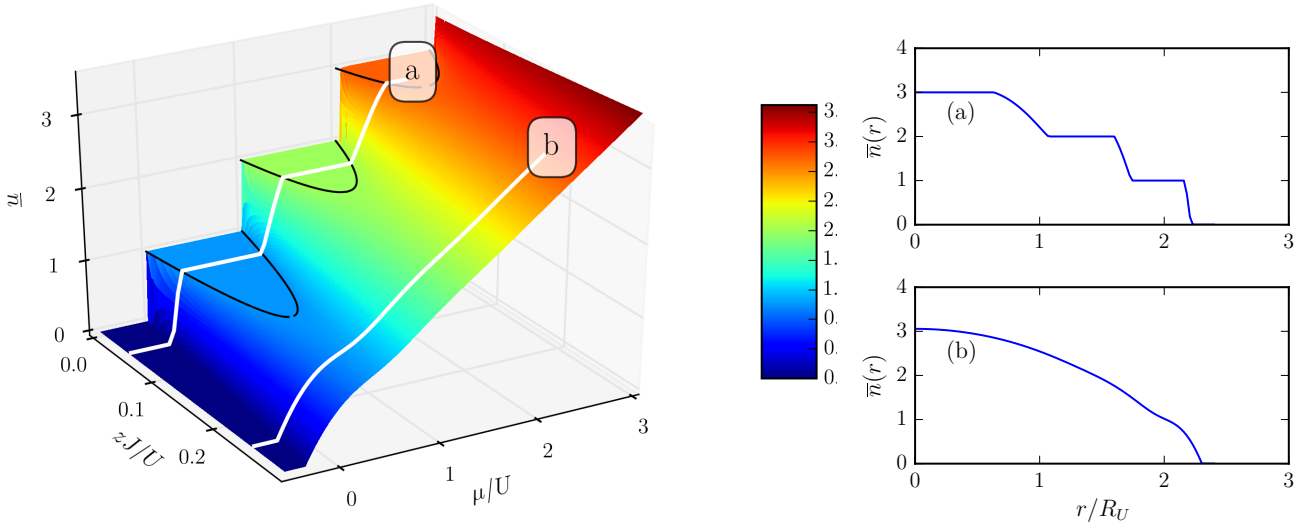

Figure 3.15.: Shell structure of a trapped Mott insulator. The left plot reproduces the phase diagram of the uniform Bose-Hubbard model in a tunneling J-chemical potential μ plane (U is the interaction energy, z the number of nearest neighbors). In the local density approximation, the density profile in a trap is obtained by a scan of the chemical potential $\mu_{\rm loc}(\boldsymbol{r}) = \mu - V(\boldsymbol{r})$ at constant J, with μ the global chemical potential and $V(\boldsymbol{r})$ the trap potential. Two examples in the Mott (a) and superfluid (b) regimes are shown on the right panels.

which is simply given by the global chemical potential μ offset by the local potential energy inside the cell. The quantities can then be computed for uniform systems for given μ, and then averaged over all cells with the global constraint of a fixed total atom number N (the constraint fixes the global chemical potential μ). For instance, the density profile $n(\mathbf{r})$ reflects the equation of state of the homogeneous gas, $n[\mu_{\rm loc}(\mathbf{r})]$.

3.6.3. Mott shells

Using the LDA, one can see that the phase diagram established in the previous section will be measurable in the density profile of the gas. The center of the cloud corresponds to a given μ somewhere in the phase diagram (Figure 3.15). As one moves towards larger distances the local chemical potential follows a vertical line until it equals $-zJ$ (corresponding to the cloud edge where the density vanishes). When $\mu_{\rm loc}$ is located within the boundaries of a Mott lobe with filling p, the filling factor is uniform and density fluctuations are strongly suppressed.

In the presence of a trap, a Mott phase is thus associated to a plateau in the density (usually called “Mott shells" in the literature) [27, 62]. This is in fact a signature not only of a Mott insulator phase, but of any incompressible phase. The compressibility, defined as[9]

$$\kappa = \frac{1}{\overline{n}^2}\frac{\partial \overline{n}}{\partial \mu}, \tag{3.98}$$

clearly vanishes inside each Mott lobe where the density is pinned to an integer independently of the chemical potential. The incompressibility is a consequence of the existence of the excitation gap discussed before: “Pushing” gently on the system has no effect because one does not overcome the internal energy of the particles.

Let us see how this works in a simple case, where $J = 0$ and the auxiliary potential is isotropic, $V_{\rm h} = m_a\Omega^2 r^2/2$. According to the phase diagram for $J = 0$, the MI phase with p atoms per site is reached when the local chemical potential $\mu_{\rm loc}$ becomes equal to Up. In a trap, this corresponds to a radius R_p such that $\mu_{\rm loc} = \mu - \frac{1}{2}m_a\Omega^2 R_p^2 = pU$, *i.e.* $R_p = R_U\sqrt{\mu/U + p}$ with a characteristic radius $R_U = \sqrt{2U/m_a\Omega^2}$ (Figure 3.14). The edge of the cloud corresponds to R_0. A given, completely filled Mott shell with filling factor p is comprised between R_p and R_{p-1}, and contains $N_p = \frac{4\pi p}{3d^3}(R_{p-1}^3 - R_p^3)$ atoms. The total atom number is given by

$$N = \sum_{p=0}^{p_{\rm max}-1} N_p + \frac{4\pi p_{\rm max}}{3} R_{p_{\rm max}-1}^3, \tag{3.99}$$

[9] The usual thermodynamic definition of the isothermal compressibility is $\kappa_T = -(1/V)\partial V/\partial P = (1/\overline{n})\partial\overline{n}/\partial P$. Using the Gibbs Duhem relation for an isothermal process, $\overline{n}d\mu = dP$, one finds the form given in Eq. (3.98).

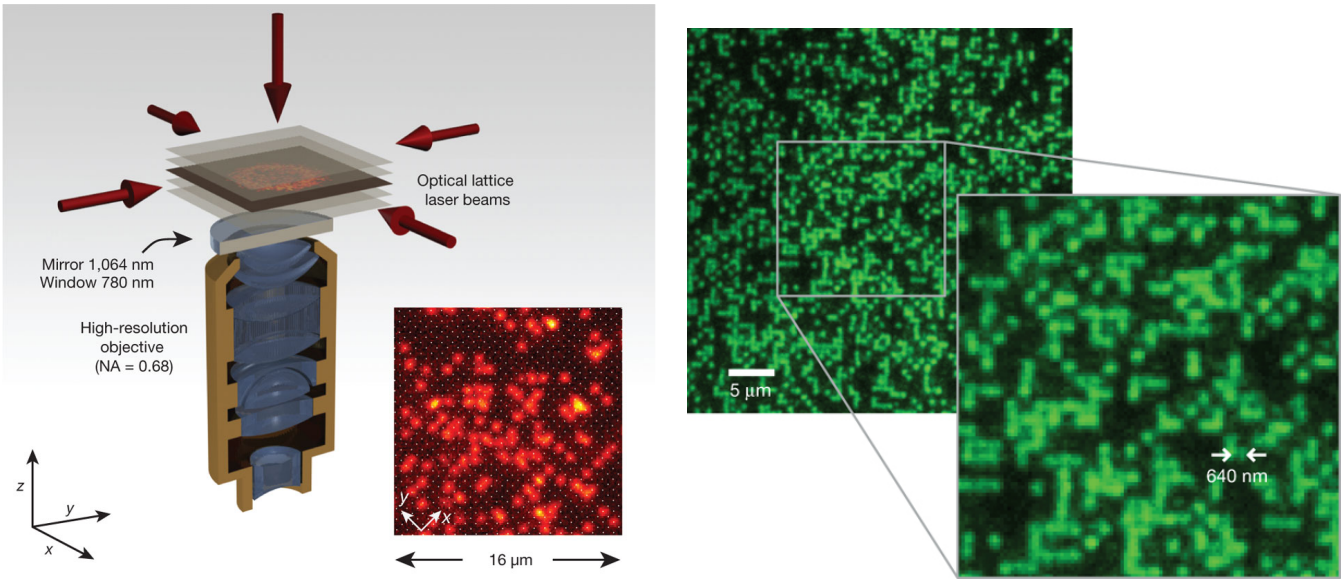

Figure 3.16.: Imaging of quantum gases at the single-atom level. Left picture (from [63]]: experimental setup and image of a diute gas. Right picture (from [64]): image of a Bose-Einstein condensate in a 2D lattice.

where the last term is the contribution from the innermost shell. The sum simplifies term by term and reads

$$N = \frac{4\pi R_U^3}{3d^3} \sum_{p=1}^{p_{\max}-1} \left(\frac{\mu}{U} + p\right)^{3/2}. \tag{3.100}$$

This relation can be inverted numerically to find μ for given experimental parameters N, Ω.

Figure 3.15 shows what happens for finite U/J larger than the critical value for the Mott transition. Two Mott shells are still present, but they are separated by superfluid layers at the interface between the $n_0 = 2$ and $n_0 = 1$ shells, and between the $n_0 = 1$ shell and the vacuum. This shell structure provides a direct evidence that an incompressible Mott phase has been formed. We will now discuss recent experiments that were able to observe it directly.

3.7. Quantum gas microscopy

3.7.1. Single-site imaging with single-atom sensitivity

Early experiments on the superfluid-Mott insulator transition were performed with three dimensional systems. Optical absorption imaging performed in these systems necessarily returns two-dimensional images of three-dimensional samples, integrated over the probe laser line-of-sight. Additionally, this integration for an ultracold gas corresponds to samples with very large optical densities, yielding *in situ* images which are difficult to interpret (to put it plainly, the images are pitch black). As a result, evidence for Mott shells was indirect (with the exception of the experiment of [65], which used a magnetic resonance imaging technique to obtain cuts through the in-situ profile). More recently, experiments were able to produce a two-dimensional gas in a square lattice. In this situation, integration perpendicular to the atomic plane is no longer an issue, and the shell structure could be directly imaged.

More sophisticated measurements have been performed by the Munich and Harvard groups who built what is now commonly known as “quantum gas microscope” [63, 64] (see also the experiment from the Chicago group [66]). These experiments are built around a microscope objective with very large numerical aperture (close to half-solid angle collection) which is corrected for aberrations. Those microscope operate at the diffraction limit, with optical resolution of a few hundred nm allowing to distinguish the optical signal from two adjacent sites with good contrast. In both experiments, the lattice depth is raised to a very large value prior to imaging, freezing the density distribution. The quantum gas is then made to emit fluorescence light by shining near-resonant light in an optical molasse configuration (the fluorescence periods are quite long, hundreds of ms, so that the optical molasses is necessary to prevent the atoms to “spill" out of the trap by heating). The fluorescence light is collected by the objective and imaged on a CCD camera. Figure 3.16 shows the experimental setup from the Munich group, as well as two images of a BEC in the square lattice. Each dot on the image is the fluorescence signal of a single atom, as collected by the imaging system[10]. The close-up shows clearly the regular arrangement of the trapping sites.

[10]Strictly speaking, this technique does not measure the atomic density. Indeed, in presence of near-resonant light atomic pairs trapped at

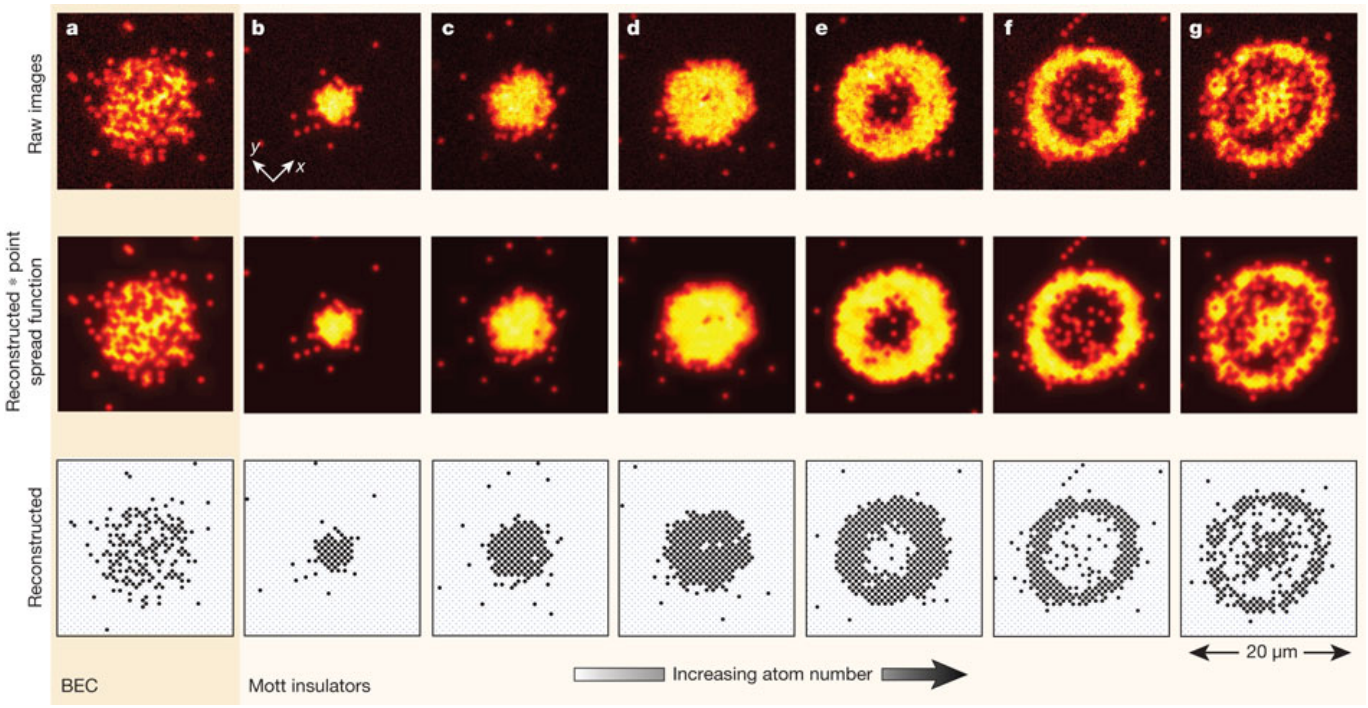

Figure 3.17.: In-situ images of a BEC and of Mott insulators [63]. The total atom number (or chemical potential, equivalently) increases from left to right. The lowest row shows a reconstructed map of the atom positions, obtained by deconvolution of the raw images to remove the effect of finite imaging resolution.

Figure 3.17 shows images of atomic clouds taken using this single-atom imaging technique, contrasting a BEC where density fluctuations are visible, to Mott insulator phases with $n_0 = 1$ atom per site. The images illustrate very clearly the formation of a plateau and demonstrate that a strongly correlated, incompressible phase has indeed been formed.

3.7.2. Thermodynamics of trapped Mott insulators

To understand better the results of quantum gas microscopy experiments, one needs to take into account the small, but finite temperature of the gas. The main features can be understood in the simple $J = 0$ limit, and it is sufficient to consider the uniform case to understand the trapped system in the local density approximation. The global partition function factorizes into a product of identical on-site partition functions $\mathcal{Z}_0$ determined by the on-site free energy $\mathcal{G}_i = \frac{U}{2}\hat{n}_i(\hat{n}_i - 1) - \mu\hat{n}_i$. From statistical mechanics, we find $\mathcal{Z}_0$ as

$$\mathcal{Z}_0 = \sum_{n_0} \exp\left(-\beta E(n_0)\right), \tag{3.101}$$

where $E(n_0) = \frac{U}{2}n_0(n_0 - 1) - \mu n_0$ and where $|n_0\rangle$ denotes a Fock state with n_0 atoms. At $T = 0$, the filling of each site is $n_0 = \mathrm{Int}[\mu/U] + 1$, where $\mathrm{Int}(x)$ returns the integer part of x. The points where $\mu = Un_0$ are special : the states $|n_0\rangle$ and $|n_0 + 1\rangle$ are degenerate, and there are many degenerate ground states corresponding to any superposition of the two Fock states (see Section 3.2.3).

At finite temperatures, other states than $|n_0\rangle$ can be thermally excited, with a probability given by the Boltzmann factor in Eq. (3.101). From Eq. (3.101) and from the standard thermodynamical relations (see Section 2.3.1), we calculate the on-site mean density,

$$\overline{n} = -\frac{\partial \mathcal{Z}_0}{\partial \mu} = \frac{1}{\mathcal{Z}_i}\sum_n n \exp\left[-\beta E(n)\right], \tag{3.102}$$

and the on-site density fluctuations ,

$$\Delta n^2 = \overline{n^2 - \overline{n}^2} = \frac{1}{\mathcal{Z}_0}\sum_n (n^2 - \overline{n}_i^2)\exp\left[-\beta E(n)\right]. \tag{3.103}$$

the same site of the lattice undergo very strong light-induced inelastic collisions, which result in the loss of the two atoms from the trap. As a result, only sites with one atom survive the imaging process. Sites initially containing an even number of atoms appear empty, and sites initially ontaining an odd number of atoms appear to have only one. The technique therefore measures the *parity* of the atom number at each site.

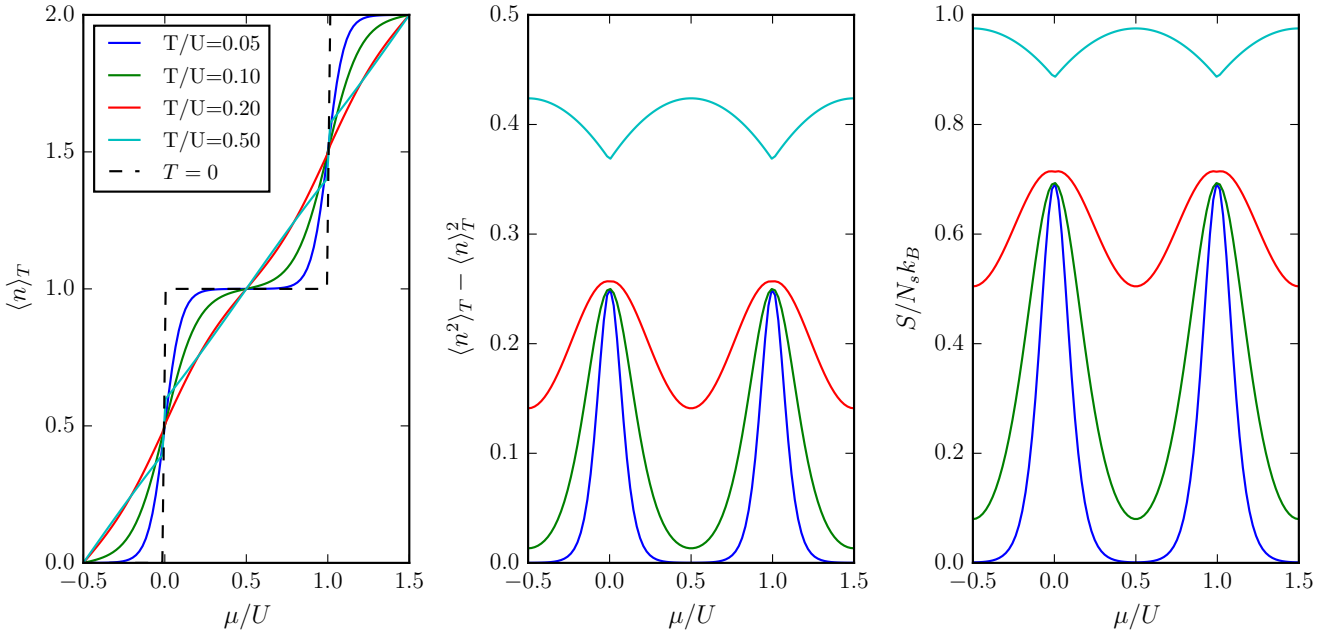

Figure 3.18.: Disappearance of Mott plateaux at finite temperatures. **a**: Average density, **b**: Density fluctuations, and **c**: entropy per site versus chemical potential.

At low enough temperatures, only the states n_0, $n_0 - 1$ and $n_0 + 1$ are important (just as in the $T = 0$ case discussed previously). The contribution from other Fock states is suppressed by a factor at least $\sim e^{-\beta U} \ll 1$ due to their higher interaction energy. By restricting the sums above to the three states only ("particle-hole approximation"), one obtains the analytical expressions for the mean density,

$$\overline{n}_i \approx n_0 + \frac{B(X,T)}{1 + A(X,T)}, \tag{3.104}$$

for the density fluctuations,

$$\Delta n_i^2 \approx \frac{4\exp(-\beta U) + A(X,T)}{[1 + A(X,T)]^2}. \tag{3.105}$$

We have defined the quantities

$$A(X,T) = 2\exp\left(-\frac{\beta U}{2}\right)\cosh(\beta U X), \tag{3.106}$$

$$B(X,T) = 2\exp\left(-\frac{\beta U}{2}\right)\sinh(\beta U X), \tag{3.107}$$

to try to keep the notation compact. We have also introduced the convenient variable $X = \mu/U - (n_0 - 1/2)$. At low temperatures $T < U$, as the chemical potential goes from the bottom to the top of each Mott "lobe", X varies between -1/2 and +1/2.

In Fig. 3.18, we show the density and fluctuations as a function of X, for the first Mott plateau ($n_0 = 1$) and various temperatures up to $T = U$. Finite temperature effects are clearly pronounced near the edges of a Mott plateau, where it is easier to reduce the free energy by creating supplementary particles or holes. A Mott-like region survives for all practical purposes up to $T = T^* \sim 0.2U$, where the Mott plateau has completely disappeared. One can see T^* as a kind of crossover temperature where the MI "melts" due to thermal fluctuations and transforms into an interacting thermal gas.

Fig. 3.19 shows experimental data from [63] where the average density and density fluctuations are plotted as a function of position in the trap. One can observe a clear correlation between "density plateaux" and supression of density fluctuations, a signature of an incompressible phase. The finite temperature, $J = 0$ theory that we have sketched above has been used to fit the experimental profiles with T a free parameter. This gives $k_B T \approx 0.05U$, confirming that the experimental system remains well below the "melting" temperature. Note that this estimation of temperature ascribes all imperfections (due *e.g* to imaging) to a finite temperature effect, and therefore provides an upper bound for the true temperature.

Fig. 3.18 also shows the distribution of entropy across the system. The entropy is computed from the standard thermodynamic formula. In the "particle-hole approximation", one finds

$$S/k_{\rm B} = \ln \mathcal{Z}_0 + \mu \bar{n}_i - \frac{1}{\beta}\frac{\partial \ln \mathcal{Z}_0}{\partial \beta} \tag{3.108}$$

$$\approx \ln\left[1 + A(X,T)\right] + \frac{1}{2\beta}\frac{A(X,T)}{1+A(X,T)} - \beta U X \frac{B(X,T)}{1+A(X,T)}, \tag{3.109}$$

which is plotted in Fig. 3.18. The plot shows how the entropy is concentrated in the regions with non-integer fillings interpolating between Mott plateaux. These regions would be be superfluid at $T = 0$, but the condensate fraction vanishes for temperatures $T \sim zJ$ [67, 68]. For higher temperatures, there is no condensate and the layers are formed by a normal Bose fluid. The reason for this spatial segregation of entropy is the excitation gap in the Mott region, leading to a finite excitation energy $\sim U$ to create particle- or hole-like excitations.

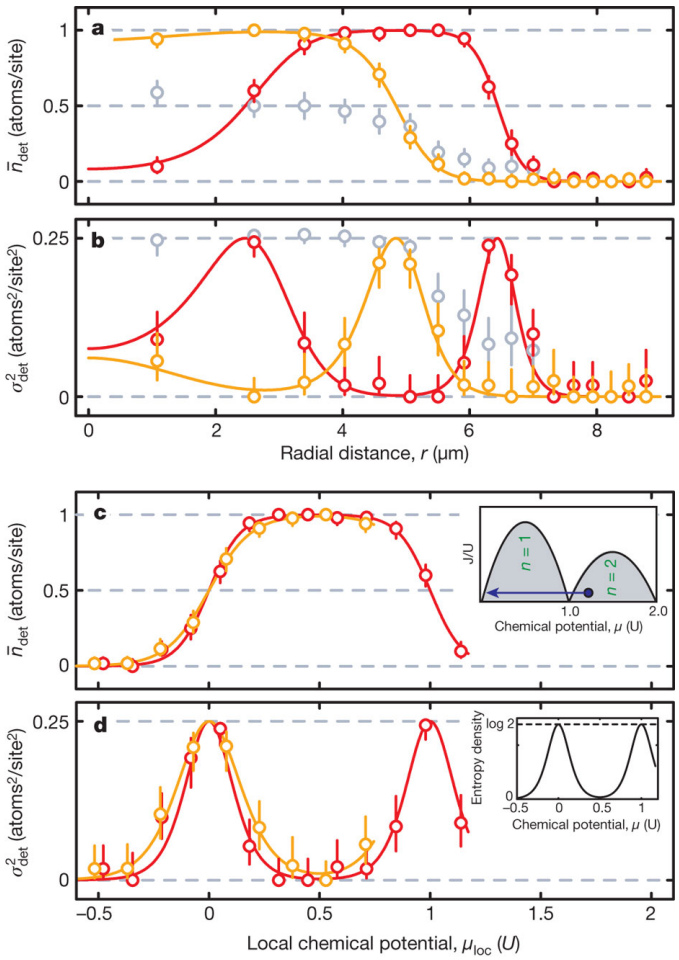

Figure 3.19.: Density (**a**, **c**) and density fluctuations (**c**, **d**) measured by [63]. The top two graphs ((**a**, **b**) are plotted versus distance from the center of the cloud for three different configurations: a condensate (pink symbols), a Mott insulator with $n_0 = 1$ (yellow symbols) and a Mott insulator with $n_0 = 1, 2$ (red symbols). In the last case, the $n_0 = 2$ core appears empty due to light-assisted collisions during the imaging process. The bottom two graphs ((**c**, **d**) show the same data versus local chemical potential. The concentration of fluctuations (hence, of entropy) in the layers between Mott plateaux is clearly seen. The lines are fit to the data using the $J = 0$ theory sketched in the notes, leading to temperatures $k_B T \lesssim 0.05 - 0.1\,U$.

4. The Fermionic Hubbard model : a short overview

We now turn to a short discussion of experiments involving fermionic atoms. As in the continuum case, interactions between two fermions in the same internal state are strongly suppressed at very low temperatures, due to the vanishing of the $s-$wave scattering amplitude. As a result, a single-component gas of fermions very much behaves as an ideal Fermi gas in a periodic potential, as described briefly in Chapter 2. For a gas of two-component fermions, $s-$wave scattering between fermions in different internal states is allowed and this will be the subject discussed in the present Chapter. Most experiments have been carried out with alkali atoms, ^{6}Li or ^{40}K. Two particular hyperfine states are selected, usually on the basis of their collisional stability and the availability of a convenient Feshbach resonance allowing to control the interaction between the two components. We will denote the two internal states as $\downarrow$ / $\uparrow$. There is a clear analogy with the modelling of electronic systems, with two possible spin states and the optical lattice playing the role of the periodic potential exerted by the crystal matrix hosting the electronic fluid. We note that recent experiments with different atoms are starting to probe new regimes with many spin components (*e.g.* 6 for Ytterbium 173, or even 10 for Strontium 87) and long-range dipole-dipole interactions (Chromium or Erbium).

4.1. Fermi-Hubbard Hamiltonian

4.1.1. Two-component fermions on a lattice

The basic single-band, tight-binding Hamiltonian for a two-component fermion gas in an optical lattice can be written in a very parallel way to what we have done for bosons. Introducing annihilation operators $\hat{c}_{i,\sigma}$ for a fermion in the Wannier state $W(\boldsymbol{r}-\boldsymbol{r}_i)$ and in the spin state σ, the fermionic Hubbard Hamiltonian reads

$$\mathcal{H}_{\mathrm{FH}} = -J\sum_{\langle i,j\rangle,\sigma}\hat{c}^\dagger_{i,\sigma}\hat{c}_{j,\sigma} + \frac{U}{2}\sum_i \hat{n}_{i,\uparrow}\hat{n}_{i,\downarrow}. \tag{4.1}$$

Here U corresponds to on-site interactions between $\downarrow-\uparrow$ fermions, usually tunable thanks to Feshbach resonances. In the following, we will present a qualitative description of (some) phenomena described by the Hamiltonian in Eq. (4.1). A more extensive discussion can be found in [69, 70].

4.1.2. From band to Mott insulator

We will discuss the Hubbard model in two limits specified by the filling factor, $\overline{n} = \frac{N\uparrow/\downarrow}{N}$. For unit filling (per spin state) $\overline{n}=1$, each spin component completely fills the available Hilbert space in the lowest band (recall there are N_s Bloch/Wannier states in each band). This corresponds to a band insulator, familiar from the theory of solids, where motion across the lattice is blocked because of the Pauli exclusion principle : An atom cannot tunnel to a neighbouring site (while staying in the lowest band) because it is necessarily occupied by an identical fermion. Any residual motion must involve higher Bloch bands, the description of which lies beyond our simple Hubbard model. These effects are typically weak for practical parameters, except perhaps very close to a Feshbach resonance [71].

A more complicated case corresponds to partial filling of the lowest band, for instance in the half-filling case $\overline{n}=1/2$. In this case, one expects for $U=0$ that each spin component forms a "metallic" state, where all $N_s/2$ states lowest Bloch states are occupied, and all others are empty. In 1D, for instance, the dispersion relation in the tight-binding limit is $\varepsilon(q) = -2J\cos(qd)$ and the first Brillouin zone is $]-k_L, k_L]$. A half-filled band corresponds to all states with quasimomentum $|q|\leq k_L/2$ occupied, and a Fermi energy $E_F = 0$(note that the bottom of the band is at energy $-2J$). The Fermi surface remains sharply defined until a temperature $k_BT \sim zJ$, where it becomes increasingly smeared by thermal fluctuations. For higher temperatures ($zJ \ll k_BT \ll \Delta$, with Δ the gap to the first excited band), the Fermi gas slowly turns to a Boltzmann gas uniformly filling the lowest band. In the metallic regime, nothing prevents double occupancy of a lattice site by two fermions with opposite spin. Close to half-filling and for $U \ll J$, fluctuations creating an empty site and a doubly-occupied one are thus likely for non-(or weakly-) interacting quasi-particles.

Increasing the interaction U (taken here to be repulsive, $U>0$, as for bosons), there will be an increased energy cost to pay for double occupancy. We can easily understand that a similar phenomenon as seen for bosons will take place, namely a suppression of such doubly occupied sites as repulsive interactions take over. This entails a suppression of on-site number fluctuations and the formation of a Mott insulator. This should be distinguished from the band insulator arising at unit filling: In the former case, the suppression of "metallic" behaviour is due to intercomponent interactions and in the latter to the Pauli principle.

The phenomenology of the Mott transition is similar to what we have seen for single-component bosons : suppression of mass transport, opening of an excitation gap, vanishing of the compressibility, suppression of double occupancy $\uparrow/\downarrow$ at the same lattice site with increasing U/J. There is however one major difference due to the additional spin degree of freedom. In a Mott insulator, number fluctuations are suppressed, implying that only configurations with one atom per site on average survive. For a lattice with N_s sites (and half-filling), the number of possible (almost) degenerate configurations is huge ($\sim 2^{N_s}$) because of the spin degeneracy. As we will see next, this degeneracy is lifted at low enough temperatures by an effective spin-spin interaction (the so-called superexchange mechanism)[1].

This effective spin-spin interaction leads to a phase transition to a magnetically ordered state (see Section 4.2.2), which masks the metal-Mott insulator phase transition that could be expected in analogy with the Bose-Hubbard model. For temperatures high enough to "avoid" the magnetic phase transition, one has in fact a smooth crossover from a spin-disordered metal to a spin-disordered insulator, without sharp changes as expected in the proximity of a true phase transition.

Experimental evidence for fermionic Mott insulators were obtained in 2008 [72, 73]. One experiment [72] used the double occupancy (averaged over the whole lattice) as observable. A drastic reduction for large interaction strengths was observed and further interpreted as evidence for a strongly correlated phase. The second experiment [73] measured the so-called "global compressibility", *i.e.* the change in the radius of the cloud with increasing confinement. In a Mott insulator, the density is fixed and the cloud radius remains constant when changing the external confinement (until the added potential energy becomes on the order of U, which triggers the formation of another shell for bosons, or of a band insulator for fermions).

More recently, quantum gas microscopes were demonstrated for fermionic atoms [74, 75, 76, 77, 78, 79]. The molasse cooling is problematic for fermionic Li and K, the atomic species that have been observed, making these experiments even more challenging than for bosons. Figure 4.1 shows an example taken from [79], where the unit-density plateaux are clearly observed.

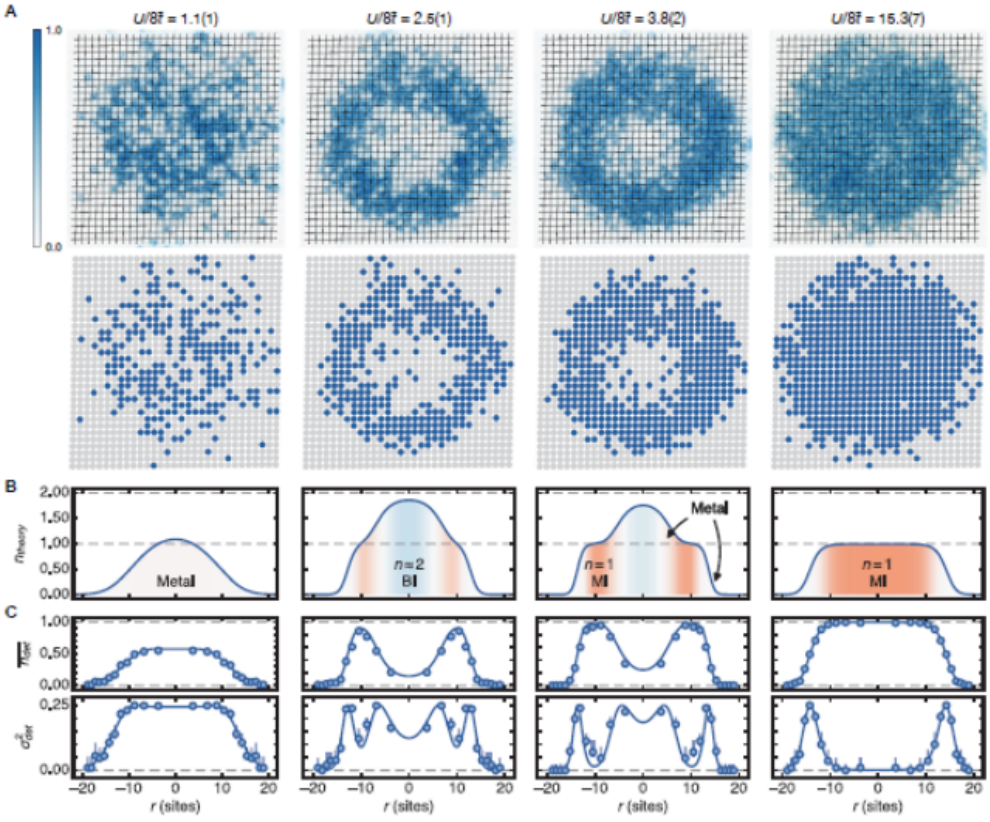

Figure 4.1.: In-trap fluorescence images of a two-component Fermi gas in the Mott insulator regime taken using a quantum gas microscope. The cuts show the mean observed density (top row), the on-site density fluctuations (middle row) and a reconstructed profile showing the positions of the atoms before imaging (bottom row).

[1] Note that a similar discussion applies to bosons with multiple internal states, as opposed to the single-component case discussed in Chapter 2.

4.2. Magnetism in the deep Mott regime

4.2.1. Toy model: two fermions in two wells

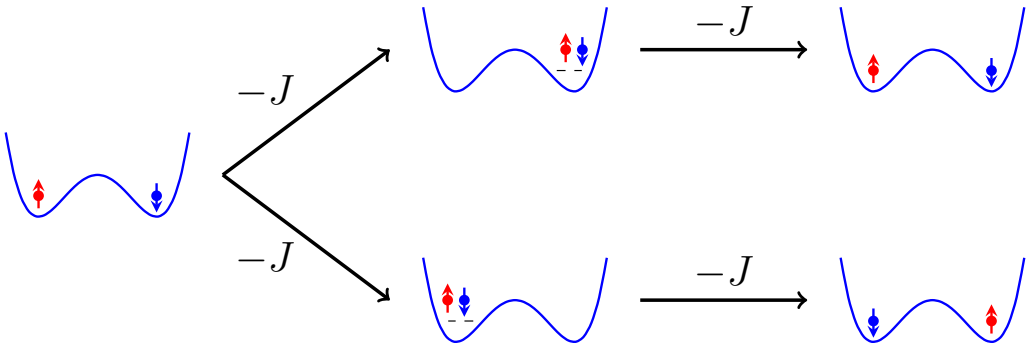

Figure 4.2.: Superexchange for two fermions in a double-well potential.

In order to set the stage for discussing the low-temperature magnetic properties in the Mott regime, we first consider a toy model with only two fermions (one in each spin component) in a double-well potential. At low energies, the double-well potential has two low-lying energy eigenstates, analogous to the Bloch states in a lattice. One can form symmetric or antisymmetric superpositions, which are well localized in the left or in the right well and are analogous to the Wannier states. We denote by $\phi_{L/R}$ these localized states. The single-particle Hamiltonian is not diagonal in this basis, with a tunneling matrix element J. If we also account for on-site repulsion between unlike fermions, with matrix element U, we arrive at a simplified Hubbard Hamiltonian

$$\mathcal{H}_{2\mathrm{w}} = -J \sum_{\sigma} \left(\hat{c}^{\dagger}_{L,\sigma} \hat{c}_{R,\sigma} + \mathrm{h.c.} \right) + \frac{U}{2} \sum_{i} \hat{n}_{L,\uparrow} \hat{n}_{R,\downarrow}. \tag{4.2}$$

This problem is simple enough to be solved exactly (see Appendix E). The Hilbert space for one $\uparrow$ and one $\downarrow$ fermion is spanned by four states. Without tunneling, two of them correspond to singly-occupied states,

$$\mathcal{E}_1 = \{|L\uparrow, R\downarrow\rangle, |L\downarrow, R\uparrow\rangle\}, \qquad |1\rangle = |L\uparrow, R\downarrow\rangle = \hat{c}^{\dagger}_{L,\uparrow}\hat{c}^{\dagger}_{R,\downarrow}|\varnothing\rangle, \qquad |2\rangle = |L\downarrow, R\uparrow\rangle = \hat{c}^{\dagger}_{L,\downarrow}\hat{c}^{\dagger}_{R,\uparrow}|\varnothing\rangle,$$

with energy zero. The other two states correspond to a high-energy subspace where both fermions are in the same well,

$$\mathcal{E}_2 = \{|L\uparrow, L\downarrow\rangle, |R\uparrow, R\downarrow\rangle\}, \qquad |3\rangle = |L\uparrow, L\downarrow\rangle = \hat{c}^{\dagger}_{L,\uparrow}\hat{c}^{\dagger}_{L,\downarrow}|\varnothing\rangle, \qquad |4\rangle = |R\uparrow, R\downarrow\rangle = \hat{c}^{\dagger}_{R,\uparrow}\hat{c}^{\dagger}_{R,\downarrow}|\varnothing\rangle,$$

with interaction energy U. Taking tunneling into account, the eigenvalues become $E_-, 0, U, E_+$ in ascending order, with

$$E_{\pm} = \frac{U}{2} \pm \frac{1}{2}\sqrt{U^2 + 16J^2}. \tag{4.3}$$

For $U \gg J$, the eigenstates therefore remain grouped into a low-energy subspace with energy ~ 0 and a high-energy subspace with energy $\sim U$. The eigenvectors in the low-energy sector are given by

$$|s'\rangle \approx \frac{1}{\sqrt{2}} \left(|L\uparrow, R\downarrow\rangle - |L\downarrow, R\uparrow\rangle \right) + \mathcal{O}\left(\frac{J}{U}\right), \tag{4.4}$$

$$|t_0\rangle = \frac{1}{\sqrt{2}} \left(|L\uparrow, R\downarrow\rangle + |L\downarrow, R\uparrow\rangle \right). \tag{4.5}$$

The first state with energy $\approx -4J^2/U$ corresponds to a spin singlet (with a small admixture of the doubly-occupied state $|I_+\rangle$). The second with energy 0 corresponds to a spin triplet state[2]. The lower energy of the singlet state corresponds to an effective spin-exchange interaction favouring the singlet state.

The behavior for large U can be obtained from another point-of-view, the so-called *effective Hamiltonian* technique. In this point of view, one is interested only in the low-energy subspace $\mathcal{E}_1$ with one fermion per site. The bare matrix elments of the tunneling operator vanish within this subspace. Tunneling couples to higher-energy states (doubly occupied), such that coupling between the two wells arise from second-order processes, where a first atom tunnels to a nearby site and a second atom (possibly the same) tunnels to fill the empty site. This is shown graphically in

[2] There are of course two other triplet states in the subspace with single occupancy, $|t_+\rangle = |L\uparrow, R\uparrow$ and $|t_-\rangle = |L\downarrow, R\downarrow\rangle$. They have zero interaction energy and zero tunneling energy (Pauli blocking) and are therefore degenerate with $|t_0\rangle$.

Figure 4.2, where one can see two possibles final states, either identical to the initial one or with a change of spin states. The latter corresponds to a spin-exchange process. Note that the intermediate, doubly-occupied state is only a virtual one. The effective Hamiltonian approach allows to describe these second-order processes. Using the formulation of Appendix F, the matrix elements in the singly-occupied subspace $\mathcal{E}_1$ are given by

$$\hat{H}_{\text{eff}} = \begin{pmatrix} -\frac{2J^2}{U} & \frac{2J^2}{U} \\ \frac{2J^2}{U} & -\frac{2J^2}{U} \end{pmatrix}. \tag{4.6}$$

We rewrite this in second quantized form (to facilitate extension to the full Hubbard model),

$$\hat{H}_{\text{eff}} = -\frac{J^2}{U}\left(\hat{c}^\dagger_{L\uparrow}\hat{c}^\dagger_{R\downarrow}\hat{c}_{R\downarrow}\hat{c}_{L\uparrow} + \hat{c}^\dagger_{L\downarrow}\hat{c}^\dagger_{R\uparrow}\hat{c}_{R\uparrow}\hat{c}_{L\downarrow} - \hat{c}^\dagger_{L\uparrow}\hat{c}^\dagger_{R\downarrow}\hat{c}_{R\uparrow}\hat{c}_{L\downarrow} - \hat{c}^\dagger_{L\downarrow}\hat{c}^\dagger_{R\uparrow}\hat{c}_{R\downarrow}\hat{c}_{L\uparrow}\right) \tag{4.7}$$

$$= \frac{J^2}{U}\left(-\hat{n}_{L\uparrow}\hat{n}_{R\downarrow} - \hat{n}_{L\downarrow}\hat{n}_{R\uparrow} + \hat{c}^\dagger_{L\uparrow}\hat{c}_{L\downarrow}\hat{c}^\dagger_{R\downarrow}\hat{c}_{R\uparrow} + \hat{c}^\dagger_{L\downarrow}\hat{c}_{L\uparrow}\hat{c}^\dagger_{R\uparrow}\hat{c}_{R\downarrow}\right) \tag{4.8}$$

We introduce a spin 1/2 operator for the left well, $\hat{\boldsymbol{S}}_L$, which is defined by its standard components

$$\hat{S}_{z,L} = \frac{1}{2}\left(\hat{n}_{L\uparrow} - \hat{n}_{L\downarrow}\right), \qquad \hat{S}_{+,L} = \hat{c}^\dagger_{L\uparrow}\hat{c}_{L\downarrow}, \qquad \hat{S}_{-,L} = \hat{c}^\dagger_{L\downarrow}\hat{c}_{L\uparrow}, \tag{4.9}$$

and similarly for the right well. This allows us to rewrite the effective Hamiltonian as

$$\hat{H}_{\text{eff}} = \frac{J^2}{U}\left(\hat{\boldsymbol{S}}_L \cdot \hat{\boldsymbol{S}}_R - \frac{1}{4}\right). \tag{4.10}$$

We therefore recover the result obtained from the exact solution : an effective, isotropic Heisenberg spin-spin interaction ("superexchange") mediated by virtual tunneling processes to doubly occupied sites. The coupling is antiferromagnetic, *i.e.* the energy is minimized by making neighboring spins antiparallel, and the exchange constant J_{ex} scales as J^2/U.

4.2.2. Antiferromagnetism and Néel ordering

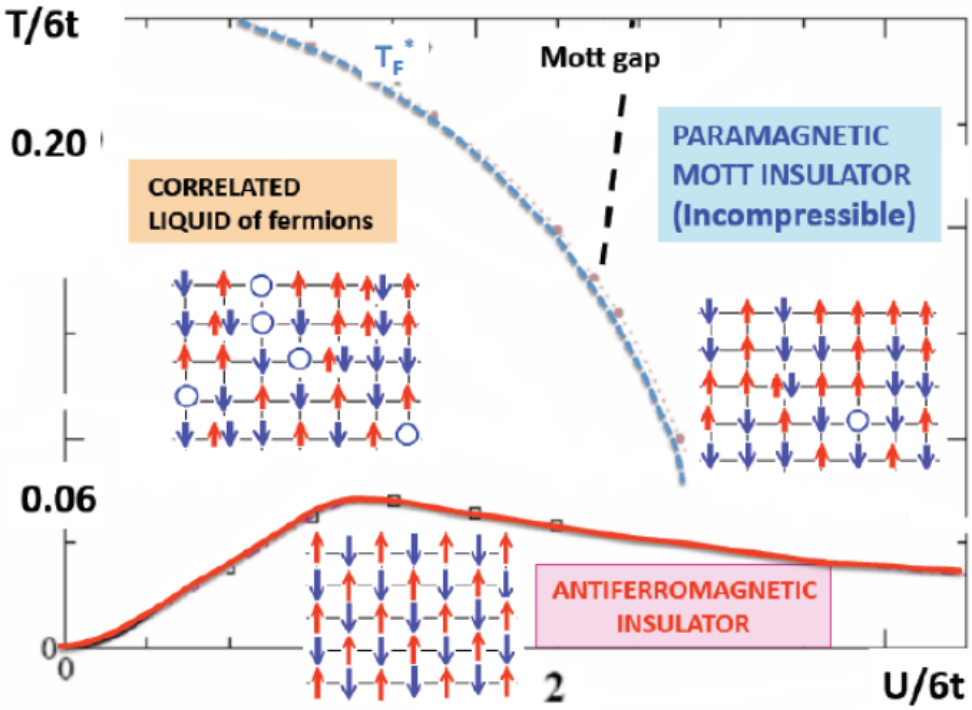

Figure 4.3.: Phase diagram of the uniform fermionic Hubbard model at half-filling (from [70]).

A similar reasoning can be applied to the Hubbard model for fermions in an extended lattice, and in the Mott insulator regime where $U \gg J$. The effective Hamiltonian remains an Heisenberg spin Hamiltonian

$$\mathcal{H}_{\text{FH}} \underset{\text{Mott } U \gg J}{\longrightarrow} \mathcal{H}_{\text{Heisenberg}} = J_{\text{ex}} \sum_{\langle i,j\rangle,\sigma}\left(\hat{\boldsymbol{S}}_i \cdot \hat{\boldsymbol{S}}_j - \frac{1}{4}\hat{n}_i\hat{n}_j\right), \tag{4.11}$$

with antiferromagnetic coupling $J_{\text{ex}} = \frac{4J^2}{U} > 0$ between nearest neighbors. On bipartite lattices, which can be partitioned on two equivalent sublattices A and B (among them, the square and cubic lattices), the ground state of this Heisenberg model is an antiferromagnetic state with *Néel order* [80]: all the spins belonging to a given A or B are aligned but the spin of the two sublattices are oppositely oriented.

A phase diagram in the interaction-temperature plane is shown in Figure 4.3. Coming from high temperatures, a phase transition to a state with Néel order is found at a temperature $T_{\text{Néel}}$ where magnetic order sets in. For large U, this temperature is on the order of the superexchange coupling,

$$T_{\text{Néel}} \sim J_{\text{ex}} = \frac{4J^2}{U}. \tag{4.12}$$

For intermediate values of U, numerical calculations have found a maximum for intermediate coupling, as shown in the figure (see [69, 70] for more details).

There has been very impressive progress in the last few years to obtain colder and colder systems of fermions, and to obtain evidence for antiferromagnetic ordering. Quantum gas microscopes proved extremely useful (though not strictly necessary). The longitudinal spin density $s_z(\boldsymbol{r}_i) = n_\uparrow(\boldsymbol{r}_i) - n_\downarrow(\boldsymbol{r}_i)$ is measured by selectively imaging each of the spin component and taking the difference of the two images. Each individual realization of the system provides a snapshot of the distribution $s_z(\boldsymbol{r}_i)$. Averaging over many such realizations, one can reconstruct many observables such as the average density, $\langle n(\boldsymbol{r}_i)\rangle$, spin density, $\langle s_z(\boldsymbol{r}_i)\rangle$, and density correlations, $\langle s_z(\boldsymbol{r}_i)s_z(\boldsymbol{r}_j)\rangle$[3].

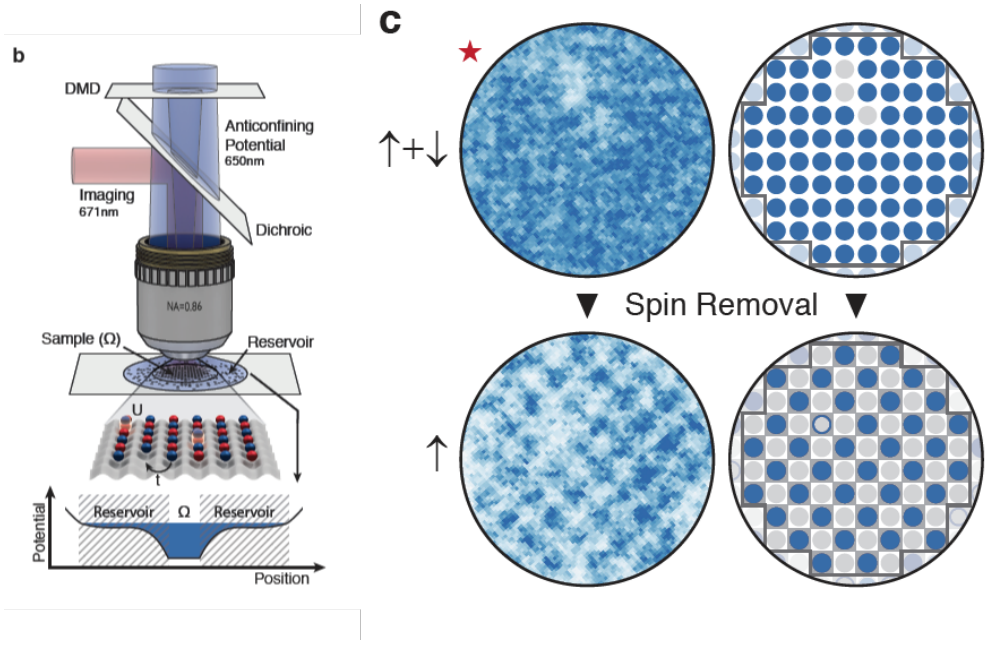

Figure 4.4.: Experimental setup (left picture), and principle for spin-resolved quantum gas microscopy (right picture) in [81]. The image showing the density of spin ↑ atoms clearly displays a checkerboard pattern characteristic of antiferromagnetism.

Short-range antiferromagnetic correlations have been reported by many groups [82, 83, 84, 85, 86]. Here "short-range" essentially means "nearest-neighbors": The correlation function $\langle s_z(\boldsymbol{r}_i)s_z(\boldsymbol{r}_j)\rangle$ is found to decay very rapidly with distance $|\boldsymbol{r}_i - \boldsymbol{r}_j|$. This corresponds to a temperature regime below U, but above the Néel temperature.

In a very recent experiment, this temperature limit has been overcome and antiferromagnetic long-range order has been observed in 2D [81] (see also [87]). Here a key advance was made by using the spatial segregation of entropy already encountered for bosons (see Fig. 4.4). By tailoring the trapping potential using advanced optical techniques, the authors were able to create extended regions (a few tens of lattice sites wide) with nearly uniform density and low entropy per site. This potential engineering essentially results in shuffling all the entropy towards the edges of the trap, far away from the region where measurements are performed, thereby allowing to uncover low-temperature (or equivalently, low-entropy) physics. This technique allowed them to prepare a two-component Fermi-Hubbard system below the Néel temperature, and to observe the long-range spin correlations across the whole system (see right panel in Fig. 4.4).

[3] In reality, things are slightly complicated by the fact that quantum gas microscopes measure the parity of the on-site occupation numbers, and not the occupation numbers directly, but the general principle is the same.

A. Time of flight experiments

Neglecting interactions during expansion, a time-of-flight (t.o.f.) picture reflects the initial momentum distribution of the trapped cloud. To show this statement, we express the initial wave function before release (say ψ_0) in the momentum basis,

$$\psi_0(\boldsymbol{r}, t=0) = \int \frac{d^3\boldsymbol{k}}{(2\pi)^{3/2}} \tilde{\psi}_0(\boldsymbol{k}) e^{i\boldsymbol{k}\cdot\boldsymbol{r}}. \tag{A.1}$$

with $\tilde{\psi}(\boldsymbol{k})$ the Fourier transform of ψ. Evolution during t.o.f. is due to a free particle Hamiltonian, leading to

$$\psi(\boldsymbol{r}, t) = \int \frac{d^3\boldsymbol{k}}{(2\pi)^{3/2}} \tilde{\psi}_0(\boldsymbol{k}) e^{i\left(\boldsymbol{k}\cdot\boldsymbol{r} - \frac{\hbar\boldsymbol{k}^2 t}{2m_a}\right)} \tag{A.2}$$

For long enough times, the phase factor determines the integral. It oscillates very rapidly, thus averaging the integral to zero, except near the points of stationary phase $k_i = m_a r_i/\hbar t$ ($r_i = x, y, z$). A stationary phase approximation (see Appendix B) yields

$$\psi(\boldsymbol{r}, t) \approx \tilde{\psi}_0\left(\boldsymbol{k} = \frac{m_a\boldsymbol{r}}{\hbar t}\right) e^{i\frac{m_a\boldsymbol{r}^2}{2\hbar t}} \int \frac{d^3\boldsymbol{r}}{(2\pi)^{3/2}} e^{-i\frac{\hbar\delta\boldsymbol{k}^2 t}{2m_a}} = \left(\frac{m_a}{i\hbar t}\right)^{3/2} \tilde{\psi}_0\left(\boldsymbol{k} = \frac{m_a\boldsymbol{r}}{\hbar t}\right) e^{i\frac{m_a\boldsymbol{r}^2}{2\hbar t}}. \tag{A.3}$$

This result becomes exact as $t \to \infty$, where the integral over the oscillating exponential tends to a δ function.

B. The method of stationary phase

Given an integral of the form

$$I = \int_a^b dx f(x) e^{i\phi(x)}, \tag{B.1}$$

where ϕ varies rapidly in the interval $[a, b]$ and f varies slowly, one expands the phase around the stationary phase points x_ν where $d\phi/dx = 0$,

$$\phi(x) \approx \sum_\nu \phi(x_\nu) + \frac{1}{2}\phi''(x_\nu)(x - x_\nu)^2 + \cdots, \tag{B.2}$$

and set $f(x) \approx f(x_\nu)$ in the integrand. Then one breaks up the integral into several pieces around each of the x_ν, and extend the integration bounds to $\pm\infty$ for each piece (this gives a good approximation since the fast oscillations average out the contributions far from the stationary points). This gives

$$I \approx \sum_\nu f(x_\nu) e^{i\sum_\nu \phi(x_\nu)} \int_{-\infty}^{+\infty} dx e^{i\frac{1}{2}\phi''(x_\nu)(x-x_\nu)^2} \tag{B.3}$$

$$= \sum_\nu f(x_\nu) e^{i\sum_\nu \phi(x_\nu)} \sqrt{\frac{2\pi}{|\phi''(x_\nu)|}} e^{i\arg[\phi''(x_\nu)] - i\frac{\pi}{4}}. \tag{B.4}$$

The Gaussian integral is calculated using contour integration. This method can be generalized to more than 1 dimension ("saddle-point integration").

C. Quantum adiabatic theorem

We consider a slowly evolving quantum system. The Hamiltonian admits for every time an eigenbasis written as

$$H(t)|\phi_n(t)\rangle = E_n(t)|\phi_n(t)\rangle. \tag{C.1}$$

The time-dependent wave function can be expanded in this instantaneous basis,

$$|\Psi(t)\rangle = \sum_n a_n(t) e^{-\frac{i}{\hbar}\int_0^t \varepsilon_n(t')dt'} |\phi_n(t)\rangle, \tag{C.2}$$

with the initial condition $a_n(0) = \delta_{n,n_0}$. The adiabatic theorem states that for arbitrarily slow evolution *and in the absence of level crossings*, $a_n(t) \to \delta_{n,n_0}$ (note that this is an asymptotic behavior, and that for finite speeds one expects corrections to the adiabatic following).

Substituting the expansion (C.2) into the Schrödinger equation, one finds (omitting the time dependence to make the notations lighter),

$$\dot{a}_n = -\langle\phi_n|\dot{\phi}_n\rangle - \sum_{m\ neqn} \langle\phi_n|\dot{\phi}_m\rangle e^{-\frac{i}{\hbar}\int_0^t (\varepsilon_m-\varepsilon_n)dt'} a_m. \tag{C.3}$$

We rewrite the term with $m = n$ as $\langle\phi_n|\dot{\phi}_n\rangle = i\gamma_n$. This term is purely imaginary: $d\langle\phi_n|\phi_n\rangle/dt = 0 = \langle\dot{\phi}_n|\phi_n\rangle + \langle\phi_n|\dot{\phi}_n\rangle$, so that γ_n is real. This term gives rise to the famous Berry phase for cyclic evolutions. The terms with $m \neq n$ can be rewritten using the relation (true only for $m \neq n$),

$$\frac{d}{dt}\langle\phi_n|H(t)|\phi_m\rangle = 0 = \Big(\varepsilon_n - \varepsilon_m\Big)\langle\phi_n|\dot{\phi}_m\rangle + \langle\phi_n|\dot{H}|\phi_m\rangle,$$

where the conservation of the scalar product $\frac{d}{dt}\langle\phi_n|\phi_m\rangle = 0$ has been used. This gives

$$\langle\phi_n|\dot{\phi}_m\rangle = \frac{\langle\phi_n|\dot{H}|\phi_m\rangle}{\varepsilon_m - \varepsilon_n}$$

for $m \neq n$. We then arrive at the following equation governing the time dependence of the band amplitudes,

$$\dot{a}_n = -i\gamma_n a_n - \sum_{m\neq n} \frac{\langle\phi_n|\dot{H}|\phi_m\rangle}{\varepsilon_m - \varepsilon_n} e^{-\frac{i}{\hbar}\int_0^t (\varepsilon_m-\varepsilon_n)dt'} a_m. \tag{C.4}$$

This is the typical structure for adiabatic problems.

Without solving Eq. C.4) explicitly, we can give an approximate adiabaticity criterion using time-dependent perturbation theory. We require that the rate of change of the amplitude due to non-adiabatic projection is much smaller than the one corresponding to free evolution (set by the Bohr frequencies $(\varepsilon_m - \varepsilon_n)/\hbar$). This leads to

$$\Big|\langle\phi_n|\dot{H}|\phi_m\rangle\Big| \ll \frac{\Big(\varepsilon_m - \varepsilon_n\Big)^2}{\hbar}. \tag{C.5}$$

This leads to our final statement for the adiabatic approximation,

$$a_n(t) \approx a_n(0) e^{-i\gamma_n t} + \mathcal{O}(\epsilon), \tag{C.6}$$

$$\epsilon = \frac{\hbar|\langle\phi_n|\dot{H}||}{(\varepsilon_m - \varepsilon_n)^2}. \tag{C.7}$$

with $\epsilon \ll 1$. The book by Albert Messiah contains a more detailed discussion, and we refer the reader to it for more details [20].

D. Derivation of Bose-Hubbard Hamiltonian

In this Appendix, we discuss in more details the derivation of the Bose-Hubbard Hamiltonian. Using the expansion of the field operator, $\hat{\Psi}(\mathbf{r}) = \sum_i W(\boldsymbol{r} - \boldsymbol{r}_i)\hat{a}_i$ in the interaction term in Eq. (3.1), one finds

$$\hat{H}_{\text{int}} = \frac{1}{2}\sum_{ijkl} U_{ijkl}\hat{a}_i^\dagger \hat{a}_j^\dagger \hat{a}_k \hat{a}_l \tag{D.1}$$

The interaction matrix elements are given by the expression

$$U_{ijkl} = g\int d\mathbf{r}\; W^*(\boldsymbol{r} - \boldsymbol{r}_i)W^*(\boldsymbol{r} - \boldsymbol{r}_j)W(\boldsymbol{r} - \boldsymbol{r}_k)W(\boldsymbol{r} - \boldsymbol{r}_l) \tag{D.2}$$

involving the overlap between multiple Wannier functions. Because the Wannier functions are by construction well-localized around the lattice sites, the interaction term is strongly dominated by the term with $i = j = k = l$ in Eq.(D.1), where the overlap between all Wannier functions is maximal (matrix element $U = U_{iiii}$). The next leading terms correspond to the ones where one of the Wannier functions is located one lattice site away (matrix element $V = U_{iiij}$ with i and j nearest-neighbours), followed by terms where one Wannier function is two lattice sites away (matrix element $W' = U_{iiij}$ with i and j next-nearest-neighbours) and where two Wannier functions are one lattice site away (matrix element $W = U_{iijj}$ with i and j nearest-neighbours), etc ... We rewrite the sum to reflect this hierarchy, listing terms of decreasing magnitude

$$\hat{H}_{\text{int}} = \frac{1}{2}\sum_i U\hat{a}_i^\dagger\hat{a}_i^\dagger\hat{a}_i\hat{a}_i \tag{D.3}$$

$$+\sum_{\langle i,j\rangle} V\underbrace{\hat{a}_i^\dagger\hat{a}_i^\dagger\hat{a}_i\hat{a}_j}_{\hat{a}_i^\dagger\hat{n}_i\hat{a}_j} + \text{h.c.} \tag{D.4}$$

$$+\sum_{\langle\langle i,j\rangle\rangle} W'\underbrace{\hat{a}_i^\dagger\hat{a}_i^\dagger\hat{a}_i\hat{a}_j}_{\hat{a}_i^\dagger\hat{n}_i\hat{a}_j} + \text{h.c.} + \frac{1}{2}\sum_{\langle i,j\rangle} W\left[\left(\hat{a}_i^\dagger\right)^2(\hat{a}_j)^2 + \underbrace{\hat{a}_i^\dagger\hat{a}_i\hat{a}_j^\dagger\hat{a}_j}_{\hat{n}_i\hat{n}_j} + \text{h.c.}\right] \tag{D.5}$$

$$+\cdots, \tag{D.6}$$

where other terms involving more than two different sites were discarded. The first term $\propto U$ on the right hand side of Eq.(D.3) is the dominant on-site interaction, which is purely local. The term on the second line $\propto V$ gives the first correction $\propto \hat{a}_i^\dagger\hat{n}_i\hat{a}_j$, which represent an *interaction-induced* tunneling event from site i to a nearest neighbour j with a density-dependent tunneling amplitude (similarly for the first term on the third line $\propto W'$). The last term on the third line $\propto W$ involves two types of interactions, a first one $\propto \hat{n}_i\hat{n}_j$ describing off-site interactions between nearest neighbors and a second one $\propto \left(\hat{a}_i^\dagger\right)^2(\hat{a}_j)^2$ called *co-tunneling*, which describes a correlated event where two particles tunnel simultaneously and is purely due to interactions.

Figure D.1 shows the magnitude of U, V, W, W' and of the single particle tunneling energy J for different lattice depths. One concludes from this plot that the two energy scales U and J are dominant in the domain of validity of the Bose-Hubbard model, and that the interaction Hamiltonian is safely approximated by keeping only the on-site term. The first correction to consider is in the form of density-induced tunneling terms.

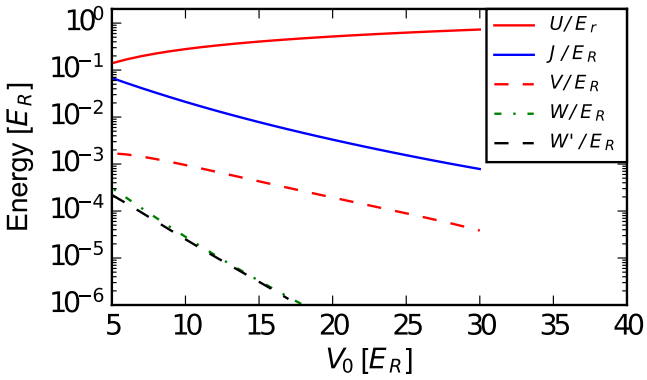

Figure D.1.: Interaction parameters U, V, W, W' for the Bose-Hubbard model. Also shown in the single-particle tunneling energy J. The interaction strength was chosen to match the one for ^{87}Rb atoms [scattering length $a_s \approx 5.5\,\mathrm{nm}$] in a $\lambda_L = 820\,\mathrm{nm}$ lattice.

E. Solution of the problem of two fermions in two wells

We give in this Appendix the solution for the problem of two fermions in two wells, described by the Hubbard Hamiltonian (4.2),

$$\mathcal{H}_{2\mathrm{w}} = -J\sum_{\sigma}\left(\hat{c}^{\dagger}_{L,\sigma}\hat{c}_{R,\sigma} + \mathrm{h.c.}\right) + \frac{U}{2}\sum_{i}\hat{n}_{L,\uparrow}\hat{n}_{R,\downarrow}. \tag{E.1}$$

The Hilbert space is spanned by only four states,

$$\begin{aligned}
&\mathcal{E}_1 = \{|L\uparrow, R\downarrow\rangle, |L\downarrow, R\uparrow\rangle\}, \quad |1\rangle = |L\uparrow, R\downarrow\rangle = \hat{c}^{\dagger}_{L,\uparrow}\hat{c}^{\dagger}_{R,\downarrow}|\varnothing\rangle, \quad |2\rangle = |L\downarrow, R\uparrow\rangle = \hat{c}^{\dagger}_{L,\downarrow}\hat{c}^{\dagger}_{R,\uparrow}|\varnothing\rangle, \quad \text{energy } 0,\\
&\mathcal{E}_2 = \{|L\uparrow, L\downarrow\rangle, |R\uparrow, R\downarrow\rangle\}, \quad |3\rangle = |L\uparrow, L\downarrow\rangle = \hat{c}^{\dagger}_{L,\uparrow}\hat{c}^{\dagger}_{L,\downarrow}|\varnothing\rangle, \quad |4\rangle = |R\uparrow, R\downarrow\rangle = \hat{c}^{\dagger}_{R,\uparrow}\hat{c}^{\dagger}_{R,\downarrow}|\varnothing\rangle, \quad \text{energy } U.
\end{aligned}$$

Denoting $\hat{T} = \sum_{\sigma}\hat{a}^{\dagger}_{L,\sigma}\hat{a}_{R,\sigma} + \mathrm{h.c.}$, we have[1]

$$\hat{T}|1\rangle = |3\rangle + |4\rangle, \quad \hat{T}|2\rangle = |3\rangle - |4\rangle, \quad \hat{T}|3\rangle = |1\rangle - |2\rangle, \quad \hat{T}|4\rangle = |1\rangle - |2\rangle.$$

We rewrite the Hamiltonian in matrix form in the $\{|1\rangle, |2\rangle, |3\rangle, |4\rangle\}$ basis,

$$\mathcal{H}_{2\mathrm{w}} = \left(\begin{array}{cc|cc} 0 & 0 & J & J \\ 0 & 0 & -J & -J \\ \hline J & -J & U & 0 \\ J & -J & 0 & U \end{array}\right) \tag{E.2}$$

To diagonalize this Hamiltonian, we introduce the linear superpositions

$$|s\rangle = \frac{1}{\sqrt{2}}\left(|L\uparrow, R\downarrow\rangle - |L\downarrow, R\uparrow\rangle\right), \tag{E.3}$$

$$|t_0\rangle = \frac{1}{\sqrt{2}}\left(|L\uparrow, R\downarrow\rangle + |L\downarrow, R\uparrow\rangle\right), \tag{E.4}$$

$$|I_{\pm}\rangle = \frac{1}{\sqrt{2}}\left(|L\uparrow, L\downarrow\rangle \pm |R\uparrow, R\downarrow\rangle\right). \tag{E.5}$$

One can check that $|t_0\rangle, |I_-\rangle$ are eigenstates of $\mathcal{H}_{2\mathrm{w}}$ with eigenvalues $0, U$, respectively. The other two eigenstates are found as superpositions of $|s\rangle, |I_+\rangle$. They diagonalize the restricted Hamiltonian matrix

$$\left(\begin{array}{cc} 0 & -2J \\ -2J & U \end{array}\right). \tag{E.6}$$

The eigenvalues are

$$E_{\pm} = \frac{U}{2} \pm \frac{1}{2}\sqrt{U^2 + 16J^2}, \tag{E.7}$$

with corresponding eigenvectors

$$|s'\rangle = \cos\left(\frac{\theta}{2}\right)|s\rangle + \sin\left(\frac{\theta}{2}\right)|I_+\rangle, \tag{E.8}$$

$$|I'_+\rangle = -\sin\left(\frac{\theta}{2}\right)|s\rangle + \cos\left(\frac{\theta}{2}\right)|I_+\rangle, \tag{E.9}$$

with $\cos(\theta) = U/\sqrt{U^2 + 16J^2}$, and $\cos\left(\frac{\theta}{2}\right) = \sqrt{\frac{1+\cos(\theta)}{2}}$, $\sin\left(\frac{\theta}{2}\right) = \sqrt{\frac{1-\cos(\theta)}{2}}$.

[1] Remember that the order in which occupation numbers matter for fermions, so that $|L\uparrow, R\downarrow\rangle = -|R\downarrow, L\uparrow\rangle$.

F. The method of the effective Hamiltonian

In this Appendix, we discuss in more details the derivation of the superexchange Hamiltonian. We consider a quantum system with Hamiltonian

$$\hat{H} = \hat{H}_0 + \hat{H}_1. \tag{F.1}$$

The eigenvalues of $\hat{H}_0$ are organized into well-separated manifolds $\{\mathcal{E}_\nu\}_{\nu=0,\dots}$ containing several levels indexed $|i\nu\rangle$, as sketched in Figure F.1. We note $E_{i\nu}$ the energy of an individual level. The effective Hamiltonian method allows one to compute the effect of $\hat{H}_1$, treated as a weak perturbation, on a given manifold $\mathcal{E}_\alpha$, usually the lowest one. This method will be valid as long as all matrix elements of $\hat{H}_1$ are small compared to the energy separation between two of the $\mathcal{E}_\alpha$ subspaces.

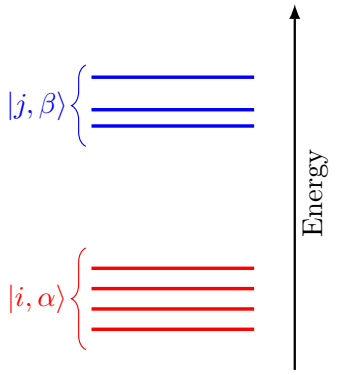

Figure F.1.: Energy diagrams of $\hat{H}_0$.

The method revolves around a unitary transformation $e^{i\hat{S}}$ generated by a Hermitian operator $\hat{S}$ of the same order as $\hat{H}_1$. We define $\hat{S}$ by imposing that the transformed Hamiltonian $\hat{H}' = e^{i\hat{S}}\hat{H}e^{-i\hat{S}}$ has the same eigenvalues as the restriction $\hat{P}_\alpha\hat{H}\hat{P}_\alpha$ of the Hamiltonian on the subspace $\mathcal{E}_\alpha$,with $\hat{P}_\alpha = \sum_i |i\alpha\rangle\langle i\alpha|$ the projector on $\mathcal{E}_\alpha$. This is equivalent to saying that $\hat{H}'$ is diagonal by blocks, *i.e.* the matrix elements between two different multiplicities $\mathcal{E}_\alpha$ and $\mathcal{E}_\beta$ ($\alpha \neq \beta$) vanish. There remains an ambiguity, in the sense that for any operator $\hat{T}$ that acts as the identity in $\mathcal{E}_\alpha$, $e^{i(\hat{S}+\hat{T})}$ is a unitary transformation satisfying our definition. We remove the ambiguity by imposing that $\hat{S}$ is purely non-diagonal, implying in particular

$$\langle i\alpha|\hat{S}|j\alpha\rangle = 0. \tag{F.2}$$

This allows one to perform a perturbative expansion of the transformed Hamiltonian,

$$\hat{H}' = e^{i\hat{S}}\hat{H}e^{-i\hat{S}} = \hat{H}_0 + \hat{H}_1 + i[\hat{S}_1,\hat{H}_0] + i[\hat{S}_2,\hat{H}_0] + i[\hat{S}_1,\hat{H}_1] + \hat{S}_1\hat{H}_0\hat{S}_1 - \frac{1}{2}\left(\hat{S}_1^2\hat{H}_0 + \hat{H}_0\hat{S}_1^2\right) + \cdots \tag{F.3}$$

The zeroth other and first order terms in the expansion are simply $\hat{H}_0$ and $\hat{H}_1$, due to the condition (F.2).
At first order, we define $\hat{S}_1$ by the vanishing of off-diagonal matrix elements of $\hat{H}'$ between different multiplicities,

$$\langle i\alpha|\hat{S}_1|j\beta\rangle = -i\frac{\langle i\alpha|\hat{H}_1|j\beta\rangle}{E_{i\alpha} - E_{j\beta}}, \qquad \alpha \neq \beta. \tag{F.4}$$

We then treat the second order terms. The term involving $\hat{S}_2$ vanishes due to (F.2), and the remaining terms can be evaluated to give the matrix elements (within $\mathcal{E}_\alpha$),

$$\langle i\alpha|\hat{P}_\alpha\hat{H}^{(\alpha)}_{\text{eff}}\hat{P}_\alpha|j\alpha\rangle = \langle i\alpha|\hat{H}|j\alpha\rangle + \frac{1}{2}\sum_{k,\beta\neq\alpha}\left(\frac{1}{E_{j\alpha} - E_{k\beta}} + \frac{1}{E_{i\alpha} - E_{k\beta}}\right) \times \langle i\alpha|\hat{H}_1|k\beta\rangle\langle k\beta|\hat{H}_1|j\alpha\rangle. \tag{F.5}$$

For $i = j$, we recover the result from ordinary second-order perturbation theory. We also obtain off-diagonal elements of the effective hamiltonian $\hat{H}^{(\alpha)}_{\text{eff}}$ acting within the subspace $\mathcal{E}_\alpha$ of interest.

Special case where all states in the subspace $\mathcal{E}_\alpha$ are degenerate with energy E_α:

$$\hat{P}_\alpha \hat{H}_{\text{eff}}^{(\alpha)} \hat{P}_\alpha = \hat{P}_\alpha \hat{H} \hat{P}_\alpha + \hat{P}_\alpha \hat{H}_1 \hat{Q}_\alpha \left(\frac{1}{E_\alpha - \hat{H}_0} \right) \hat{Q}_\alpha \hat{H}_1 \hat{P}_\alpha; \tag{F.6}$$

with $\hat{Q}_\alpha = 1 - \hat{P}_\alpha$, the projector complementary to $\hat{P}_\alpha$.

Bibliography

[1] G. Grynberg and C. Robilliard. Cold atoms in dissipative optical lattices. *Physics Reports*, 355(5–6):335–451, 12 2001.

[2] A. J. Leggett. Bose-einstein condensation in atomic gases: some fundamental concepts. *Rev. Mod. Phys.*, 73:307, 2001.

[3] P. O. Fedichev, M. W. Reynolds, and G. V. Shlyapnikov. Three-body recombination of ultracold atoms to a weakly bound s level. *Physical Review Letters*, 77(14):2921–2924, 09 1996.

[4] B. S. Rem, A. T. Grier, I. Ferrier-Barbut, U. Eismann, T. Langen, N. Navon, L. Khaykovich, F. Werner, D. S. Petrov, F. Chevy, and C. Salomon. Lifetime of the Bose gas with resonant interactions. *Physical Review Letters*, 110(16):163202–, 04 2013.

[5] Richard J. Fletcher, Alexander L. Gaunt, Nir Navon, Robert P. Smith, and Zoran Hadzibabic. Stability of a unitary Bose gas. *Physical Review Letters*, 111(12):125303–, 09 2013.

[6] D. S. Petrov, C. Salomon, and G. V. Shlyapnikov. Weakly bound dimers of fermionic atoms. *Phys. Rev. Lett.*, 93:090404, Aug 2004.

[7] J. D. Jackson. *Classical electrynamics, 3rd edition*. John Wiley & Sons, Inc., 1999.

[8] C. Cohen-Tannoudji, J. Dupont-Roc, and G. Grynberg. *Atom-photons interactions*. Wiley VCH, New York, 1997.

[9] C Becker, P Soltan-Panahi, J Kronjäger, S Dörscher, K Bongs, and K Sengstock. Ultracold quantum gases in triangular optical lattices. *New Journal of Physics*, 12(6):065025, 2010.

[10] Leticia Tarruell, Daniel Greif, Thomas Uehlinger, Gregor Jotzu, and Tilman Esslinger. Creating, moving and merging Dirac points with a Fermi gas in a tunable honeycomb lattice. *Nature*, 483(7389):302–305, 03 2012.

[11] A. Hemmerich and T. W. Hänsch. Two-dimensional atomic crystal bound by light. *Physical Review Letters*, 70(4):410–413, 01 1993.

[12] Gyu-Boong Jo, Jennie Guzman, Claire K. Thomas, Pavan Hosur, Ashvin Vishwanath, and Dan M. Stamper-Kurn. Ultracold atoms in a tunable optical Kagome lattice. *Phys. Rev. Lett.*, 108:045305, Jan 2012.

[13] Neil Ashcroft and David Mermin. *Solid State Physics*. Brooks/Cole, 1976.

[14] Jean Dalibard. Des cages de lumière pour les atomes : la physique des pièges et des réseaux optiques. available at http://www.phys.ens.fr/∼dalibard/, 2013.

[15] W. Kohn. Analytic properties of Bloch waves and Wannier functions. *Physical Review*, 115(4):809–821, 08 1959.

[16] Nicola Marzari and David Vanderbilt. Maximally localized generalized Wannier functions for composite energy bands. *Phys. Rev. B*, 56:12847–12865, Nov 1997.

[17] Immanuel Bloch, Jean Dalibard, and Wilhelm Zwerger. Many-body physics with ultracold gases. *Reviews of Modern Physics*, 80(3):885–964, 07 2008.

[18] M. Greiner, O. Mandel, T. Esslinger, T. W. Hänsch, and I. Bloch. Quantum phase transition from a superfluid to a Mott insulator in a gas of ultracold atoms. *Nature*, 415:39, 2002.

[19] Franco Dalfovo, Stefano Giorgini, Lev P. Pitaevskii, and Sandro Stringari. Theory of Bose-Einstein condensation in trapped gases. *Rev. Mod. Phys.*, 71:463, 1999.

[20] Albert Messiah. *Mécanique quantique*, volume 2. Dunod, 2000.

[21] P B Blakie and J. V. Porto. Adiabatic loading of bosons into optical lattices. *Phys. Rev. A*, 69:13603, 2004.

[22] D McKay and B DeMarco. Thermometry with spin-dependent lattices. *New Journal of Physics*, 12(5):055013, 2010.

[23] Markus Greiner, Immanuel Bloch, Olaf Mandel, Theodor W. Hänsch, and Tilman Esslinger. Exploring phase coherence in a 2D lattice of Bose-Einstein condensates. *Physical Review Letters*, 87(16):160405–, 10 2001.

[24] Stefan S. Natu, David C. McKay, Brian DeMarco, and Erich J. Mueller. Evolution of condensate fraction during rapid lattice ramps. *Phys. Rev. A*, 85:061601, Jun 2012.

[25] Michael Köhl, Henning Moritz, Thilo Stöferle, Kenneth Günter, and Tilman Esslinger. Fermionic atoms in a three dimensional optical lattice: Observing Fermi surfaces, dynamics, and interactions. *Physical Review Letters*, 94(8):080403–, 03 2005.

[26] M. P. A. Fisher, P. B. Weichman, G. Grinstein, and D. S. Fisher. Boson localization and the superfluid-insulator transition. *Phys. Rev. B*, 40:546, 1989.

[27] D. Jaksch, C. Bruder, J.Ĩ. Cirac, C.W̃. Gardiner, and P. Zoller. Cold bosonic atoms in optical lattice. *Phys. Rev. Lett.*, 81:3108, 1998.

[28] W. Zwerger. Mott-Hubbard transition of cold atoms in an optical lattice. *J. Opt. B: Quantum Semiclass. Opt.*, 5:S9–S16, 2003.

[29] K. Huang. *Statistical mechanics*. Wiley, New York, 1990.

[30] D. F. Walls and G. J. Milburn. *Quantum optics*. Springer-Verlag, Berlin, 1988.

[31] Roy J. Glauber. The quantum theory of optical coherence. *Phys. Rev.*, 131(6):2529, June 1963.

[32] L. Mandel and E. Wolf. *Optical coherence and quantum optics*. Cambridge University Press, Cambridge, MA, 1990.

[33] Oliver Penrose and Lars Onsager. Bose-einstein condensation and liquid helium. *Phys. Rev.*, 104(3):576, November 1956.

[34] J. Javanainen and S. M. Yoo. Relative phase of two Bose-Einstein condensates. *Phys. Rev. Lett.*, 76:161, 1996.

[35] Y. Castin and J. Dalibard. Relative phase of two Bose-einstein condensates. *Phys. Rev. A*, 55:4330, 1997.

[36] Lode Pollet. Recent developments in quantum Monte Carlo simulations with applications for cold gases. *Reports on Progress in Physics*, 75(9):094501, 2012.

[37] Daniel S. Rokhsar and B. G. Kotliar. Gutzwiller projection for bosons. *Physical Review B*, 44(18):10328–10332, 11 1991.

[38] Werner Krauth, Michel Caffarel, and Jean-Philippe Bouchaud. Gutzwiller wave function for a model of strongly interacting bosons. *Physical Review B*, 45(6):3137–3140, 02 1992.

[39] K. Sheshadri, H. R. Krishnamurthy, R. Pandit, and T. V. Ramakrishnan. Superfluid and insulating phases in an interacting boson model : mean-field theory and the RPA. *Euro. Phys. Lett.*, 22:257, 1993.

[40] L. Pitaevskii and S. Stringari. *Bose-Einstein condensation*. Oxford University Press, Oxford, 2003.

[41] R. Roth and K. Burnett. Superfluidity and interference pattern of ultracold bosons in an optical lattice. *Phys. Rev. A*, 67:031602 (R), 2003.

[42] D. van Oosten, Peter van der Straten, and H. T. C. Stoof. Quantum phases in an optical lattice. *Phys. Rev. A*, 63:053601, 2001.

[43] P. Nozières. Is the roton in superfluid ^{4}He the ghost of a Bragg spot? *Journal of Low Temperature Physics*, 137(1-2):45–67, 2004.

[44] Ehud Altman and Assa Auerbach. Oscillating superfluidity of bosons in optical lattices. *Phys. Rev. Lett.*, 89:250404, 2001.

[45] J. K. Freericks and H. Monien. Phase diagram of the Bose-Hubbard model. *EPL (Europhysics Letters)*, 26(7):545, 1994.

[46] F. Gerbier, S. Trotzky, S. Folling, U. Schnorrberger, J. D. Thompson, A. Widera, I. Bloch, L. Pollet, M. Troyer, B. Capogrosso-Sansone, N. V. Prokof'ev, and B. V. Svistunov. Expansion of a quantum gas released from an optical lattice. *Physical Review Letters*, 101(15):155303, 2008.

[47] Markus Greiner. *Ultracold quantum gases in three-dimensional optical lattice potentials*. LMU Munich, 2003.

[48] E. Altman, E. Demler, and M. D. Lukin. Probing many-body states of ultracold atoms via noise correlations. *Phys. Rev. A*, 70:013603, 2004.

[49] S. Fölling, F. Gerbier, A. Widera, O. Mandel, T. Gericke, and I. Bloch. Spatial quantum noise correlations of ultracold atoms released from an optical lattice. *Nature*, 434:481, 2005.

[50] R. Hanbury Brown and R. Q. Twiss. A test of a new type of stellar interferometer on Sirius. *Nature*, 178(4541):1046–1048, 11 1956.

[51] E. M. Purcell. The question of correlation between photons in coherent light rays. *Nature*, 178(4548):1449–1450, 12 1956.

[52] U. Fano. Quantum theory of interference effects in the mixing of light from phase-independent sources. *American Journal of Physics*, 29(8):539–545, 1961.

[53] M. Schellekens, R. Hoppeler, A. Perrin, J. Viana Gomes, D. Boiron, A. Aspect, and C. I. Westbrook. Hanbury Brown Twiss effect for ultracold quantum gases. *Science*, 310(5748):648–651, 10 2005.

[54] T. Rom, Th. Best, D. van Oosten, U. Schneider, S. Folling, B. Paredes, and I. Bloch. Free fermion antibunching in a degenerate atomic Fermi gas released from an optical lattice. *Nature*, 444(7120):733–736, 12 2006.

[55] F. Gerbier, A. Widera, S. Fölling, O. Mandel, T. Gericke, and I. Bloch. Phase coherence of an atomic Mott insulator. *Phys. Rev. Lett.*, 95:050404, 2005.

[56] C. Kollath, A. Iucci, T. Giamarchi, W. Hofstetter, and U. Schollwöck. Spectroscopy of ultracold atoms by periodic lattice modulations. *Phys. Rev. Lett.*, 97:050402, Jul 2006.

[57] Christian Schori, Thilo Stöferle, Henning Moritz, Michael Köhl, and Tilman Esslinger. Excitations of a superfluid in a three-dimensional optical lattice. *Phys. Rev. Lett.*, 93:240402, Dec 2004.

[58] Jongchul Mun, Patrick Medley, Gretchen K. Campbell, Luis G. Marcassa, David E. Pritchard, and Wolfgang Ketterle. Phase diagram for a Bose-Einstein condensate moving in an optical lattice. *Phys. Rev. Lett.*, 99:150604, Oct 2007.

[59] Oliver Morsch and Markus Oberthaler. Dynamics of Bose-Einstein condensates in optical lattices. *Rev. Mod. Phys.*, 78:179–215, Feb 2006.

[60] E. Altman, A. Polkovnikov, E. Demler, B. I. Halperin, and M. D. Lukin. Superfluid-insulator transition in a moving system of interacting bosons. *Phys. Rev. Lett.*, 95:020402, Jul 2005.

[61] A. Polkovnikov, E. Altman, E. Demler, B. Halperin, and M. D. Lukin. Decay of superfluid currents in a moving system of strongly interacting bosons. *Phys. Rev. A*, 71:063613, Jun 2005.

[62] G. G. Batrouni, V. Rousseau, R. T. Scalettar, M. Rigol, A. Muramatsu, P. J. H. Denteneer, and M. Troyer. Mott domains of bosons confined on optical lattices. *Physical Review Letters*, 89(11):117203, 08 2002.

[63] Jacob F. Sherson, Christof Weitenberg, Manuel Endres, Marc Cheneau, Immanuel Bloch, and Stefan Kuhr. Single-atom-resolved fluorescence imaging of an atomic Mott insulator. *Nature*, 467(7311):68–72, 09 2010.

[64] W. S. Bakr, A. Peng, M. E. Tai, R. Ma, J. Simon, J. I. Gillen, S. Fölling, L. Pollet, and M. Greiner. Probing the superfluid–to–Mott insulator transition at the single-atom level. *Science*, 329(5991):547–550, 07 2010.

[65] Simon Fölling, Artur Widera, Torben Müller, Fabrice Gerbier, and Immanuel Bloch. Formation of spatial shell structures in the superfluid to Mott insulator transition. *Phys. Rev. Lett.*, 97:060403, 2006.

[66] Nathan Gemelke, Xibo Zhang, Chen-Lung Hung, and Cheng Chin. In situ observation of incompressible Mott-insulating domains in ultracold atomic gases. *Nature*, 460(7258):995–998, 08 2009.

[67] Fabrice Gerbier. Boson Mott insulators at finite temperatures. *Phys. Rev. Lett.*, 99:120405, Sep 2007.

[68] S. Trotzky, L. Pollet, F. Gerbier, U. Schnorrberger, I. Bloch, N. V. Prokof/'ev, B. Svistunov, and M. Troyer. Suppression of the critical temperature for superfluidity near the Mott transition. *Nat Phys*, 6(12):998–1004, December 2010.

[69] Antoine Georges. Condensed matter physics with light and atoms: Strongly correlated cold fermions in optical lattices. In M. Inguscio, W. Ketterle, and C. Salomon, editors, *Ultracold Fermi Gases*, Lectures given at the Enrico Fermi Summer School, 2007. arXiv:cond-mat/0702122.

[70] Antoine Georges and Thierry Giamarchi. Strongly correlated bosons and fermions in optical lattices. In C. Salomon, G. Shlyapnikov, and L. Cugliandolo, editors, *Many-Body Physics with Ultracold Gases*, volume 94 of *Lecture Notes of the Les Houches Summer School*. Oxford University Press, 2012. arXiv:1308.2684.

[71] F. Werner, O. Parcollet, A. Georges, and S. R. Hassan. Interaction-induced adiabatic cooling and antiferromagnetism of cold fermions in optical lattices. *Phys. Rev. Lett.*, 95:056401, Jul 2005.

[72] Robert Jordens, Niels Strohmaier, Kenneth Gunter, Henning Moritz, and Tilman Esslinger. A Mott insulator of fermionic atoms in an optical lattice. *Nature*, 455(7210):204–207, 09 2008.

[73] U. Schneider, L. Hackermuller, S. Will, Th. Best, I. Bloch, T. A. Costi, R. W. Helmes, D. Rasch, and A. Rosch. Metallic and insulating phases of repulsively interacting fermions in a 3D optical lattice. *Science*, 322(5907):1520–1525, 2008.

[74] Maxwell F. Parsons, Florian Huber, Anton Mazurenko, Christie S. Chiu, Widagdo Setiawan, Katherine Wooley-Brown, Sebastian Blatt, and Markus Greiner. Site-resolved imaging of fermionic ^{6}Li in an optical lattice. *Phys. Rev. Lett.*, 114:213002, May 2015.

[75] Elmar Haller, James Hudson, Andrew Kelly, Dylan A. Cotta, Bruno Peaudecerf, Graham D. Bruce, and Stefan Kuhr. Single-atom imaging of fermions in a quantum-gas microscope. *Nat Phys*, 11(9):738–742, September 2015.

[76] G. J. A. Edge, R. Anderson, D. Jervis, D. C. McKay, R. Day, S. Trotzky, and J. H. Thywissen. Imaging and addressing of individual fermionic atoms in an optical lattice. *Phys. Rev. A*, 92:063406, Dec 2015.

[77] Ahmed Omran, Martin Boll, Timon A. Hilker, Katharina Kleinlein, Guillaume Salomon, Immanuel Bloch, and Christian Gross. Microscopic observation of Pauli blocking in degenerate fermionic lattice gases. *Phys. Rev. Lett.*, 115:263001, Dec 2015.

[78] Lawrence W. Cheuk, Matthew A. Nichols, Melih Okan, Thomas Gersdorf, Vinay V. Ramasesh, Waseem S. Bakr, Thomas Lompe, and Martin W. Zwierlein. Quantum-gas microscope for fermionic atoms. *Phys. Rev. Lett.*, 114:193001, May 2015.

[79] Daniel Greif, Maxwell F. Parsons, Anton Mazurenko, Christie S. Chiu, Sebastian Blatt, Florian Huber, Geoffrey Ji, and Markus Greiner. Site-resolved imaging of a fermionic Mott insulator. *Science*, 351(6276):953–957, 2016.

[80] Laurent-Patrick Levy. *Magnétisme et supraconductivité*. CNRS Editions, Paris, 1998.

[81] Anton Mazurenko, Christie S. Chiu, Geoffrey Ji, Maxwell F. Parsons, Màrton Kanàsz-Nagy, Richard Schmidt, Fabian Grusdt, Eugene Demler, Daniel Greifan, and Markus Greiner. Experimental realization of a long-range antiferromagnet in the Hubbard model with ultracold atoms. cond-mat:1612.08436, 2016.

[82] Daniel Greif, Thomas Uehlinger, Gregor Jotzu, Leticia Tarruell, and Tilman Esslinger. Short-range quantum magnetism of ultracold fermions in an optical lattice. *Science*, 340(6138):1307–1310, 06 2013.

[83] Daniel Greif, Gregor Jotzu, Michael Messer, Rémi Desbuquois, and Tilman Esslinger. Formation and dynamics of antiferromagnetic correlations in tunable optical lattices. *Phys. Rev. Lett.*, 115:260401, Dec 2015.

[84] Maxwell F. Parsons, Anton Mazurenko, Christie S. Chiu, Geoffrey Ji, Daniel Greif, and Markus Greiner. Site-resolved measurement of the spin-correlation function in the Fermi-Hubbard model. *Science*, 353(6305):1253–1256, 2016.

[85] Martin Boll, Timon A. Hilker, Guillaume Salomon, Ahmed Omran, Jacopo Nespolo, Lode Pollet, Immanuel Bloch, and Christian Gross. Spin- and density-resolved microscopy of antiferromagnetic correlations in Fermi-Hubbard chains. *Science*, 353(6305):1257–1260, 2016.

[86] Lawrence W. Cheuk, Matthew A. Nichols, Katherine R. Lawrence, Melih Okan, Hao Zhang, Ehsan Khatami, Nandini Trivedi, Thereza Paiva, Marcos Rigol, and Martin W. Zwierlein. Observation of spatial charge and spin correlations in the 2D Fermi-Hubbard model. *Science*, 353(6305):1260–1264, 2016.

[87] Peter T. Brown, Debayan Mitra, Elmer Guardado-Sanchez, Peter Schauss, Stanimir S. Kondov, Ehsan Khatami, Thereza Paiva, Nandini Trivedi, David A. Huse, and Waseem S. Bakr. Observation of canted antiferromagnetism with ultracold fermions in an optical lattice. eprint cond-mat:1612.07746, 2016.